Durham University

Durham E-Theses

Manifestation of quantum resonant effects in the atom-optical delta-kicked accelerator

Saunders, Mark

How to cite:

Saunders, Mark (2009) *Manifestation of quantum resonant effects in the atom-optical delta-kicked accelerator*, Durham theses, Durham University. Available at Durham E-Theses Online: http://etheses.dur.ac.uk/2087/

Use policy

The full-text may be used and/or reproduced, and given to third parties in any format or medium, without prior permission or charge, for personal research or study, educational, or not-for-profit purposes provided that:

- a full bibliographic reference is made to the original source
- a link is made to the metadata record in Durham E-Theses
- the full-text is not changed in any way

The full-text must not be sold in any format or medium without the formal permission of the copyright holders.

Please consult the full Durham E-Theses policy for further details.

Academic Support Office, The Palatine Centre, Durham University, Stockton Road, Durham, DH1 3LE
e-mail: e-theses.admin@durham.ac.uk Tel: +44 0191 334 6107
http://etheses.dur.ac.uk

The copyright of this thesis rests with the author or the university to which it was submitted. No quotation from it, or information derived from it may be published without the prior written consent of the author or university, and any information derived from it should be acknowledged.

Manifestation of quantum resonant effects in the atom-optical delta-kicked accelerator

by

Mark Saunders

Submitted in conformity with the requirements
for the degree of Doctor of Philosophy.

Atomic and Molecular Physics
Physics Department
Durham University

© 2009 Mark Saunders

1 2 AUG 2009

Abstract

In this thesis we investigate quantum resonant effects in the atom-optical δ-kicked accelerator.

Using Floquet analysis, we theoretically study the time evolution of quantum systems which have a classical counterpart that exhibits chaotic dynamics. We introduce quantum resonance and quantum antiresonance features of the quantum δ-kicked rotor by setting the pulse period to an integer multiple of the half-Talbot time. The model is generalised to the atom-optical δ-kicked accelerator by considering thermal alkali atoms subject to a periodically pulsed standing wave potential formed from counter-propagating laser beams.

The dynamics of the momentum distribution is analysed by evaluating the momentum moments and momentum cumulants. We derive analytic solutions for these observables for the ultracold and thermal limiting cases, and observe fractional quantum resonant phenomena. Simulations have been developed to examine the time evolution for individual momentum eigenstates, which we use to construct a non-interacting finite temperature gas, based upon a Monte Carlo method. We investigate the temperature dependence of the δ-kicked rotor, neglecting gravitational effects, and show that the atomic dynamics is highly sensitive to the initial momentum width of the gas. A generalisation of the model to quantify the transition between the ultracold and thermal temperature regimes of the atom-optical δ-kicked accelerator is examined using linear regression analysis. High order quantum resonance features are found to be sensitive to the relative acceleration between the atomic gas and the pulsed optical standing wave.

We assess the dependence of the δ-kicked accelerator upon gravitational acceleration, quantifying the width of the high order quantum resonance features, which we use to assess the prospect for precision measurement using a finite temperature gas.

Contents

Acknowledgements

Simon Gardiner has been a fantastic supervisor, and I certainly appreciate him teaching me the skills required to be a theoretical physicist. I have enjoyed collaborating on this project with Katherine Challis and Paul Halkyard. We acknowledge everyone who contributed to the project: *Sensitivity to Gravity of Driven Cold-Atom Dynamics.* Funding was provided by Durham University and the UK Engineering and Physical Sciences Research Council (EPSRC) with grant numbers: EP/D032970/1 and EP/D037174/1.

I am grateful for advice at group meetings from members of the Durham University Atomic and Molecular Physics group, in particular Charles Adams, Simon Cornish, Ifan Hughes, and Matt Jones. Hosting the Young Atom Opticians conference helped me to gain experience in project planning, so thank you to everyone who participated. I had inspiring discussions on this project with Mark Fromhold, David Hallwood, Tania Monteiro, and Alexey Tonyushkin. For reviewing the transcript, I would like to thank Andrew Martin, Robert Potvliege, Ian Saunders, and Denise Spangler. Thank you to Chris Done and John Saunders for advising me on writing my thesis. Thank you to Pauline Walker and Jeff Walker for helping me to prepare for my viva exam.

I would also like to acknowledge my family for supporting me throughout my life. I have also learned a great deal from my students at Durham University taekwondo society. I look forward to travelling to South Korea to begin my career as a physicist at Seoul National University.

Finally I would like to say thank you to Denise Spangler, who has been there for me throughout my Ph. D. I can't wait to marry you and continue our special adventure for many years to come.

Dedication

This thesis is dedicated to my parents

Pauline Walker

and

John Saunders.

List of Publications

[1] Mark Saunders, Paul L. Halkyard, Katharine J. Challis, and Simon A. Gardiner.
Physical Review A 76, 043415 (October 2007)
Manifestation of quantum resonances and antiresonances in a finite-temperature dilute atomic gas

[2] Paul L. Halkyard, Mark Saunders, Simon A. Gardiner, and Katharine J. Challis.
Physical Review A 78, 063401 (November 2008)
Power-law behavior in the quantum-resonant evolution of the δ-kicked accelerator

[3] Mark Saunders, Paul L. Halkyard, Simon A. Gardiner, and Katharine J. Challis.
Physical Review A 79, 023423 (February 2009)
Fractional resonances in the atom-optical δ-kicked accelerator

List of Figures

List of Tables

List of Symbols

a	Linear acceleration $a = g - a_\phi$.
a_ϕ	Linear acceleration due to the phase shifted laser beam.
$\hat{A}$	Arbitrary operator.
b	Summation index.
b	Gradient from linear regression analysis with Eq. (11.3).
b_{opt}	Optimal gradient: standard error minimised in Section 11.3.3.
b_{th}	Gradient saturation value in the thermal limit.
B	Number of bins over the quasimomentum range.
$\hat{B}$	Arbitrary operator.
$c_{kj}(\beta, nT)$	Probability amplitudes.
c	Constant from linear regression analysis with Eq. (11.3).
c	Arbitrary constant.
$D_j(\beta, t = nT)$	Individual eigenstate momentum evolution, given by Eq. (4.20).
$D(p)$	Momentum distribution function.
$\|e\rangle$	Excited state of two level atom, eliminated in Section B.5.
$\hat{E}_T$	Free evolution operator.
$E_q(\langle\langle \hat{p}^q \rangle\rangle_n^{1/q})$	Error in the qth momentum cumulant, from Section 6.4
f	Kick strength factor in Eq. (2.3), with units of momentum.
$f(\hat{B})$	Arbitrary function in Section A.2, which may be Taylor expanded.
$\vec{F}$	Periodic force applied to the classical δ-kicked rotor.
$F(t)$	Time dependent force, defined by Eq. (2.3).
$\hat{F}$	Floquet operator.
$\hat{F}_{\delta\text{kr}}$	Floquet operator of the quantum δ-kicked rotor.
$\hat{F}_{\delta\text{ka}}$	Time evolution operator of the atom-optical δ-kicked accelerator.
$\tilde{F}_n(\beta)$	Transformed time evolution operator, given by Eq. (4.12).
$\tilde{\mathcal{F}}_n(\beta)$	Time-ordering of $\tilde{F}_n(\beta)$, defined by Eq. (4.16).

$\|g\rangle$	Ground state of a two level atom.
g	Local gravitational acceleration.
δg	Width in the gravitational sensitivity.
$\hbar$	Planck's constant $\hbar = h/2\pi = 1.055 \times 10^{-34}$ Js.
$\hbar K$	Momentum unit: Two photon recoils.
$\hbar\omega_L$	Energy difference between the internal atomic energy levels.
H_{rotor}	Classical rotor Hamiltonian, given by Eq. (2.1).
H_{pendulum}	Classical forced rotor Hamiltonian, given by Eq. (2.2).
$H_{\delta\text{kr}}$	Classical δ-kicked rotor Hamiltonian, given by Eq. (2.4).
$\hat{H}_{\delta\text{kr}}$	Quantum δ-kicked rotor Hamiltonian, given by Eq. (3.1)
$\hat{H}_{\delta\text{ka}}$	Atom-optical δ-kicked accelerator Hamiltonian, defined by Eq. (4.3).
$\tilde{H}_{\delta\text{ka}}$	Transformed Hamiltonian, in reference frame of the falling atoms.
$\hat{H}_{2\text{level}}$	Two-level atom Hamiltonian, defined by Eq. (4.2).
$\hat{H}_{1\text{level}}$	Excited state suppressed in Hamiltonian (B.18)
$\hat{H}_{\delta}$	Periodically pulsed Hamiltonian (B.19).
H.c.	Hermitian conjugate, defined by $\hat{U}^{\dagger} = (\hat{U}^{*})^{T}$.
i	Imaginary number.
I	Moment of inertia of the classical δ-kicked rotor.
$\|j\rangle$	Discrete eigenstate spectrum of $\hat{J}$.
j	Eigenvalues of $\|j\rangle$, restricted to be an integer.
j, k	Counting index used to label the momentum eigenstates.
J	Angular momentum $J = \|\vec{J}\| = \|\vec{R} \times \vec{p}\|$.
$\hat{J}$	Angular momentum operator.
$\hat{J}'$	Transformed angular momentum operator, defined by Eq. (3.3).
k	Rescaled Planck's constant, defined by Eq. (3.4).
k_L	Magnitude of wave-vector corresponding to laser frequency ω_L.
$\hat{k}$	Discrete momentum operator, defined by Eq. (4.7).
k	Discrete momentum eigenvalues.
k_{limit}	Extent of the discrete momentum basis.
$\hat{K}_{\delta}$	Evolution due to one kick.
K	Wavenumber of the standing-wave pulses.
ℓ	Restriction of the rescaled Planck's constant, imposed by Eq. (3.4).
ℓ	Integer multiple of half-Talbot times, defined by Eq. (3.33).
ℓ'	Effective kick period $T = \ell' T_T/2$, defined as integer $\ell' = \ell + \Omega$.

m	Integer defining $\Upsilon = m\pi$.
m	Counting index in Appendix E.
M	Mass of each individual atom.
n	Number of kicks.
nT^+	The time infinitesimally after the nth kick.
n_R	Quantum resonance transition kick number.
n_A	Quantum antiresonance transition kick number.
n_{FR}	Fractional quantum resonance transition kick number.
n'	In Section D.5, an even number of kicks is expressed by $n = 2n'$
$\mathcal{N}$	The sample size of momentum eigenstates.
N	Order of the quantum antiresonance.
$\hat{O}(\tau)$	Operator defined by Eq. (A.14), factorised in Section A.5.
$\vec{p}$	Classical linear momentum vector.
$\hat{p}$	Momentum operator.
p	Momentum values.
$\|p\rangle = \|k + \beta\rangle$	Momentum eigenstate.
$\langle \hat{p}^q \rangle_n$	Momentum moment of order q.
$\langle\langle \hat{p}^q \rangle\rangle_n$	Momentum cumulant of order q.
$\Delta\langle\langle \hat{p}^2 \rangle\rangle_n$	Change in second-order momentum cumulant, plotted in Fig. 11.2.
$\langle\langle \hat{p}^4 \rangle\rangle_n^{1/3}$	Cube root of fourth-order momentum cumulant, plotted in Fig. 11.3.
q	Counting index for the order of the moments and cumulants.
r_1	Denotes integer values of Ω, for which $s = 1$.
r_2	Denotes integer values of Ω, for which $s = 2$.
R	Radius of the classical δ-kicked rotor.
s	Order of fractional quantum resonance from setting $\Omega = 1/s$.
t	Time.
t_p	Laser pulse duration.
T	Pulse period, defined be Eqs. (3.33) and (4.10).
T_T	Talbot time, defined be Eqs. (3.32) and (4.11).
$\mathcal{T}_w$	Maxwell-Boltzmann temperature, given by Eq. (5.15).
U	Optical dipole potential, defined by Eq. (1.1).
U_0	Optical dipole potential depth.
$\hat{U}(t)$	Unitary operator defined by Eq. (4.5).
$\hat{U}_1$, $\hat{U}_2$	Unitary operators used in Section A.4 to derive basis transformations.

$\hat{U}_3$	Unitary operator defined by Eq. (B.3) to eliminate the $\|g\rangle\langle g\|$ term.
$\hat{U}_4$	Operator (B.9) transforms to accelerating frame.
$\hat{U}_5$	Unitary operator defined by Eq. (B.17).
w	Width of initial finite-temperature momentum distribution (5.14).
w_{th}	Thermalisation transition width of the atom cloud.
x	Generic variable used for expressing trigonometric formulae.
(x, y)	Restricted plane of the classical δ-kicked rotor.
z	The classical δ-kicked rotor processes about the z-axis.
$\hat{z}$	Position operator.
∞	Infinity.
α	Parameter used in identities (E.12) and (E.20).
$\hat{\beta}$	Quasimomentum operator, defined by Eq. (4.7).
β	Quasimomentum eigenvalue.
β_m^R	Resonant value of the quasimomentum.
β_m^A	Antiresonant value of the quasimomentum.
$\bar{\beta}^R$	Reconstruction loci from Eq. (9.12).
$\delta\beta_R$	Quantum resonance width from Eq. (9.13).
$\bar{\beta}^A$	Reconstruction loci from Eq. (9.14).
$\delta\beta_A$	Quantum antiresonance width from Eq. (9.15).
γ	Constant used in Section A.2 to define $\hat{B}$ to be linear in $\hat{z}$.
γ_n	Transformed Floquet operator parameter defined by Eq. (C.9).
$\delta(t - nT)$	Dirac δ-function describes a train of kicks with Eq. (2.3).
δ_{k0}	Kronecker δ-function.
Δ	Laser detuning, defined $\Delta \equiv \omega_0 - \omega_L$.
Δt	Time interval.
η	Gauss sum, defined by Eq. (D.7).
η	Bessel function argument used in Section 5.4 and Appendix E.
θ	Angle of the classical δ-kicked rotor.
$\hat{\theta}$	Angle operator.
κ	Stochasticity parameter.
κ_c	Critical value of the stochasticity parameter.
λ	Parameter used in identities (E.12) and (E.20).
μK	Temperature unit: microKelvin.
μ	Integer in Eq. (9.12).

μ'	Integer in Eq. (9.14).
$\nu_{n,\ell}(\Omega,\beta)$	Matrix element parameter defined by Eq. (D.6).
ξ, ξ_1, ξ_2	Parameter used to define the unitary operators in Section A.4.
π	Constant $\pi = 3.14159265\ldots$.
$\hat{\rho}(t=0)$	Initial density operator, defined by Eq. (5.1).
ρ_1, ρ_2, ρ_3	Constants defining defining $\hat{A}$ quadratic in $\hat{p}$, used Section A.5.
τ	Infinitesimal region integrated over in Eq. (3.11).
τ	Large time interval in Eq. (4.1) before time-of-flight measurement.
τ	Parameter in Eq. (A.1) from which we derive Eq. (A.3).
Υ	Matrix element parameter incorporating β, defined by Eq. (9.3).
ϕ_d	Kick strength defined by Eq. (3.26).
ϕ_1, ϕ_2	Laser phases from Eq. (4.2).
ϕ_r, ϕ_s	Phases defined to simplify the $\|e\rangle\langle g\|$ to Eq. (B.3).
$\|\phi\rangle$, $\|\psi\rangle$	State vectors used in Section A.4 to derive basis transformations.
$\|\Psi(t)\rangle$	Wave-vector, governed by the Schrödinger equation (3.7).
$\|\tilde{\Psi}(t)\rangle$	Unitary transformation of $\|\Psi(t)\rangle$, evaluated by Eq. (A.7).
χ	Phase parameter introduced in Eq. (D.5).
ω_L	Laser frequency, introduced in Eq. (4.2).
ω_0	Frequency to induce a transition from $\|g\rangle$ to $\|e\rangle$ in Eq. (4.2).
ω	Bessel function argument in Eq. (5.5).
Ω	Effective gravity parameter defined by Eq. (4.13).
$\Omega = r/s$	Rational values of Ω, by choosing integers r and s.
Ω_{R1}, Ω_{R2}	Rabi frequencies from Eq. (4.2).
Ω_R	Rabi frequencies set to be the same, to obtain Eq. (B.2).
Ω_m^{FR}	Value of Ω corresponding to a fractional quantum resonance.
$\bar{\Omega}_R$, $\bar{\Omega}'_R$	Asymptote in the vicinity of a fractional quantum resonance.
$\bar{\Omega}_A$, $\bar{\Omega}'_A$	Asymptote in the vicinity of a quantum antiresonance.
$\delta\Omega'$	Fractional quantum resonance width, given by Eq. (12.7).

Chapter 1

Introduction

1.1 Overview

We investigate a periodically driven system known as the quantum δ-kicked rotor, observing phenomena known as quantum resonance and quantum antiresonance. These effects have been studied in experiment by exposing laser cooled atoms to laser pulses. With the system oriented vertically, we analyse high-order quantum resonant effects by incorporating gravity. In this chapter, we describe and motivate the structure and content of the thesis [1–3].

1.2 Thesis outline

In this thesis, we theoretically analyse various arrangements of δ-kicked systems. In the context of atomic physics, we simulate a finite temperature distribution of alkali atoms subject to periodic laser beam pulses.

We describe the background information for this thesis over three chapters. In Chapter 2, we introduce the classical δ-kicked rotor. This is a simple mathematical model which we use to explain the transition from stable to chaotic dynamics. In Chapter 3, we discuss the quantum counterpart to the classically chaotic regime. We define the quantum resonance and quantum antiresonance features, highlighting their dependence upon the periodicity of the kicks by drawing an analogy to the Talbot effect from the field of optics. We generalise to the atom-optical δ-kicked accelerator in Chapter 4, by incorporating temperature and gravity into the quantum δ-kicked rotor model. In this thesis, we present results for the atom-optical arrangement for a variety of experimental configurations.

With the next four chapters, we outlined the analytic and numerical methods used to model the system, and demonstrated that both approaches are compatible. We define the observables used to quantify the dynamics in Chapter 5. Analytic solutions are summarised for the ultracold and thermal regimes, from which we infer that high-order quantum resonant effects contribute to the time evolution. The numerical simulation used to model the atom-optical δ-kicked accelerator is presented in Chapter 6. We assess the analytic predictions in Chapter 7 for the ultracold limit by determining the evolution of a zero momentum eigenstate, and in Chapter 8 by analysing the behaviour for the thermal limit, which is approximated by a broad initial distribution of momentum eigenstates.

We present original results in the next four chapters. We observe quantum resonant effects for a variety of experimental parameters, which have been shown in experiment to have applications to precision measurement of velocity, and both linear and angular acceleration. We examine the contribution from the individual momentum eigenstates in Chapter 9, from which a finite temperature gas is constructed. This allows us to study the temperature dependence of quantum resonances and quantum antiresonances in Chapter 10 by considering the special case of the atom-optical δ-kicked rotor, for which the gravitational acceleration is neglected. In Chapter 11, we study the generalised atom-optical δ-kicked accelerator by incorporating gravitational effects into the model. We investigate the dynamics for a finite-temperature gas cloud subject to particular values of a gravity parameter, and observe the high-order quantum resonant features. In Chapter 12, we examine the gravity dependence of the δ-kicked accelerator. We assess the time evolution for the ultracold limit, and then explore the limits for which a finite temperature gas exhibits the ultracold behaviour.

We summarise the thesis conclusions in Chapter 13, which is followed by five appendices that contain analytic derivations which we make use of in the main body of the text. The remit for this thesis is to explore the implementation of δ-kicked systems in the context of atomic physics.

1.3 Publications

In Publication [1], we investigated the quantum resonance and quantum antiresonance features of the atom-optical δ-kicked rotor. In Chapter 10 we present results for a finite temperature gas, which is constructed from momentum eigenstates analysed in Chapter 9.

Introducing gravity into the model, we present analytic results from Publication [2]. We evaluate observables in Chapter 5, which we summarise for the ultracold regime in Table 7.1, and for the thermal regime in Table 8.1.

In Publication [3], we explore the gravity dependence of the atom-optical δ-kicked accelerator. In Chapter 11, we compare specific values of the gravity parameter for a thermal gas. We present the gravity dependence in Chapter 12. Note that the gravitational senstitivity results for a finite temperature gas are preliminary in scope.

1.4 Research context

To develop our understanding of quantum phenomena, we are interested in the quantum mechanical counterpart to classical Hamiltonian systems [4–6]. The classical δ-kicked rotor has been extensively modelled, since despite being defined from a simple iterative map [7, 8], its dynamics undergo a transition from stablity to chaos as the driving force increases. In contrast to the classically chaotic regime, the quantum δ-kicked rotor displays signatures that highlight its quantum nature [9–12].

In this thesis, we study quantum δ-kicked systems, as studied by S. A. Gardiner, as published in Refs. [1–3, 13–22]. Quantum resonant features of periodically driven systems have received significant attention [23–34], with a variety of theoretical models investigated by the Monteiro group at UCL, studying aspects including spin chains [35, 36], Bogoliubov resonances [37], localization [38], double δ-kicked systems [39–41], chaotic quantum ratchets [42, 43], and observation of nonlinear resonances [44].

Quantum versions of classically chaotic systems have been studied for a variety of experimental configurations. In this thesis, we study quantum δ-kicked systems in the context of atomic-physics by considering a cloud of atoms subject to a periodically pulsed laser potential. The atom-optical δ-kicked rotor which was first studied experimentally by the Raizen group at Austin, Texas, analysing quantum resonance using sodium atoms [45–54]. Incorporating gravity, the δ-kicked accelerator was investigated by the Burnett group at Oxford, demonstrating the principle of gravity measurement using caesium atoms [16–18, 21, 55–62]. In the ultracold regime, experiments with Bose-Einstein condensates have made it possible to observe quantum antiresonances [63], and provide detailed information about the momentum distribution of a δ-kicked gas [64, 65], with the observation of high-order quantum resonances [66, 67].

1.5 Atom-light interactions

In this thesis, we consider two counter-propagating laser beams, with a wave-vector along the vertical z direction of magnitude k_L, which forms an optical dipole potential [68–70]

$$U = -U_0 \sin^2 k_L z, \tag{1.1}$$

where the potential depth $U_0 = \hbar\Omega_R^2/4|\Delta|$, where Ω_R is the Rabi frequency and Δ is the detuning. A well localised atom with a broad range of momentum, experiences a force given by

$$F = -\nabla U. \tag{1.2}$$

In Section 4.2.3, we present the system Hamiltonian, adopting the two-level atom approximation. The available atom-light interaction mechanisms are absorption, spontaneous emission and stimulated emission. For large values of Δ, spontaneous emission may be neglected by adiabatic elimination of the excited state. We find that the atoms experience a change in momentum in units of $\hbar K$, which corresponds to two photon recoils, as explained in Section 4.4.3.

A high temperature cloud of atoms corresponding to the classical limit is composed from a broad distribution of momentum states, and in position space is described by a localised wave packet.

To observe quantum resonant effects, we need to be in the low temperature limit where the momentum distribution is less that $\hbar K$, such that the atomic wavepacket is delocalised. In this case, the periodically pulsed standing wave imprints a phase upon each spatial part of the wavepacket, and the relative phase determines whether we see quantum resonance or quantum antiresonance effects. The results for the ultracold limit are presented in Chapter 7, with the transition of the dynamics to the ultracold regime analysed in Chapters 10 and 11.

Over the duration of the pulses, the atoms do not move a large distance, although their momentum is modified. Therefore, in Section 4.2.1 we explain how the momentum is measured using a time-of-flight method, from which observables are defined and analytically evaluated in Chapter 5.

1.6 Summary

In this thesis, we present a model to describe the quantum δ-kicked accelerator, which:

1. Can be experimentally realised using an atom-optical configuration.
2. Has potential applications to precision measurement of momentum, angular acceleration, and linear acceleration.
3. Exhibits quantum resonant effects which are intrinsic to quantum mechanics, thus enabling the quantum counterpart to a classically chaotic regime to be studied.

Chapter 2

The classical δ-kicked rotor

2.1 Overview

Classical systems which exhibit extreme sensitivity to changes in initial conditions are said to be chaotic, and have been studied extensively for a variety of simple systems [4, 6]. The δ-kicked rotor is an important model due to the complex dynamics exhibited by the system despite being described by a simple mathematical definition. In this chapter, we review the properties of the classical δ-kicked rotor, in preparation for our investigation into the quantum δ-kicked rotor.

2.2 Model Hamiltonian

The rotor is defined by a mass M with linear momentum $\vec{p}$, constrained to move on a circle of radius R. The energy of this system is represented by the Hamiltonian [71]

$$H_{\text{rotor}} = \frac{J^2}{2I}, \tag{2.1}$$

with the moment of inertia $I = MR^2$. It is convenient to select a coordinate system defined such that the mass is constrained to the (x, y)-plane, precessing about the z-axis with angular momentum $J = |\vec{J}| = |\vec{R} \times \vec{p}|$.

Adding a constant force $\vec{F}$ along the x-direction, we produce a pendulum, as sketched in Fig. 2.1. This is described by the Hamiltonian [71]

$$H_{\text{pendulum}} = \frac{J^2}{2I} - FR\cos\theta, \tag{2.2}$$

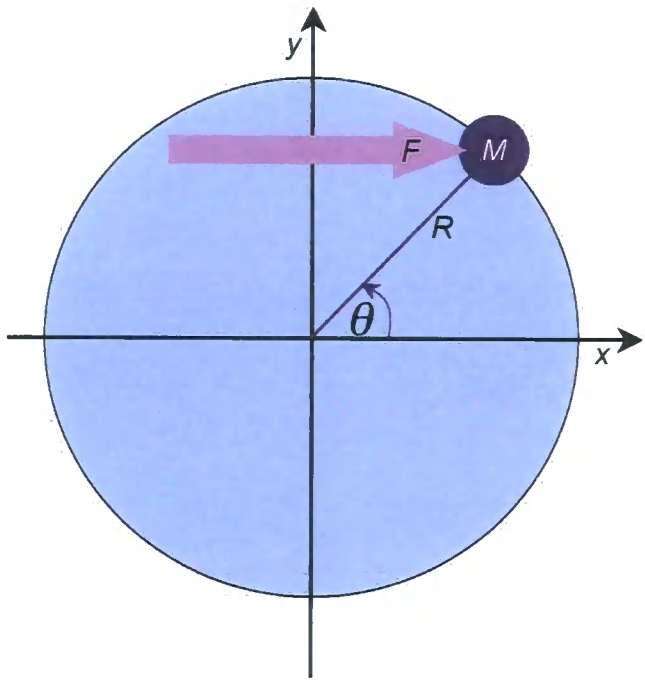

Figure 2.1: The δ-kicked rotor is modelled by a body of mass M constrained to move on circle of radius R, subject to periodic pulsing of force $\vec{F}$, as described by Eq. (2.4).

where θ is the angular position of the oscillator.

We now consider the force to be time dependent. In particular, we introduce into the model a periodic sequence of instantaneous δ-kicks, given by

$$F(t) = f \sum_{n=0}^{\infty} \delta(t - nT), \tag{2.3}$$

where n denotes the number of the pulse[1]. Since the Dirac δ-functions have dimensions of frequency, f has units of momentum, which ensures consistency with the force F. Modifying Hamiltonian (2.2) by substituting F for the periodic kicks described by Eq. (2.3), the classical δ-kicked rotor is defined by the Hamiltonian

$$H_{\delta\text{kr}} = \frac{J^2}{2I} - fR\cos\theta \sum_{n=0}^{\infty} \delta(t - nT). \tag{2.4}$$

In this chapter, we introduce the classical description of the δ-kicked rotor. In the next section, we evaluate the dynamics due to Hamiltonian (2.4) by using Hamilton's equations

[1]Formal explorations of Hamiltonian (2.4) frequently consider the sum $\sum_{n=-\infty}^{\infty} \delta(t-nT)$ [6]. However, when considering dynamics beginning at time $t = 0$, the time evolution is independent of whether the lower limit of the sum is $n = -\infty$ or $n = 0$.

of motion.

2.3 Hamilton's equations of motion

In this section we will show that the dynamics of the δ-kicked rotor are described by a single variable κ, known as the stochasticity parameter. Hamilton's equations of motion allow the time-evolutions of the canonically conjugate position and momentum variables to be determined from the Hamiltonian [6, 72].

For the classical δ-kicked rotor, we find that the angular position evolution is given by

$$\frac{d\theta}{dt} = \frac{\partial H_{\delta\mathrm{kr}}}{\partial J} = \frac{J}{I}. \tag{2.5}$$

We interpret from Eq. (2.5) that between the kicks, θ evolves linearly with time. The angular momentum is found to evolve according to

$$\frac{dJ}{dt} = -\frac{\partial H_{\delta\mathrm{kr}}}{\partial \theta} = fR\sin\theta\sum_{n=0}^{\infty}\delta(t-nT). \tag{2.6}$$

Both Eqns. (2.5) and (2.6) are consistent with the definition from Hamiltonian (2.4) that during the period of free evolution, no force acts to modify J. For times $t = nT$ the δ-functions take an infinite value, which results in J having an instantaneous discontinuity[2].

We now wish to solve Hamilton's equations of motion in order to predict the dynamics of the classical δ-kicked rotor. We evaluate the evolution over the duration from the time instantaneously preceding one kick to just before the next. We thus integrate Eqs. (2.5) and (2.6) over one time period T to reveal the mapping

$$\begin{aligned}\theta_{n+1} - \theta_n &= \int_{(nT)^-}^{([n+1]T)^-} dt\frac{d\theta}{dt};\\ J_{n+1} - J_n &= \int_{(nT)^-}^{([n+1]T)^-} dt\frac{dJ}{dt}.\end{aligned} \tag{2.7}$$

The subscripts n denote a kick occurring at time $t = nT$, with the integral's lower limit defined to be infinitesimally before this kick, as denoted by $(nT)^-$. The subsequent kick at time $(n+1)T$ does not contribute to the integral, as the upper limit $t = ([n+1]T)^-$ is

[2]The energy of the system is modified with each kick, due to the explicit time dependence that appears in the δ-function term of Hamiltonian (2.4). In Section 4.2.4, we address the validity of the δ-function approximation to the laser-driven atomic physics experiments that are considered in this thesis.

defined just before that kick occurs. Thus, these integrals describe the dynamics due to a δ-kick, followed by a period of free evolution. An equivalent expression to Hamiltonian (2.4) for the δ-kicked rotor is obtained by solving equations (2.7), which reveals the iterative definition

Solving Eqs. (2.7) we obtain an equivalent, iterative definition of the δ-kicked rotor:

$$\begin{aligned} \theta_{n+1} - \theta_n &= \frac{J_{n+1}T}{I}; \\ J_{n+1} - J_n &= fR\sin\theta_n. \end{aligned} \tag{2.8}$$

To simplify this map we express Eqs. (2.8) in terms of dimensionless quantities with the rescaling

$$J' = \frac{JT}{I}. \tag{2.9}$$

We thus obtain the Chirikov-Taylor standard map [6–8],

$$\begin{aligned} \theta_{n+1} &= \theta_n + J'_{n+1}; \\ J'_{n+1} &= J'_n + \kappa\sin\theta_n. \end{aligned} \tag{2.10}$$

We observe that there is exactly one dimensionless free parameter,

$$\kappa = fR\frac{T}{I}, \tag{2.11}$$

which governs the system dynamics. The term standard map highlights the fact that it describes a broad range of dynamical systems, which have been studied exhaustively [8, 73]. Applications reduced to the standard map include: microwave ionisation of Rydberg atoms [74]; electron-transport in resonant tunnelling in diodes [75]; and comet dynamics in the solar system [76]. In the next section we examine how the value of the stochasticity parameter κ influences the dynamics described by the classical δ-kicked rotor Hamiltonian (2.4).

2.4 Phase space

The δ-kicked rotor is completely described by its angular position and angular momentum, which is equivalent to a point in a (θ, J') phase space. In this section, we explore the effect on the dynamics due to the periodic kicks, which modify the angular momentum,

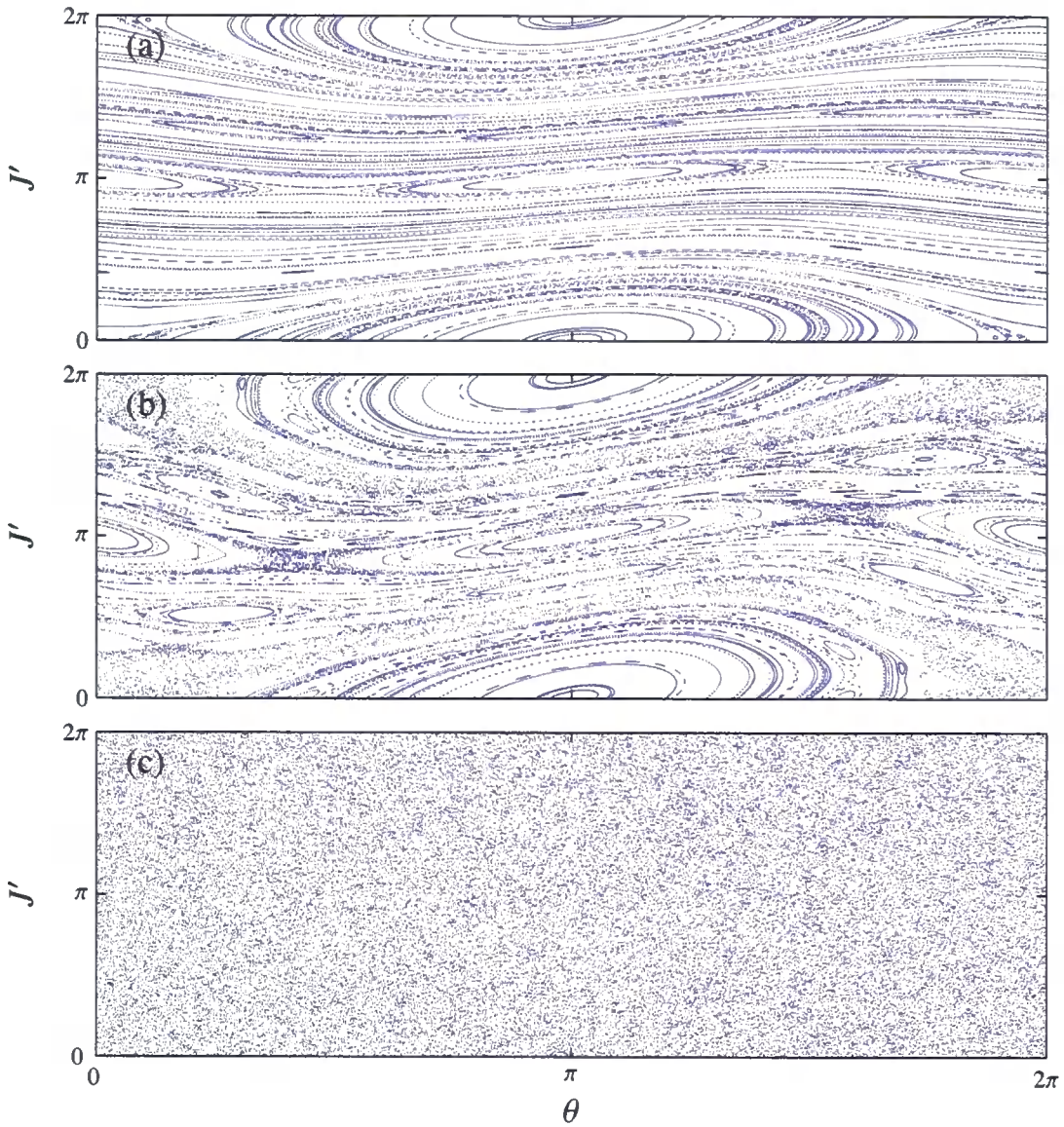

Figure 2.2: The standard map (2.10). Poincaré sections for the classical δ-kicked rotor, with stochasticity parameter (a) $\kappa = 0.5$, (b) $\kappa = 0.971635$, and (c) $\kappa = 16\pi^2/5$. A total of $\mathcal{N} = 100$ initial states are uniformly distributed, with the phase space trajectories shown by the blue dots. The Chirikov-Taylor standard map is iterated up to $n = 500$.

as described by Hamiltonian (2.4).

It is convenient to examine a subset of the phase space by constructing a diagram known as a Poincaré section. In Fig. 2.2, each dot within the phase space indicates the state of the system following an iteration of the standard map (2.11). We evaluate the phase space trajectories of the standard map (2.10) over $n = 500$ iterations, for a range of

values of stochasticity parameter κ. A total of $\mathcal{N} = 100$ initial conditions were randomly assigned values of $(\theta_{n=0}, J'_{n=0})$.

A stable trajectory is characterised by closed curves, which dominate the phase space for low values of the stochasticity parameter, as seen for $\kappa = 0.5$ in Fig. 2.2(a).

A chaotic time evolution is indicated by points which appear distributed at random. The transition from stability to chaos is predicted to occur in a critical region located $0.971635\cdots \leq \kappa_c < 63/64$ [77–79], such that the chaotic region dominates for $\kappa > \kappa_c$. In Fig. 2.2(b), for $\kappa = 0.971635$, we observe isolated stable regions, surrounded by chaotic points.

Setting $\kappa = 16\pi^2/5 \approx 31.58$ in Fig. 2.2(c), all trajectories are found to be chaotic[3]. For the remainder of this thesis, we focus on large values of the stochasticity parameter, for which the classical regime is chaotic.

2.5 Summary

In this chapter the classical δ-kicked rotor was defined by Hamiltonian (2.4). Due to the time periodicity of the system, it is convenient to derive the iterative description known as the Chirikov-Taylor standard map (2.10). The degree of chaos is quantified by the stochasticity parameter κ. In the next chapter, we formulate the δ-kicked rotor from a quantum mechanical perspective.

[3]This value of κ imposed by Eq. (3.26) is consistent with experimental parameters [16–21, 55–60].

Chapter 3

The quantum δ-kicked rotor

3.1 Overview

Quantum mechanical counterparts to classically chaotic systems have received substantial attention, in order to explore and interpret quantum phenomena. In Chapter 2, we demonstrated that the classical δ-kicked rotor as an example of a simple classical system that exhibits chaotic time evolution. In this chapter, we introduce the quantum δ-kicked rotor as a basic tool for studying quantum regimes which have a classically chaotic counterpart.

Understanding the relationship between classically chaotic systems and their quantum mechanical counterpart is instrumental to the development of quantum physics [80–83]. Quantum systems do not adopt the behaviour used to define classical chaos, to the extent that M. Berry made this distinction by introducing the terminology quantum chaology [84].

A quantum signature known as localisation has been discovered in condensed matter physics with the prediction by P. W. Anderson [85] that classically diffusive processes are suppressed in random lattices. A mapping of the quantum δ-kicked rotor to the Anderson localisation model was studied by collaboration between Fishman, Grempel and Prange, as published in Refs. [86–88]. Anderson localisation has applications to semiconductor physics, with the experimental observation of a metal-insulator transition studied by considering the dependence of the quantum δ-kicked rotor evolution upon the kick strength [89, 90]. Localisation has been demonstrated for laser-driven atomic ensembles [45–52, 91–95].

The quantum δ-kicked rotor is an example of a system that has been extensively

studied. Quantum resonance features, as first studied by G. Casati, F. M. Izrailev and D. Shepelyansky [9–12], have been analysed in detail by S. Wimberger *et. al.* [30–34], and I. Dana *et. al.* [23–29].

3.2 Model Hamiltonian

The quantum analogue to the classical δ-kicked rotor (2.4) can be described by the Hamiltonian,

$$\hat{H}_{\delta\mathrm{kr}} = \frac{\hat{J}^2}{2I} - fR\cos\hat{\theta}\sum_{n=0}^{\infty}\delta(t-nT), \tag{3.1}$$

with quantisation imposed by the commutation relation

$$\left[\hat{\theta},\hat{J}\right] = i\hbar. \tag{3.2}$$

3.2.1 Quantum transformation

Following the procedure from Section 2.3 for the standard map, the equivalent quantum transformation to Eq. (2.9),

$$\hat{J}' = \frac{\hat{J}T}{I}, \tag{3.3}$$

rescales the commutation constraint to

$$\left[\hat{\theta},\hat{J}'\right] = i\hbar\frac{T}{I} \equiv i\bar{k}. \tag{3.4}$$

We wish to investigate the quantum δ-kicked rotor in the regime for which the classical counterpart is chaotic, as shown in Fig. 2.2(c). We explore the dependence upon the stochasticity parameter κ, and the rescaled Planck's constant $\bar{k}$, both dimensionless quantities that may be freely varied. The quantum kicked rotor was first considered by G. Casati *et. al.* in 1979 [9][1].

[1]We investigate the realisation of the standard map from the context of atomic physics, with results for the δ-kicked rotor found in Chapter 10. By varying the pulse period, fractional quantum resonance features were discovered by G. Casati *et. al.* [9]. High-order quantum resonance results are presented in Chapter 11 for the general case of a system known as the δ-kicked accelerator.

3.2.2 Angular momentum

In quantum mechanics, we note that $\hat{J}$, the z-component of the angular momentum, has a discrete spectrum of eigenstates $|j\rangle$, such that

$$\hat{J}|j\rangle = \hbar j|j\rangle, \tag{3.5}$$

where j is restricted to integer values [96, 97]. The rescaled angular momentum operator also has a discrete eigenstate spectrum, as seen by,

$$\hat{J}'|j\rangle = \frac{\hat{J}T}{I}|j\rangle = \frac{T}{I}\hbar j|j\rangle = \bar{k}j|j\rangle. \tag{3.6}$$

3.3 Floquet analysis

The time evolution of a wave-vector $|\Psi\rangle$, described by Hamiltonian $\hat{H}$, is governed by the time-dependent Schrödinger equation [98],

$$i\hbar\frac{d}{dt}|\Psi(t)\rangle = \hat{H}(t)|\Psi(t)\rangle. \tag{3.7}$$

The time-evolution operator of the quantum δ-kicked rotor, defined from just before one kick to just before the next, is given by

$$\hat{F}_{\delta\text{kr}} = \hat{E}_T\hat{K}_\delta. \tag{3.8}$$

This is known as a Floquet operator [99], which is partitioned into two separate parts: the kicking operator, $\hat{K}_\delta$, followed by the free evolution operator, $\hat{E}_T$.

3.3.1 Evolution between kicks: $\hat{E}_T$

Between kicks, the Hamiltonian, $\hat{H} = \hat{J}^2/2I$, is time-independent. The solution to the Schrödinger equation at time $nT < t < (n+1)T$ is evaluated as[2],

$$|\Psi(t)\rangle = \exp\left(-\frac{i}{\hbar}\frac{\hat{J}^2}{2I}t\right)|\Psi(nT^+)\rangle, \tag{3.9}$$

[2]An exponential function of operators is defined by the Taylor series expansion $e^{\hat{A}} = \sum_{b=0}^{\infty}\hat{A}^b/b!$.

where $t = nT^+$ indicates the time infinitesimally after the kick that occurs at time $t = nT$. The free evolution over one time period is therefore obtained to be,

$$\hat{E}_T = \exp\left(-\frac{i}{\hbar}\frac{\hat{J}^2}{2I}T\right). \tag{3.10}$$

3.3.2 Evolution due to one δ-kick: $\hat{K}_\delta$

In order to describe the system evolution resulting from an isolated individual kick, we follow the treatment of S. A. Gardiner [13], for which we integrate the Schrödinger equation over the infinitesimal time interval of a kick. This is evaluated explicitly by parametrising the time interval by τ. Substituting Eq. (3.1) into (3.7) and integrating, we obtain

$$i\hbar\int_{nT-\tau}^{nT+\tau} dt\frac{d}{dt}|\Psi(t)\rangle = \frac{\hat{J}^2}{2I}\int_{nT-\tau}^{nT+\tau} dt|\Psi(t)\rangle - fR\cos\hat{\theta}\int_{nT-\tau}^{nT+\tau}\sum_{n=0}^{\infty}\delta(t-nT)|\Psi(t)\rangle. \tag{3.11}$$

In order to impose the δ-kick approximation, we restrict this integration to an infinitesimal interval. Taking the limit that τ tends to zero, the contribution to the integral from the angular momentum term tends to zero. Thus, the Schrödinger equation that we wish to integrate reduces to

$$i\hbar\frac{d}{dt}|\Psi(t)\rangle = -fR\cos\hat{\theta}\delta(t-nT)|\Psi(nT)\rangle. \tag{3.12}$$

The Dirac δ-function is constrained by the normalisation condition

$$\int_{-\infty}^{\infty}\delta(t)dt = 1, \tag{3.13}$$

which is consistent with a step function of width 2τ and height $1/2\tau$, for arbitrarily small τ [13]. We therefore approximate (3.12) by the differential equation

$$i\hbar\frac{d}{dt}|\Psi(t)\rangle = -\frac{fR}{2\tau}\cos\hat{\theta}|\Psi(nT)\rangle, \tag{3.14}$$

which has solution

$$|\Psi(nT+\Delta t)\rangle = \exp\left(\frac{i}{\hbar}fR\cos\hat{\theta}\frac{\Delta t}{2\tau}\right)|\Psi(nT)\rangle. \tag{3.15}$$

The integration takes place over time interval 2τ, and so we set $\Delta t = 2\tau$, and allow $\tau \to 0$.

Thus, the effect of a δ-kick is represented by the operator

$$\hat{K}_\delta = \exp\left(\frac{i}{\hbar} f R \cos\hat{\theta}\right). \tag{3.16}$$

3.3.3 Combining the time evolution results: $\hat{F}_{\delta\mathrm{kr}}$

By combining Eqs. (3.10) and (3.16), the time evolution operator over one time period T is determined to be

$$\hat{F}_{\delta\mathrm{kr}} = \underbrace{\exp\left(-\frac{i}{\hbar}\frac{\hat{J}^2}{2I}T\right)}_{\hat{E}_T}\underbrace{\exp\left(\frac{i}{\hbar} f R \cos\hat{\theta}\right)}_{\hat{K}_\delta}. \tag{3.17}$$

In terms of the rescaled parameters from (2.11) and (3.4),

$$\hat{F}_{\delta\mathrm{kr}} = \exp\left(-\frac{i}{k}\frac{\hat{J}'^2}{2}\right)\exp\left(i\frac{\kappa}{k}\cos\hat{\theta}\right). \tag{3.18}$$

As a result, the quantum δ-kicked rotor is characterised by two dimensionless parameters: the stochasticity parameter κ, and the rescaled Planck's constant k. The quantum map corresponding to standard map (2.10), as introduced by G. Casati *et. al.* [9], is given by

$$|\Psi_{n+1}\rangle = \hat{F}_{\delta\mathrm{kr}}|\Psi_n\rangle. \tag{3.19}$$

After n iterations of the Floquet operator, the initial state $|\Psi_0\rangle$ becomes

$$|\Psi_n\rangle = \hat{F}^n_{\delta\mathrm{kr}}|\Psi_0\rangle. \tag{3.20}$$

3.4 Quantum resonant effects

In this thesis, we use the term quantum resonance effect to refer to particular features that are exhibited by quantum δ-kicked systems. This includes quantum resonance and quantum antiresonance phenomena, which we demonstrate in this section for the simple case of the quantum δ-kicked rotor.

Acting upon the angular momentum eigenstates with free evolution operator (3.10),

and substituting for the eigenvalues in Eq. (3.6), we obtain,

$$\hat{E}_T|j\rangle = \exp\left(-\frac{i}{k}\frac{\hat{j}'^2}{2}\right)|j\rangle = \exp\left(-i\frac{kj^2}{2}\right)|j\rangle. \tag{3.21}$$

By choosing a classically chaotic parameter, we explore the dependence of the time evolution upon the rescaled Planck's constant. This allows the quantum mechanical nature of the quantum δ-kicked rotor to be explored. We observe quantum resonance and quantum antiresonance features by restricting the rescaled Planck's constant to

$$k = 2\pi\ell, \tag{3.22}$$

defining ℓ to be an integer. In Section 3.6, we explain that k may be experimentally modified by tuning the pulse period T. Therefore, we consider ℓ to be a measure of the time between the pulses. By imposing integer values ℓ, we may simplify Eq. (3.21) by noting that an even value of j implies that j^2 is also even, and conversely, an odd value of j implies that j^2 is also odd. Hence, $\exp(-i\pi\ell j^2) = \exp(\pm i\pi\ell j)$ and so

$$\hat{E}_T|j\rangle = \exp\left(\pm i\pi\ell j\right)|j\rangle = \exp\left(\pm i\frac{\hat{j}'}{2}\right)|j\rangle. \tag{3.23}$$

Therefore, restricting k to integer multiples of 2π, as with constraint (3.22), we may simplify Eq. (3.21) to

$$\hat{E}_T|j\rangle = (-1)^{\ell j}|j\rangle, \tag{3.24}$$

for which dramatically different features occur depending whether ℓ is even or odd.

3.4.1 Kick strength

Substituting (3.23) into (3.18), the Floquet operator reduces to

$$\hat{F}_{\delta\mathrm{kr}} = \exp\left(\pm i\frac{\hat{j}'}{2}\right)\exp\left(i\frac{\kappa}{k}\cos\hat{\theta}\right). \tag{3.25}$$

We find that subject to constraint (3.22), the Floquet operator depends only upon the single parameter, κ/k, which for experimental realisations is denoted by the kick strength variable ϕ_d. We restrict the study throughout this thesis to the classically chaotic regime,

and have chosen

$$\phi_d = \kappa/k = 0.8\pi, \tag{3.26}$$

as an illustrative value typical of recent experiments [16–18, 21, 55–58, 60]. For $\ell = 2$, it follows that the stochasticity parameter $\kappa = 16\pi^2/5$, as was chosen in Fig. 2.2(c) to illustrate the dynamics of the classical δ-kicked rotor.

3.4.2 Quantum resonance

For even values of ℓ, the evolution operator (3.24) reduces to the identity, and so the Floquet operator is

$$\hat{F}_{\delta\mathrm{kr}} = \exp\left(i\phi_d \cos\hat{\theta}\right), \tag{3.27}$$

for which the system effectively responds only to the δ-kicks.

Applying the Floquet operator n times,

$$\hat{F}^n_{\delta\mathrm{kr}} = \hat{K}^n_\delta = \exp\left(in\phi_d \cos\hat{\theta}\right). \tag{3.28}$$

This effect, known as quantum resonance, may be interpreted to be mathematically equivalent to the application of one kick with n times the kick-strength of ϕ_d.

3.4.3 Quantum antiresonance

We consider the application of the Floquet operator twice,

$$\hat{F}^2_{\delta\mathrm{kr}} = \exp\left(-i\frac{\hat{J}'}{2}\right)\exp\left(i\phi_d\cos\hat{\theta}\right)\exp\left(i\frac{\hat{J}'}{2}\right)\exp\left(i\phi_d\cos\hat{\theta}\right). \tag{3.29}$$

In Appendix A, we derive the displacement operator result (A.4), which simplifies Eq. (3.29) to

$$\hat{F}^2_{\delta\mathrm{kr}} = \exp\left(i\phi_d\cos(\hat{\theta}-\pi\ell)\right)\exp\left(i\phi_d\cos\hat{\theta}\right). \tag{3.30}$$

There are two possible cases to consider, depending on whether ℓ is even or odd:

1. For even values of ℓ, we make the simplification $\cos(\hat{\theta}-\pi\ell) = \cos(\hat{\theta})$, with the result that $\hat{F}^2_{\delta\mathrm{kr}} = \hat{K}^2_\delta$. We saw in Section 3.4.2 that this is characteristic of quantum resonance.

2. In this section, we introduce the phenomenon of quantum antiresonance by examining the case of odd values of ℓ, for which $\cos(\hat{\theta} - \pi\ell) = -\cos(\hat{\theta})$. In this case, the exponential terms in Eq. (3.30) cancel to reveal

$$\hat{F}_{\delta\mathrm{kr}}^2 = 1. \tag{3.31}$$

As a result, after every two kicks, the system is returned to its original state.

3.5 Evolution of an angular momentum eigenstate

Quantum resonant effects are dramatic phenomena observed for the quantum counterpart to a classically chaotic system, which have been studied for a variety of configurations [4–6].

The classical δ-kicked rotor exhibits chaotic trajectories for large values of κ, as demonstrated in Fig. 2.2(c). By imposing quantisation condition (3.2), we may compare the quantum δ-kicked rotor with its classically chaotic counterpart. In the quantum case, the dynamics depend upon k, displaying the effects described in Section 3.4.

The quantum resonance and quantum antiresonance features of the quantum δ-kicked rotor are demonstrated in Fig. 4.2. We quantify the time evolution in terms of $D(j)$, the normalised angular momentum density[3]. We show results for the cases $\ell = 1$ in the left-hand plots, and $\ell = 2$ in the right-hand plots. The initial condition of the zero-momentum eigenstate is shown in Figs. 4.2(a) and (b). The application of Floquet operator (3.18) modifies the momentum distribution, as seen in Figs. 4.2(c) and (d). Quantum antiresonance, characterised by Eq. (3.31), is depicted in Fig. 4.2(e) by the recurrence of the initial state. In contrast, quantum resonance, characterised by Eq. (3.28), is observed in Fig. 4.2(f), as seen by the continued spread in the momentum distribution. The time evolution of the eigenstate displays these quantum resonant effects for subsequent kicks, with the momentum dependence investigated in Chapter 9 for a range of parameters.

3.6 The Talbot time

The Talbot effect is a phenomenon from classical optics, discovered in 1836 [100, 101], and analysed for an extensive variety of optical arrangements [102, 103]. In this section, we

[3]Observables used to analyse the momentum distributions are introduced in Chapter 5.

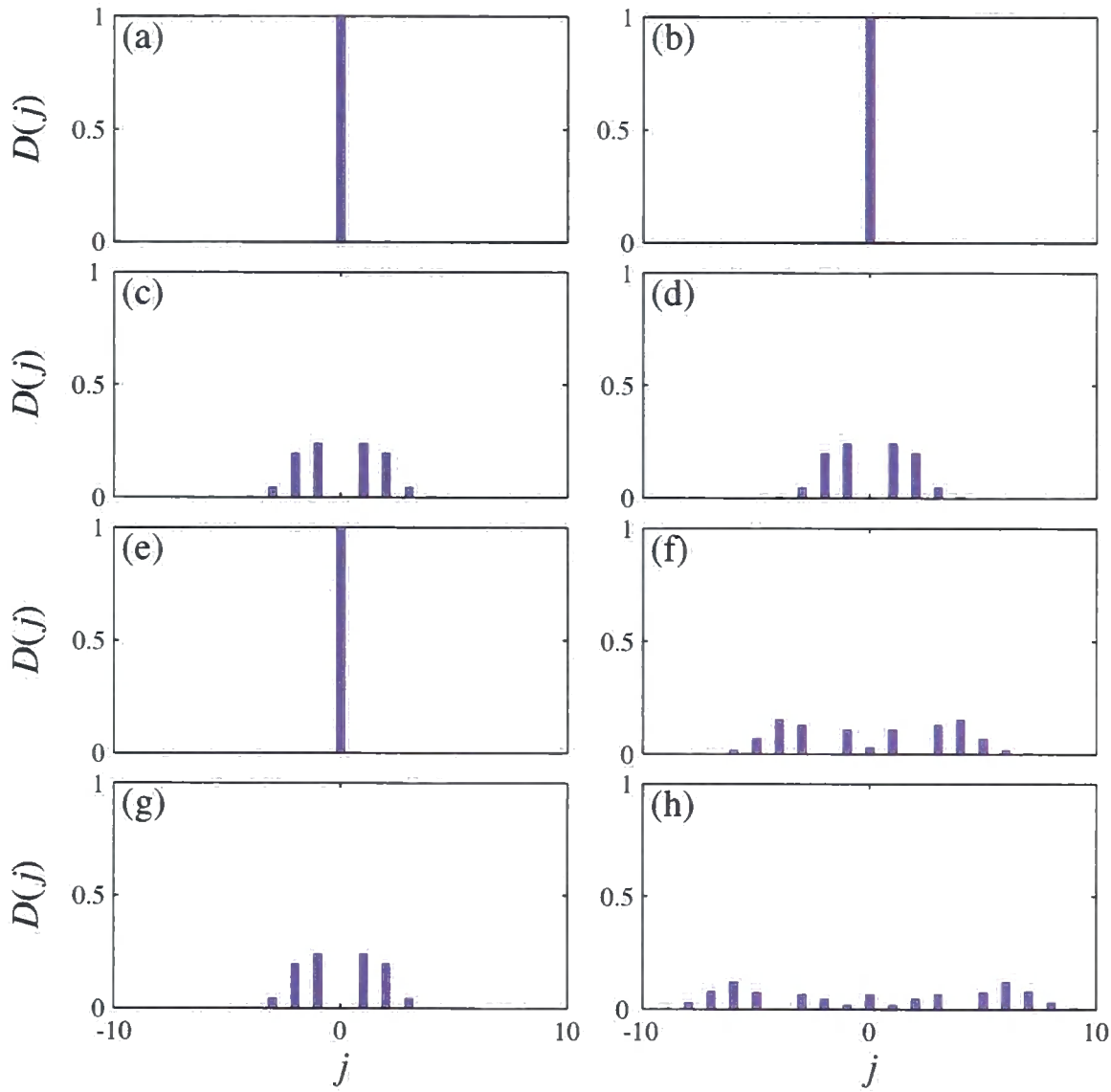

Figure 3.1: The quantum standard map (3.20), with initial eigenstate $|j = 0\rangle$, shown in (a) and (b). The normalised distribution density $D(j)$, is shown evolving over subsequent applications of Floquet operator (3.18), with $n = 1$ (c), (d); $n = 2$ (e), (f); and $n = 3$ (g), (h). Parameters are $\phi_d = \kappa/k = 0.8\pi$, with $k = 2\pi$ (Quantum antiresonance: $\ell = 1$) [left-hand column], and $k = 4\pi$ (Quantum resonance: $\ell = 2$) [right-hand column].

make an analogy with the effect from optics by defining the Talbot time. We demonstrate that an angular momentum eigenstate exhibits the quantum resonant effects introduced in Section 3.4.

In Fig. 4.2, we investigate the dependence of the quantum δ-kicked rotor upon the rescaled Planck's constant, $k = \hbar T/I$. This could be examined by varying the properties of the rotor. However, we choose to keep M and R fixed, constraining the moment of inertia. Therefore, to examine the k dependence, we modify T, the time period between the δ-kicks.

The Talbot time is then defined as

$$T_T \equiv \frac{4\pi I}{\hbar}, \tag{3.32}$$

which is the smallest time between kicks for which we observe quantum resonance. The features described in Section 3.4 may be equivalently characterised in terms of the pulse period

$$T = \frac{\ell T_T}{2}, \tag{3.33}$$

again with even ℓ values corresponding to quantum resonance, and quantum antiresonance observed for odd values of ℓ [104].

3.7 Summary

In this chapter, we have introduced the quantum δ-kicked rotor to analyse the quantum analogue to a classically chaotic regime. We evaluate the time-evolution using Floquet analysis, demonstrating quantum resonance in Section 3.4.2, and quantum antiresonance in Section 3.4.3. In the next chapter we generalise to the δ-kicked accelerator for an atom-optical configuration, incorporating gravitational effects for a finite temperature gas.

Chapter 4

Atom-optical realisation of the δ-kicked accelerator

4.1 Overview

The quantum δ-kicked rotor may be examined by subjecting a dilute atomic gas to a periodically pulsed optical standing wave. This is referred to as the atom-optical configuration. One of the features of such experiments is that the optical standing wave may be oriented vertically, allowing a distribution of atoms to fall under gravity during the optical pulses. This realises the quantum δ-kicked accelerator.

In this chapter, we introduce the δ-kicked accelerator, incorporating gravity into the model derived in Chapter 3. An experimental realisation is presented, for which results are presented in Chapter 7 in the zero-temperature limit, and for a thermal gas in Chapter 8.

4.2 Atom-optical configuration

In this thesis, the dynamics of quantum δ-kicked systems is investigated in the context of atomic physics, due to the advances in laser cooling and trapping that have made it possible to study quantum phenomena [105, 106]. A typical experimental configuration is presented in Fig. 4.1(a), with a summary of the procedure outlined in Fig. 4.1(b). We present a simplified schematic of experimental arrangements performed in Oxford, UK, using caesium [107], and in Austin, Texas, USA, using sodium [108, 109].

A thermal distribution of alkali atoms is confined and Doppler cooled in a magneto-

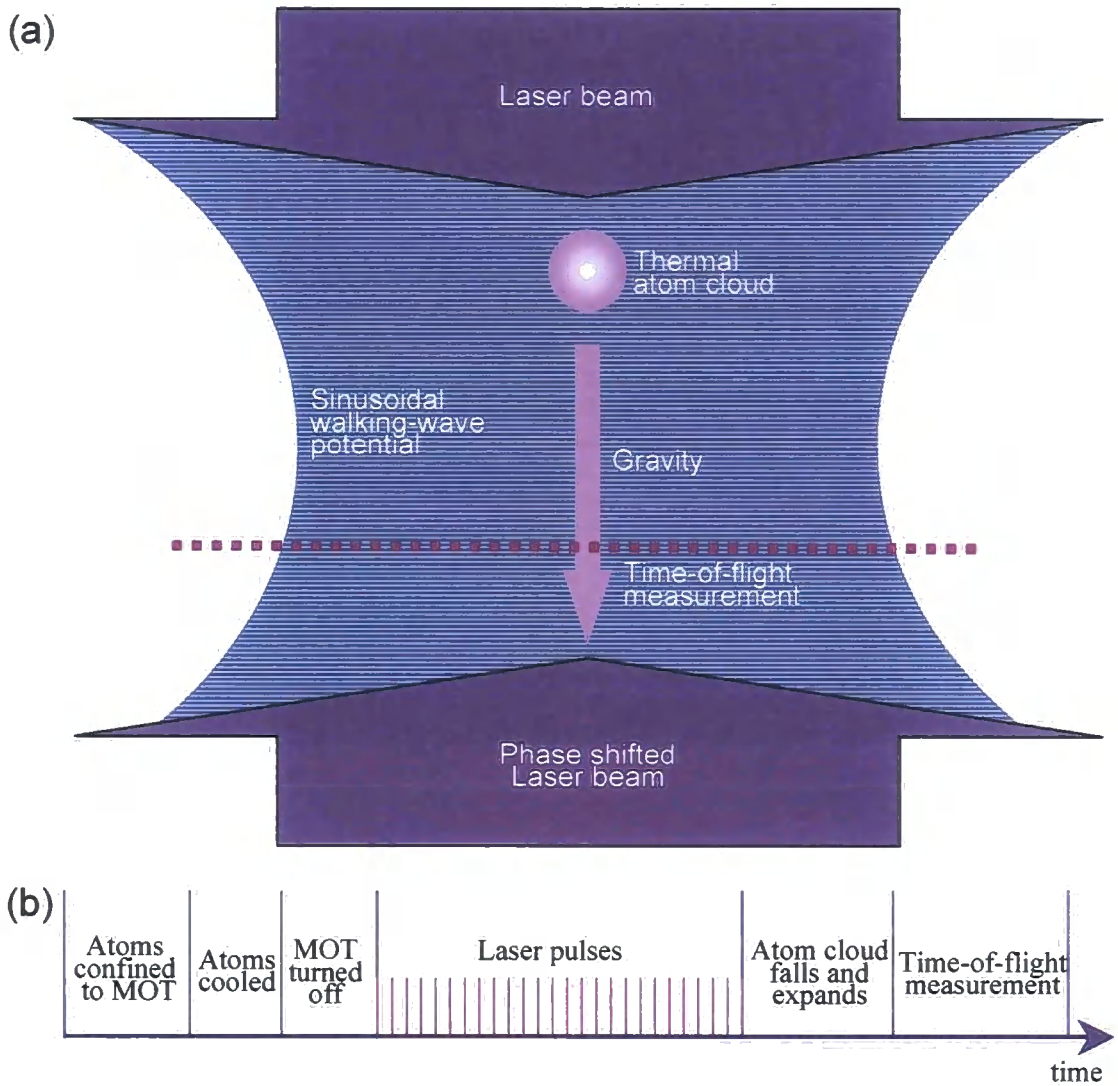

Figure 4.1: Atomic realisation of the δ-kicked accelerator. A schematic for a typical experiment is shown in (a), with the experimental procedure outlined in (b).
A finite temperature cloud of atoms is laser cooled before being exposed to a periodically pulsed sinusoidal potential formed by the interference of two counter-propagating laser beams. The atoms experience a linear acceleration a_ϕ, tuned by phase shifting the laser beams to a walking-wave potential. The laser pulses approximate δ-kicks, exposing the cooled atoms to an environment described by Hamiltonian (4.3). Orienting the system vertically enables the precision measurement of local gravitational acceleration g. Following the pulses, the atoms then fall freely under gravity, allowing the cloud to expand, resulting in the separation of the momentum states. They pass through a time-of-flight beam, enabling the momentum distribution of the atoms to be measured.

optical trap (MOT) [110–113]. Releasing the atom cloud from all external fields, it falls subject to gravity and the potential formed by two periodically pulsed counter-propagating laser beams [114]. We theoretically examine the evolution of the momentum distribution due to the vertically aligned pulsed sinusoidal potential, which we compare with experiment [16–18, 21, 55–57, 64].

Over the duration of the pulses, the position of the atoms is not modified significantly by the interactions with the laser beam. However, the momentum of the atoms provides a signature for quantum resonant effects, which is typically measured using a time-of-flight measurement, as explained in the next section.

4.2.1 Time-of-flight method

Following the laser pulses at time $t = nT$, the momentum distribution is to be measured. The atom cloud is allowed to fall freely, expanding and thus causing the individual momentum states to separate [115]. Treating the subsequent evolution classically, after an evolution of duration τ, the change in the vertical position $z(t)$ for a particular momentum state is given by

$$z(\tau + nT) - z(nT) = \frac{p(nT)\tau}{M}. \tag{4.1}$$

Since the Doppler cooled cloud initially has a narrow distribution in position, after sufficient time for which $\tau \gg nT$, the momentum distribution at $t = nT$ may be inferred from the position distribution at $t = \tau + nT$.

The Burnett group at Oxford made use of the time-of-flight method, resolving the momentum with a precision on the order of $\sim \hbar K$ [107]. This degree of resolution is sufficient for the observation of quantum resonance and quantum antiresonance, as we demonstrate in Chapter 7. We explain in Chapter 10 that there are a variety of experimental techniques available for the preparation of an atomic ensemble with a very narrow momentum distribution, thus ensuring that the temperature is low enough for quantum effects to be observed.

4.2.2 Interactions

In a thermal gas, interactions occur when the constituent atoms collide, distributing their energy and momentum [116]. The experiments in Oxford and Texas were performed using a thermal gas at μK temperatures. Interactions were suppressed by using very dilute samples.

At lower temperatures considered in this thesis, bosonic species form a Bose-Einstein condensate, for which interactions are significant and categorised by s-wave scattering [117]. It is possible to tune the scattering length to zero [118] using Feshbach resonances [119–122], which means that the interactions may be neglected.

The quantum resonance effects which we are interested in observing are most prominent if the interactions are suppressed. We therefore neglect the atom-atom interactions throughout this thesis, as has been justified experimentally for the temperature range considered.

4.2.3 Two-level atom Hamiltonian

The interaction of an accelerating two-level atom exposed to a counter-propagating laser beam potential is represented by the Hamiltonian,

$$\begin{aligned}\hat{H}_{\text{2level}} =& \frac{1}{2}\hbar\omega_0\left(|e\rangle\langle e| - |g\rangle\langle g|\right) + \frac{\hat{p}^2}{2M} + Mg\hat{z} \\ &+ \frac{1}{2}\hbar\Omega_{R1}\left[e^{i(k_L\hat{z}-\omega_L t+\phi_1)}|e\rangle\langle g| + e^{-i(k_L\hat{z}-\omega_L t+\phi_1)}|g\rangle\langle e|\right] \\ &+ \frac{1}{2}\hbar\Omega_{R2}\left[e^{-i(k_L\hat{z}+\omega_L t-\phi_2)}|e\rangle\langle g| + e^{i(k_L\hat{z}+\omega_L t-\phi_2)}|g\rangle\langle e|\right],\end{aligned} \tag{4.2}$$

which describes the energy of the atoms occupying ground state $|g\rangle$ and excited state $|e\rangle$. The energy difference between the internal atomic levels is $\hbar\omega_0$, with the laser frequency ω_L corresponding to a wave-vector along the vertical direction of magnitude k_L. The difference between the transition frequency and the laser frequency is known as the detuning, defined $\Delta \equiv \omega_0 - \omega_L$. The lasers have phases ϕ_1 and ϕ_2, and Rabi frequencies Ω_{R1} and Ω_{R2}. The gravitational potential is expressed in terms of g, the local gravitational acceleration.

The laser beam potential in Eq. (4.2) does not vary with time. In the next section, we justify the assumptions imposed to model the time dependence of the Hamiltonian.

4.2.4 The Raman-Nath regime

In this thesis, we model the experimental setup theoretically by comparing it to the quantum δ-kicked rotor described in Chapter 3. We approximate the finite laser-pulse duration to be instantaneous, modelling the time periodic laser potential by a sequence of Dirac δ-functions, as imposed by Eq. (2.3) for the classical δ-kicked rotor.

The δ-kick assumption is justified provided that over the duration of the pulse, the atoms do not move a distance that is comparable with the wavelength of the laser beam. An atom satisfying this criterion is said to be in the Raman-Nath regime.

Provided that the atom cloud is sufficiently cooled, atoms which lie outside of the Raman-Nath regime serve only to reduce the effective value of the stochasticity parameter, and characteristic δ-kick behaviour continues to be exhibited in the momentum distribution [48]. In experiment, it has been verified that it is possible to sufficiently cool a cloud of alkali atoms, such that the δ-kick assumption is valid [57].

By modifying Hamiltonian (4.2) to incorporate the time periodicity of the laser pulses, it is possible to derive the atom-optical δ-kicked accelerator, which we discuss in the next section.

4.3 Model Hamiltonian

The atom-optical δ-kicked accelerator is described by the Hamiltonian,

$$\hat{H}_{\delta\mathrm{ka}} = \frac{\hat{p}^2}{2M} + Ma\hat{z} - \hbar\phi_d \cos(K\hat{z}) \sum_{n=0}^{\infty} \delta(t - nT), \tag{4.3}$$

which is subject to the quantisation condition

$$[\hat{z}, \hat{p}] = i\hbar. \tag{4.4}$$

In this section we compare the atom-optical δ-kicked accelerator to the quantum δ-kicked rotor from Chapter 3.

Hamiltonian (4.3) is derived in Appendix B by imposing the time dependence assumptions from Section 4.2.4 to the two-level atom Hamiltonian (4.2). We express this Hamiltonian in the reference frame of the falling atoms, and adiabatically eliminate the transition between $|g\rangle$ and $|e\rangle$.

Hamiltonian (4.3) has the form of the quantum δ-kicked rotor (3.1), with the following significant modifications:

1. The conjugate linear momentum $\hat{p}$ has a continuous spectrum of eigenvalues, in contrast to the discretely quantised angular momentum $\hat{J}$. In Section 4.5, we assess the dependence upon the momentum of the time evolution for a single atom.

2. The position operator $\hat{z}$, aligned along the vertical spatial axis, replaces the angular position operator $\hat{\theta}$.

3. We consider the linear motion by atoms, each with mass M, as opposed to the moment of inertia I of a rotor. The equivalence of the mathematics relating a rotor to a periodic linear system enables Bloch theory to be invoked in Section 4.4.2.

4. The model is generalised to incorporate a uniform acceleration a along the vertical direction. For a vertically aligned configuration, $a = g - a_\phi$, such that this quantity is composed of the local gravitational acceration g together with a phase term a_ϕ. Proof of principle experiments have demonstrated that precision measurement of g is possible by tuning the value of a_ϕ to reveal the quantum resonance effects [56]. The prospect for precision measurement of gravity with the quantum δ-kicked accelerator is assessed in Chapter 12.

5. The standing-wave pulses have wavenumber K, which ensures a dimensionless argument for the cosine function. In Chapter 12, we present values of K used in experiment, and explain how this is relevant to enable the prospect of precision measurement.

6. In Section 3.4, we explained that quantum resonant effects occur for large values of the quantity ϕ_d, which is defined by Eq. (3.26) in terms of both the stochasticity parameter and the rescaled Planck's constant. From the context of atomic physics, the physical interpretation of this dimensionless variable is to quantify the strength of the individual pulses from a laser beam. In Section B.6, we demonstrate that ϕ_d is the amplitude of the phase modulation, defining the effective potential depth $\phi_d \equiv \Omega_R^2 t_p / 8\Delta$ [57], for Rabi frequency Ω_R and detuning Δ. The δ-kick term contributes a phase to the system wavefunction, which has been experimentally studied over the range $0.3\pi \leq \phi_d \leq 1.5\pi$ [16, 57]. In order to remain consistent throughout this thesis, we constrain $\phi_d = 0.8\pi$, typical to experiments from atomic physics [16–18, 21, 55–58, 60].

As explained in this section, the experimental configuration introduced in Section 4.2 can be modelled by δ-kicked accelerator Hamiltonian (4.3). In the next section, we follow the procedure from Chapter 3 to derive the time evolution operator, which we then apply to an individual eigenstate in Section 4.5.

4.4 The evolution operator in the accelerating frame

The δ-kicked accelerator Hamiltonian is expressed in the reference frame of the falling atoms. We derive a time evolution operator for the atom-optical configuration, which incorporates the acceleration dependence of the falling atoms.

4.4.1 The periodic Hamiltonian in the accelerating frame

In this section, we make use of operator identities from Appendix A to derive the δ-kicked accelerator Hamiltonian from the reference frame which is accelerating with the centre of mass of the cloud of falling atoms. The unitary operator

$$U(t) = \exp\left(\frac{i}{\hbar} Ma\hat{z}t\right). \tag{4.5}$$

is used to transform Eq. (4.3). Using the displacement operator (A.3) and Hamiltonian transformation (A.8), we obtain

$$\tilde{H}_{\delta\mathrm{ka}} = \frac{(\hat{p} - Mat)^2}{2M} - \hbar\phi_d \cos(K\hat{z}) \sum_{n=0}^{\infty} \delta(t - nT). \tag{4.6}$$

Comparing this to Hamiltonian (4.3), the linear position dependent term has been removed and the momentum operator was displaced. Therefore, as a consequence of performing unitary operation (4.5), Hamiltonian (4.6) is periodic in position space. We exploit the periodicity in position to simplify the mathematics describing the evolution of the atoms.

4.4.2 Quasimomentum conservation: Bloch theory

It is convenient to separate the momentum into discrete and continuous components,

$$\hat{p} = \hbar K(\hat{k} + \hat{\beta}), \tag{4.7}$$

where the eigenvalues of $\hat{k}$ are integers, with the eigenvalues of $\hat{\beta}$ restricted to the interval $-1/2 < \beta \leq 1/2$. The Hamiltonian in the reference frame accelerating with the falling

atoms is then given by

$$\tilde{H}_{\delta\text{ka}} = \frac{[\hbar K(\hat{k}+\hat{\beta}) - Mat]^2}{2M} - \hbar\phi_d \cos(K\hat{z}) \sum_{n=0}^{\infty} \delta(t - nT). \tag{4.8}$$

The spatial periodicity of Hamiltonian (4.8) is analogous to the spatial periodicity observed in solid state systems [123, 124]. Therefore, Bloch theory applies to this system, which demonstrates a conservation law for quasimomentum, as explained below.

Hamiltonian (4.8) commutes with the quasimomentum operator $\hat{\beta}$ [1, 19, 125, 126]. Therefore, the quasimomentum is conserved in the accelerating frame, and the laser field induces coupling only between momentum eigenstates differing in momenta by integer multiples of $\hbar K$.

In Section 4.4.4, we evaluate the time evolution operator by making use of the periodicity in the momentum.

4.4.3 Momentum units

The δ-kick component of Hamiltonian (4.8) shows that the laser pulse establishes a sinusoidal potential, with periodicity set by wavevector $K = 2k_L$. We used this result to demonstrate that quasimomentum is conserved, which enables the atom-optical δ-kicked accelerator to be described using essentially the same mathematics as in Chapter 3.

Due to the momentum of an atom being changed discretely, it is convenient to use Eq. (6.2.3) to define units of momentum. To present the results of this thesis, we express the momentum in terms of $\hbar K$, which is twice the photon recoil $\hbar k_L$ [127].

4.4.4 The transformed Floquet operator

Following the same procedure as in Chapter 3, the time-evolution operator corresponding to Hamiltonian (4.3), defined from just before one kick to just before the next is determined to be

$$\hat{F}_{\delta\text{ka}} = \exp\left(-\frac{i}{\hbar}\left[\frac{\hat{p}^2}{2M} + Ma\hat{z}\right]T\right) \exp\left(i\phi_d \cos(K\hat{z})\right). \tag{4.9}$$

The Floquet operator exhibits quantum resonant effects by setting

$$T = \ell\frac{T_T}{2} = \ell\frac{2\pi M}{\hbar K^2}, \tag{4.10}$$

where the Talbot time for the atom optical configuration is defined [1]

$$T_T = \frac{4\pi M}{\hbar K^2}, \tag{4.11}$$

with ℓ a positive integer. For a single eigenstate, which has a particular value of quasi-momentum β, we demonstrate in Appendix C that the time evolution operator may be expressed as

$$\tilde{F}_n(\beta) = \exp\left(-i\pi\left[(1+2\beta)\ell - (2n-1)\,\Omega\right]\hat{k}\right)\exp\left(i\phi_d\cos(K\hat{z})\right). \tag{4.12}$$

The dependence upon kick number n introduces a time argument into the evolution operator, which means that technically it is not a Floquet operator. However, in the frame of the falling atoms, the transformed Floquet operator (4.12) is useful for investigating the kick-to-kick evolution. The dependence upon the acceleration is parametrised by the dimensionless quantity

$$\Omega \equiv \frac{2\pi\ell^2 aM^2}{\hbar^2 K^3}. \tag{4.13}$$

In this thesis, we investigate the time evolution as a function of this rescaled effective gravity parameter.

4.5 Time evolution

To evaluate the application of time evolution operator (4.12), we begin by simplifying the initial distribution by considering an idealised system prepared in a momentum eigenstate:

$$|\Psi(t=0)\rangle = |k+\beta\rangle. \tag{4.14}$$

In this chapter, we present results for a single initial momentum eigenstate, constraining the study to a particular β subspace. Gaining an understanding of the evolution of state (4.14) enables the evolution of a general distribution to be inferred.

4.5.1 Momentum eigenstate evolution

The evolution of state (4.14) can be determined at time $t = nT$, by consecutively applying transformed Floquet operators defined by Eq. (4.12). More formally,

$$|\Psi(t = nT)\rangle = \tilde{\mathcal{F}}_n(\beta)|k + \beta\rangle, \tag{4.15}$$

where

$$\tilde{\mathcal{F}}_n(\beta) = \tilde{F}_n(\beta)\tilde{F}_{n-1}(\beta)\tilde{F}_{n-2}(\beta)\ldots\tilde{F}_1(\beta). \tag{4.16}$$

The conservation of quasimomentum, as shown in Section 4.4.2, allows the evolved momentum eigenstate (4.15) to be expanded into its constituent momentum eigenstate components,

$$|\Psi(t = nT)\rangle = \sum_{j=-\infty}^{\infty} c_{kj}(\beta, nT)|j + \beta\rangle, \tag{4.17}$$

where the probability amplitudes $c_{kj}(\beta, nT)$ are given by

$$c_{kj}(\beta, nT)\delta(\beta - \beta') = \langle j + \beta'|\tilde{\mathcal{F}}_n(\beta)|k + \beta\rangle. \tag{4.18}$$

Taking the complex conjugate, the evolution of $\langle k + \beta|$ is given by

$$\langle\Psi(t = nT)| = \sum_{j=-\infty}^{\infty} c^*_{kj}(\beta, nT)\langle j + \beta|. \tag{4.19}$$

In the next chapter, we use Eq. (4.17) and (4.19) to demonstrate that the evolution of an individual momentum eigenstate is given by

$$D_j(\beta, t = nT) = \sum_{k=-\infty}^{\infty} |c_{kj}(\beta, nT)|^2 D_k(\beta, t = 0). \tag{4.20}$$

In Appendix D, we summarise the analytic forms of these matrix elements for various initial parameters. In the next section, we evaluate the time evolution for a momentum eigenstate, and demonstrate an application known as velocity selection, which has been observed in experiment [128, 129].

4.5.2 Velocity selection

In this section, we demonstrate quantum resonant effects for the δ-kicked rotor by setting $\Omega = 0$. We examine the β dependence by investigating the time dependence for individual eigenstates. An arbitrary momentum distribution is composed from many atoms with varying speeds, which we analyse by comparing the evolution for each β subspace.

The observation of quantum resonance and quantum antiresonance has been achieved experimentally. The dependence upon the momentum, or equivalently the velocity, provides applications to both precision measurement of momentum and the selection of a chosen momentum class.

Quantum resonant effects for the atom-optical δ-kicked rotor

In Fig. 4.2, we show the evolution of the momentum distribution for the atom-optical δ-kicked rotor, where $T = T_T/2$ ($\ell = 1$). The initial momentum distributions are shown for eigenstates $p = 0$ in Fig. 4.2(a), and $p = 0.5\ \hbar K$ in Fig. 4.2(b). The distributions are shown evolving by the application of successive kicks. As seen from Fig. 4.2, quantum antiresonance is observed in the $\beta = 0$ subspace, characterised by the recurrence of the initial state every two pulses. Quantum resonance is shown in the $\beta = 1/2$ subspace, with the atom cloud expanding ballistically.

Quantum resonant effects are observed as a function of momentum, as expected from the β dependence of Eq. (4.12). This can be compared to the quantum resonant effects presented in Fig. 4.2, for which the value of ℓ was varied.

Experimental observation of velocity dependent quantum resonant effects

The ability to select the velocity of atoms to high precision allows quantum systems to be manipulated. These results are consistent with an experiment by the Hoogerland group in Auckland, in which they observe these quantum resonant phenomena for a range of β values [128, 129]. They propose applications which can make use of these results: velocity selection of narrow parts of an initial distribution, or conversely, the accurate measurement of a momentum distribution.

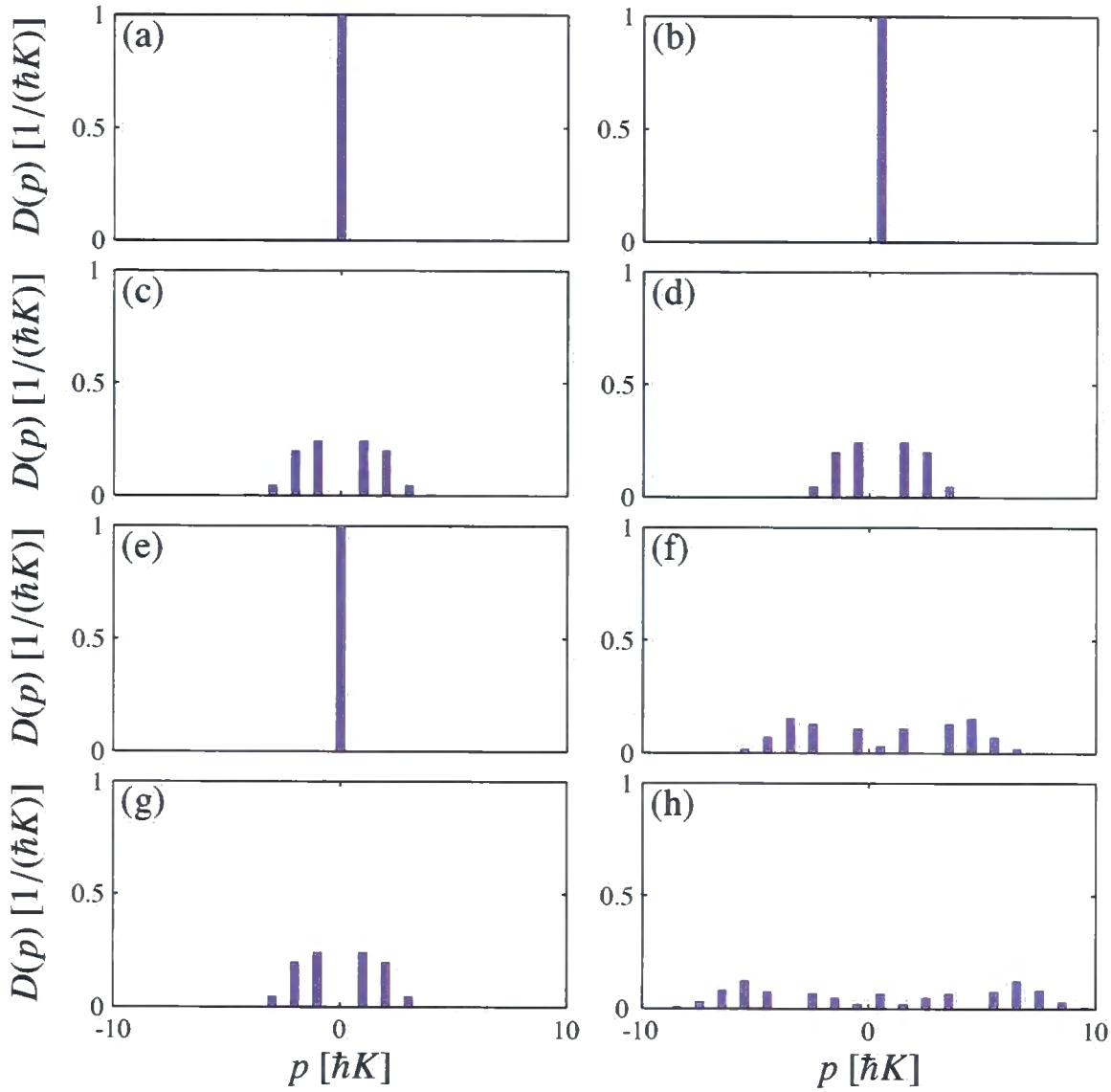

Figure 4.2: The momentum distribution of eigenstate (4.14), initially with $p = 0$ [left-hand column] and $p = 0.5\ \hbar K$ [right-hand column]. The initial state (a), (b), is evolved by subsequent applications of evolution operator (4.12), with $n = 1$ (c), (d); $n = 2$ (e), (f); and $n = 3$ (g), (h). Parameters are $\phi_d = 0.8\pi$, $T = T_T/2$ ($\ell = 1$), and $\Omega = 0$. Note the similarity to Fig. , for which the quantum resonant and quantum antiresonant effects correspond to particular values of the pulse period T.

4.6 Summary

We have derived the time evolution operator for the atom-optical δ-kicked accelerator. In Chapter 7 we show results for various system parameters, adopting the idealisation of the

zero temperature limit by restricting the system to the $\beta = 0$ subspace. In Chapter 6 we explain how a finite temperature gas was numerically simulated, with results for the high temperature limit presented in Chapter 8. A detailed analysis of the quasimomentum dependence for the individual eigenstates is given in Chapter 9. We present the temperature dependence of the δ-kicked rotor in Chapter 10, and the δ-kicked accelerator in Chapter 11.

Chapter 5

Quantum observables

5.1 Overview

In this chapter, we introduce the quantum observables which we use to characterise the time-evolution:

1. Momentum distribution.
2. Momentum moments.
3. Momentum cumulants.

We derive analytic expressions for the observables for two limiting cases:

1. The ultracold regime: In Section 5.4, we consider the idealisation of a zero temperature gas by evaluating the evolution of an individual momentum eigenstate. In this regime, the quantum resonant effects are well resolved. The low temperature analytic results are compared with simulation results in Chapter 7.
2. The thermal regime: In Section 5.5, we consider a broad initial momentum distribution composed from an incoherent mixture of momentum eigenstates. The quantum resonant effects average out. The high temperature analytic results are compared with simulation results in Chapter 8.

5.2 Definitions

The momentum distribution is determined from a matrix known as the density operator, which we time evolve using the transformed Floquet operator. To analyse the momentum

distribution, we define momentum moments and momentum cumulants, which we evaluate in this thesis for a variety of values for the system parameters.

5.2.1 Momentum distribution definition

A finite temperature atomic gas consists of an incoherent mixture of momentum eigenstates. In this section, we express the momentum distribution by defining a matrix known as the density operator. We expose this matrix to the sequence of transformed Floquet operators given in Eq. (4.16), and then extract the resulting momentum distribution.

Density operator definition

To investigate the temperature dependence of the dynamics within a gas, the initial distribution may be expressed in terms of an incoherent sum of orthogonal plane waves. This defines the density operator [99],

$$\hat{\rho}(t=0) \equiv \hbar K \int dp|p\rangle D(p)\langle p|. \tag{5.1}$$

The momentum density $D(p)$ is normalised, with units of inverse momentum $(\hbar K)^{-1}$, and may be extracted from the diagonal elements of the density operator. The integral in Eq. (5.1) is multiplied by $\hbar K$ which ensures that the density operator matrix elements are dimensionless.

In terms of the discrete and continuous variables introduced in Eq. (6.2.3), the momentum distribution is given by $D(p) = D_k(\beta)/\hbar K$, and the integral becomes

$$\hat{\rho}(t=0) = \int_{-1/2}^{1/2} d\beta \sum_{k=-\infty}^{\infty} |k+\beta\rangle D_k(\beta)\langle k+\beta|. \tag{5.2}$$

For each individual eigenstate, the value of β remains constant, due to quasimomentum conservation as described in in Section 4.4.2. As a result, the time evolution may be evaluated by examining the change in the contribution to the sum of the discrete momentum variable k.

Density operator time dependence

The time evolution of momentum operator $\hat{\rho}$ allows the time dependence of the density $D(p)$ to be evaluated. The time evolution of the individual momentum eigenstates are

given by Eq. (4.17) and (4.19). Hence the time-evolved density operator is obtained by substituting state (4.17) for the eigenstates in Eq. (5.2), which reveals

$$\hat{\rho}(t=nT) = \int_{-1/2}^{1/2} d\beta \sum_{k=-\infty}^{\infty} \sum_{j=-\infty}^{\infty} c_{kj}(\beta, nT)|j+\beta\rangle D_k(\beta) \sum_{j'=-\infty}^{\infty} c^*_{kj'}(\beta', nT)\langle j'+\beta'|. \quad (5.3)$$

Final momentum density

We extract the time evolved distribution from the diagonal elements of evolved density operator matrix (5.3). Setting $j = j'$ and $\beta = \beta'$, we obtain

$$D_j(\beta, t=nT) = \sum_{k=-\infty}^{\infty} |c_{kj}(\beta, nT)|^2 D_k(\beta, t=0). \quad (5.4)$$

In Appendix D, we explain that

$$D_j(\beta, t=nT) = \sum_{k=-\infty}^{\infty} J^2_{j-k}(\omega) D_k(\beta, t=0), \quad (5.5)$$

where ω is presented for a variety of system parameters.

As a result, the laser pulses directly modify the momentum of the atoms, and therefore the distributions in momentum space reveal the effect of the Floquet kicks. This quantity, which was plotted in Figs. 4.2 and 4.2, is used throughout this thesis to emphasise the effect of the laser pulses upon a cloud of cold atoms.

5.2.2 Momentum moment definition

The qth-order momentum moment is defined

$$\langle \hat{p}^q \rangle_n \equiv \int dp D(p) p^q, \quad (5.6)$$

which gives a measure of the shape of a distribution. The subscript n denotes the application of time-evolution operator $\tilde{\mathcal{F}}_n(\beta)$, defined in Eq. (4.16), which corresponds to time $t = nT$. In terms of the discrete and continuous variables given in Eq. (6.2.3), and substituting for the time evolved distribution (5.4), the momentum moments are given by

$$\langle \hat{p}^q \rangle_n = (\hbar K)^q \int_{-1/2}^{1/2} d\beta \sum_{j,k=-\infty}^{\infty} J^2_{j-k}(\omega) D_k(\beta)(j+\beta)^q. \quad (5.7)$$

The momentum moments are defined by distribution $D(p)$, and conversely, an arbitrary momentum distribution may be constructed from a complete set of momentum moments, $\{\langle\hat{p}^q\rangle_n\}$, for $q = 1, \ldots, \infty$. We therefore use the momentum moments in this thesis to concisely convey the distribution data. In the next section, we define momentum cumulants, which are mutually independent, and therefore provide a useful measure for describing the shape of the momentum distribution.

5.2.3 Momentum cumulant definition

In this section we define and interpret the momentum cumulants, explaining the significance of interpreting these observables.

Significance of the momentum cumulants

A qth-order momentum moment $\langle\hat{p}^q\rangle_n$ is dependent upon all moments up to order $(q-1)$. As a consequence, $\langle\hat{p}^2\rangle_n$ and $\langle\hat{p}^4\rangle_n$ are not independent quantities. Using an iterative process, mutually independent cumulants $\langle\langle\hat{p}^q\rangle\rangle_n$ can be constructed from the moments $\langle\hat{p}\rangle_n, \langle\hat{p}^2\rangle_n, \ldots, \langle\hat{p}^q\rangle_n$ [19, 130–132].

The energy of the atoms in the cloud has a mean value proportional to $\langle\langle\hat{p}^2\rangle\rangle_n$, with a standard deviation proportional to $\langle\langle\hat{p}^4\rangle\rangle_n$. Therefore, the cumulants relate directly to experimentally observable quantities.

Iterative momentum cumulant definition

Momentum cumulants are related to the moments by the recursion formula [130]:

$$\langle\langle\hat{p}^q\rangle\rangle_n = \langle\hat{p}^q\rangle_n - \sum_{k=1}^{q-1} \binom{q-1}{k-1} \langle\langle\hat{p}^k\rangle\rangle_n \langle\hat{p}^q - k\rangle_n \tag{5.8}$$

We express the momentum cumulants in terms of the momentum moments as seen below:

1. The first-order cumulant $\langle\langle\hat{p}\rangle\rangle_n$ is equivalent to the mean $\langle\hat{p}\rangle_n$.

2. The second-order cumulant $\langle\langle\hat{p}^2\rangle\rangle_n$ is the variance, as defined by

$$\langle\langle\hat{p}^2\rangle\rangle_n \equiv \langle\hat{p}^2\rangle_n - \langle\hat{p}\rangle_n^2. \tag{5.9}$$

3. The third-order cumulant, known as the skew, characterises the balance of the distribution about the mean, and is given by

$$\langle\langle\hat{p}^3\rangle\rangle_n \equiv \langle\hat{p}^3\rangle_n - 3\langle\hat{p}\rangle_n\langle\hat{p}^2\rangle_n + \langle\hat{p}\rangle_n^3. \tag{5.10}$$

4. The fourth-order momentum cumulant, also known as the kurtosis, is defined

$$\langle\langle\hat{p}^4\rangle\rangle_n \equiv \langle\hat{p}^4\rangle_n - 4\langle\hat{p}^3\rangle_n\langle\hat{p}\rangle_n + 12\langle\hat{p}^2\rangle_n\langle\hat{p}\rangle_n^2 - 3\langle\hat{p}^2\rangle_n^2 - 6\langle\hat{p}\rangle_n^4. \tag{5.11}$$

Interpretation of the momentum cumulants

The shape of the momentum distribution may be constructed from the set $\{\langle\langle\hat{p}^q\rangle\rangle_n\}$, for $q = 1, \ldots, \infty$. Since the momentum cumulants are mutually independent, finer detail is added by the higher-order cumulants, and therefore a good approximation to the original distribution is provided by the first few cumulants.

For a symmetric distribution, its odd ordered momentum cumulants are zero [3]. Futhermore, if a momentum distribution is symmetric initially, for $\Omega = r/s$, it must evolve to a symmetric distribution at intervals of s kicks [2]. As we explain in Section 5.3, we are justified in modelling a thermal gas by a Gaussian momentum distribution. Therefore, we are only interested in the even-ordered momentum cumulants.

The second-order cumulant characterises the width of a distribution. Low values of $\langle\langle\hat{p}^2\rangle\rangle_n$ correspond to narrow distributions, while high values of $\langle\langle\hat{p}^2\rangle\rangle_n$ correspond to wide distributions.

The fourth-order cumulant characterises the pointedness of a distribution. Negative values of $\langle\langle\hat{p}^4\rangle\rangle_n$ correspond to flat distibutions, which highlight quantum resonance features. Positive values of $\langle\langle\hat{p}^4\rangle\rangle_n$ correspond to peaked distributions, which emphasise the predominance of quantum antiresonance effects.

Momentum cumulant simplification for a symmetric distribution

The odd moments remain relatively insignificant in comparison to the rapidly growing even moments [3]. Therefore, the second-order cumulant simplifies to

$$\langle\langle\hat{p}^2\rangle\rangle_n = \langle\hat{p}^2\rangle_n, \tag{5.12}$$

and the fourth-order cumulant simplifies to

$$\langle\langle \hat{p}^4 \rangle\rangle_n = \langle \hat{p}^4 \rangle_n - 3\langle \hat{p}^2 \rangle_n^2. \tag{5.13}$$

The second and fourth-order cumulants are numerically evaluated in Chapter 11 to present the temperature dependence results for an atom cloud subject to δ-kicked accelerator Hamiltonian (4.3).

The set of cumulants used to convey the distribution data, may be truncated by neglecting odd cumulants and high-order cumulants. In this thesis, we find that it is sufficient to describe all of the results using $\langle \hat{p}^2 \rangle_n$ and $\langle\langle \hat{p}^4 \rangle\rangle_n$.

5.3 Initial conditions

The initial momentum distribution $D(p)$ is defined for a finite temperature gas according to Maxwell-Boltzmann statistics. In this chapter, we analytically evaluate the system dynamics for two limiting cases: the ultracold and thermal limits.

The Maxwell-Boltzmann distribution

A general distribution is expressed by its component eigenstates. We approximate a thermal gas to a Gaussian initial momentum distribution $D(p) = D_k(\beta)/\hbar K$,

$$D_k(\beta) = \frac{1}{w\sqrt{2\pi}} \exp\left(\frac{-[k+\beta]^2}{2w^2}\right), \tag{5.14}$$

which the distribution width is parametrised by the dimensionless quantity w. The initial variance is given by $\langle\langle \hat{p}^2 \rangle\rangle_{n=0} = w^2(\hbar K)^2$, and all other momentum cumulants take the value of zero.

In this thesis we explore the temperature dependence for an initial distribution of non-interacting particles with a Maxwell-Boltzmann temperature defined in terms of w by [116]

$$\mathcal{T}_w = \frac{w^2(\hbar K)^2}{M k_B}. \tag{5.15}$$

Individual momentum eigenstates

We approximate a finite temperature cloud by considering its constituent momentum eigenstates. In the limit that the system can be described by a single momentum eigen-

state, the momentum distribution reduces to a Dirac δ-function. In this limit, we set the distribution width $w = 0$, which corresponds to a zero temperature idealisation. This well approximates an ultracold Bose-Einstein condensate, provided that interactions may be neglected, as explained in Section 4.2.2.

Investigating the evolution of individual momentum eigenstates allows the dependence upon the quasimomentum to be evaluated. For example, the $p = 0.5\ \hbar K$ momentum eigenstate is shown in Fig. 4.2(b) for which the momentum distribution is described by the Dirac δ-function, $D(p) = \delta(p - \hbar K/2)$, or equivalently $D_k(\beta) = \delta_{k0}\delta(\beta - 1/2)$, for which the Kronecker δ-function δ_{k0} denotes the discrete momentum $k = 0$.

The evolution of an individual eigenstate is analytically evaluated in Section 5.4, and compared with numerical results analysing the β dependence in Chapter 9.

Finite temperature

High temperature results are obtained by taking the limit that $w \gg 1/2\sqrt{2}\pi\ell$, for which the dynamics is described by a superposition of the quantum resonant effects. We have found an analytic solution for the δ-kicked accelerator at high temperatures for specific values of the system parameters, with results summarised in Section 5.5. We compare the analytic description of the thermal limit in Chapter 8.

The temperature dependence of the δ-kicked rotor is examined in Chapter 10. We explore fractional quantum resonances of the δ-kicked accelerator in Chapter 11, evaluating the sensitivity to Ω in Chapter 12, with a view to assess the prospect for precision measurement of local gravitational acceleration.

5.4 The ultracold limit

We study the evolution of momentum moments as a useful way to characterize the atomic dynamics. If the state of the atoms is initially prepared in the momentum eigenstate $|k + \beta\rangle$, the qth-order momentum moment after time $t = nT$ is found by simplifying Eq. (5.7) to

$$\langle \hat{p}^q \rangle_n = (\hbar K)^q \sum_{j=-\infty}^{\infty} J_{j-k}^2(\omega)(j + \beta)^q, \tag{5.16}$$

where ω is a function dependent upon the value of the acceleration parameter Ω. In this section, we express $\langle \hat{p}^2 \rangle_n$ and $\langle \hat{p}^4 \rangle_n$ in terms of ω, with a solution derived for fractional quantum resonant effects.

5.4.1 Evaluating $\langle\hat{p}^2\rangle_n$ for the $\beta = 0$ eigenstate

Setting $\beta = 0$, we can analytically solve Eq. (5.16) for $q = 2$ using the Bessel function identity $\sum_{j=-\infty}^{\infty} j^2 J_j^2(\eta) = \eta^2/2$ [1, 133], from which we obtain

$$\langle\hat{p}^2\rangle_n = (\hbar K)^2 \frac{\omega^2}{2}. \tag{5.17}$$

5.4.2 Evaluating $\langle\hat{p}^4\rangle_n$ for the $\beta = 0$ eigenstate

Using the Bessel function identity $\sum_{j=-\infty}^{\infty} j^4 J_j^2(\eta) = 3\eta^4/8 + \eta^2/2$ [2], we find that Eq. (5.16) with $q = 4$ in the ultracold limit has the solution

$$\langle\hat{p}^4\rangle_n = (\hbar K)^4 \left(\frac{3\omega^4}{8} + \frac{\omega^2}{2}\right). \tag{5.18}$$

5.4.3 Quantum resonance

In the case where $\Omega = 1/s$, Eq. (5.17) and (5.18) can be evaluated analytically. For even $s(1-\ell)$, and n an integer multiple of s, we explain with Eq. (D.10) that

$$\omega = \frac{\phi_d n}{\sqrt{s}}. \tag{5.19}$$

from which we find for $q = 2$ that

$$\langle\hat{p}^2\rangle_n = (\hbar K)^2 \frac{\phi_d^2 n^2}{2s}. \tag{5.20}$$

Equation (5.20) describes quadratic growth in the second-order momentum moment, and therefore the kinetic energy, with a growth rate inversely proportional to s.

Similarly, for $q = 4$, we find that

$$\langle\hat{p}^4\rangle_n = (\hbar K)^4 \left(\frac{3\phi_d^4 n^4}{8s^2} + \frac{\phi_d^2 n^2}{2s}\right). \tag{5.21}$$

To leading order, Eq. (5.21) describes quartic growth with a rate inversely proportional to s^2.

For the initially infinitely narrow momentum distributions considered here, the evolution of the fourth-order momentum moment does not provide significant additional information over and above that extracted from the second-order momentum moment

evolution. However, as we show in Section 5.5, the situation is quite different for initially broad, thermal momentum distributions, so we have included a description of the fourth-order momentum moment dynamics here for completeness.

5.4.4 Quantum antiresonance

In Appendix D, we describe fractional quantum antiresonance effects, for which, first-order quantum antiresonances are of particular importance to this thesis, as depicted in Fig. 4.2, and characterised by the Floquet operator identity (3.31).

For a zero-momentum eigenstate, quantum antiresonance occurs for odd integers ℓ. At the quantum antiresonance, with odd values of n, the matrix element is given by $|c_{0j}(0)|^2 = J_j^2(\phi_d)$. Therefore, following the first kick, the results are the same for a quantum resonance, as is demonstrated by comparing the momentum distributions in Fig. 4.2(c) and 4.2(d). For even values of n, the momentum distribution returns to the initial condition, as is verified from the probability amplitudes given by $|c_{0j}(0)|^2 = \delta_{j0}$. The second-order momentum moment evolves as

$$\langle \hat{p}^2 \rangle_n = (\hbar K)^2 \frac{1}{4} \phi_d^2 [1 - (-1)^n]. \tag{5.22}$$

The oscillation of the second-order momentum moment with period $2T$ is illustrated in Chapter 7 by selecting values of ℓ and Ω which correspond to a quantum antiresonance.

5.4.5 Evaluating $\langle\langle \hat{p}^q \rangle\rangle_n$ for the $\beta = 0$ eigenstate

Before considering the high-temperature limit of the cumulant dynamics, it is first instructive to consider the zero-temperature limit where the initial state is a zero-momentum eigenstate. The initial state is symmetric in p so $\langle\langle \hat{p}^2 \rangle\rangle_n = \langle \hat{p}^2 \rangle_n$ is given by Eq. (5.20) which is valid for n an integer multiple of s (where $\Omega = 1/s$).

Substituting Eqs. (5.20) and (5.21) into Eq. (5.13), we find that the fourth-order momentum cumulant for the ultracold limit is given by

$$\langle\langle \hat{p}^4 \rangle\rangle_n = (\hbar K)^4 \left(-\frac{3\phi_d^4 n^4}{8s^2} + \frac{\phi_d^2 n^2}{2s} \right), \tag{5.23}$$

where again n is an integer multiple of s.

5.5 The thermal limit

Deriving analytic expressions for the momentum moment evolution of a finite temperature gas is more involved than arriving at the zero temperature results (5.20) and (5.21). However, it is possible to derive such expressions for integer and half-integer values of Ω, as detailed in Appendix E.

In this section, we consider the quantum resonant features by setting ℓ to be an integer. Also, setting the initial Gaussian momentum distribution (5.14) to be broad, we demonstrate that by choosing w to be large, the dynamics of the finite temperature case approaches the thermal limit.

5.5.1 Derivation for $\langle \hat{p}^2 \rangle_n$ in the thermal limit

In Appendix E, we derive $\langle \hat{p}^2 \rangle_n$ in the thermal limit for both integer and half-integer values of Ω. We derive Eqs. (E.33) and (E.37),

$$\langle \hat{p}^2 \rangle_n = (\hbar K)^2 \left(w^2 + \frac{\phi_d^2}{2} n \right), \tag{5.24}$$

which are the same for both cases. Note that for the case of the half-integer Ω result, Eq. (5.24) only applies for even values of n. However, we observe that the results are equivalent where the theory is applicable.

In Chapter 8, we present a numerical study of the thermal regime, and demonstrate that $\langle \hat{p}^2 \rangle_n$ is independent of Ω. We therefore refer to Ω as being unresolvable using $\langle \hat{p}^2 \rangle_n$ in the thermal limit.

For the classical δ-kicked rotor, the second-order moment for a thermal momentum distribution evolves according to Eq. (5.24) [46, 73]. Therefore, the quantum nature of the time-evolution is not revealed for a thermal gas by using second-order observables. Therefore, we evaluate the fourth-order momentum moments and cumulants.

5.5.2 Derivation for $\langle \hat{p}^4 \rangle_n$ in the thermal limit

We now summarise the analytic results derived in Appendix E for the fourth-order momentum moment. For integer values of Ω we find in Section E.3 that

$$\langle \hat{p}^4 \rangle_n = (\hbar K)^4 \left(\frac{\phi_d^4}{4} n^3 + \frac{\phi_d^4}{8} n + \frac{\phi_d^2}{2} n + 3w^2 \phi_d^2 n + 3w^4 \right). \tag{5.25}$$

For half-integer values of Ω we find in Section E.4, that with the restriction that n is even, the evolution of the fourth-order momentum moment is given by

$$\langle \hat{p}^4 \rangle_n = (\hbar K)^4 \left(\frac{\phi_d^4}{8} n^3 + \frac{5\phi_d^4}{8} n + \frac{\phi_d^2}{2} n + 3w^2 \phi_d^2 n + 3w^4 \right). \tag{5.26}$$

The leading order term of the fourth-order momentum moment evolution is cubic in n, with the leading-order coefficient for half-integer Ω is exactly half the leading-order coefficient in the integer Ω case. Therefore, it is possible to distinguish between fractional quantum resonances with integer and half-integer values of Ω using $\langle \hat{p}^4 \rangle_n$. This quantity may be used to distinguish between Ω values for a finite temperature atom cloud, as we verify numerically in Chapter 8. We refer to Ω as being resolvable using $\langle \hat{p}^4 \rangle_n$ in the thermal limit.

5.5.3 Evaluating $\langle\langle \hat{p}^q \rangle\rangle_n$ in the thermal limit

We define a Gaussian initial momentum distribution by asserting the standard deviation of $w(\hbar K)$, as explained in Section 5.3. In the thermal limit, where w is taken to be large, the momentum variance is given by Eq. (5.24). Subtracting the initial value gives

$$\Delta\langle\langle \hat{p}^2 \rangle\rangle_n = \langle\langle \hat{p}^2 \rangle\rangle_n - \langle\langle \hat{p}^2 \rangle\rangle_0 = (\hbar K)^2 \frac{\phi_d^2 n}{2}, \tag{5.27}$$

which is independent of w. Note that Eq. (5.27) applies to both integer and half-integer values of Ω, although for half-integer values of Ω it applies only for even values of n. In Chapter 8, we demonstrate that a finite temperature gas with a large value of w approaches the thermal limit. We observe that our numerical calculations strongly indicate that Eq. (5.27) should apply for all values of Ω, including irrational values of Ω. In Chapters 10 and 11, we explore the transition between the ultracold and thermal regimes.

A Gaussian distribution has no non-zero cumulants of order greater than two so, when considering an initially Gaussian momentum distribution, we have $\langle\langle \hat{p}^4 \rangle\rangle_0 = 0$. For integer values of Ω, we substitute Eqs. (5.24) and (5.25) into Eq. (5.13) and find that

$$\langle\langle \hat{p}^4 \rangle\rangle_n = (\hbar K)^4 \left(\frac{\phi_d^4}{4} n^3 - \frac{3\phi_d^4 n^2}{4} + \frac{\phi_d^4}{8} n + \frac{\phi_d^2}{2} n \right), \tag{5.28}$$

which is also independent of w. An analogous expression for half-integer values of Ω can

be found by substituting Eqs. (5.24) and (5.26) into Eq. (5.13) to yield

$$\langle\langle\hat{p}^4\rangle\rangle_n = (\hbar K)^4 \left(\frac{\phi_d^4}{8} n^3 - \frac{3\phi_d^4 n^2}{4} + \frac{5\phi_d^4}{8} n + \frac{\phi_d^2}{2} n \right), \tag{5.29}$$

which is valid for even n. For general rational values of Ω, we expect that the change in the momentum cumulants, compared to their initial values, will again be independent of w, for w sufficiently large.

5.6 Summary

We have quantified the quantum resonance effects in terms of three momentum observables: distribution, moments and cumulants. A qth-order momentum moment $\langle\hat{p}^q\rangle_n$ is dependent upon all moments up to order $(q-1)$. In particular, $\langle\hat{p}^2\rangle_n$ and $\langle\hat{p}^4\rangle_n$ are not independent quantities. Using an iterative process, mutually independent cumulants $\langle\langle\hat{p}^q\rangle\rangle_n$ can be constructed from the moments $\langle\hat{p}\rangle_n, \langle\hat{p}^2\rangle_n, \ldots, \langle\hat{p}^q\rangle_n$ [19, 130–132].

In the ultracold limit, we observe fractional quantum resonant effects. We interpret from Eqs. (5.20) and (5.22) that it is possible to resolve the value of Ω from a momentum distribution by calculating its corresponding second-order moment. The fourth-order moments and cumulants are derived for comparison with the finite-temperature results. We note from Eq. (5.23) that quantum resonance is characterised by a negative value of $\langle\langle\hat{p}^q\rangle\rangle_n$, due to a broadening of the distribution with each kick.

Taking the thermal limit, we see from Eqs. (5.24), (5.25), and (5.26), that the evolution of the momentum moments depends explicitly on w. For this reason, we defined a lower bound for the large-w limit of the momentum moment evolutions. We showed explicitly by Eqs. (5.27), (5.28), and (5.29), that for integer and half-integer values of Ω, this difficulty does not arise if we consider the change in the momentum cumulants from their initial value. In this way it is possible to have a well defined high-temperature limit.

In the thermal limit it is not possible to resolve Ω using the second-order momentum cumulant, as seen from Eq. (5.27). We find that Ω may be resolved in the thermal limit using the fourth-order momentum cumulant. In the next chapter, we present the numerical method used to simulate the finite-temperature gas subject to a periodically pulsed laser beam potential.

Chapter 6

Numerical implementation

6.1 Overview

In this thesis, we investigate the interaction of a cloud of cold atoms, subject to gravity and a periodically pulsed sinusoidal potential. The momentum distribution of the atoms within the cloud is evolved using the transformed Floquet operator (C.6),

$$\tilde{F}_n = \exp\left(-\frac{i}{\hbar}\left[\frac{\hat{p}^2}{2m}T - \frac{\hat{p}}{2}a(2n-1)T^2\right]\right)\exp\left(i\phi_d\cos(k\hat{z})\right). \tag{6.1}$$

In this chapter, we explain the code implemented in Matlab, which is a matrix oriented computing environment and programming language. We have developed a simulation of the atom-optical δ-kicked accelerator, which we use to obtain the numerical results presented in this thesis.

6.2 Variable definitions

The program specifications have been selected to simulate the δ-kicked accelerator with the numerical errors reduced to the extent that the quantum resonant effects are clearly resolvable. In this section, we explain how the code was structured to allow the system parameters to be systematically varied.

6.2.1 Input parameters

Parameters allow control of both the evolution operator and the momentum distribution. Evolution operator variables which include the properties of the laser are given in Table 6.1. Terms describing the momentum distribution which defines the properties of the atom cloud are given in Table 6.2. These tables show the variables, together with the notation used to label them. The algebra labels are used for equations, whilst the Matlab variable names in this chapter represent the variables for commands used to generate the data.

Physical quantity	Variable	Matlab name
Kick number	n	`n`
Gravity	Ω	`Omega`
Kick period	ℓ	`ell`
Kick strength	$\phi_d = 0.8\pi$	`phid`

Table 6.1: Parameters for evolution operator.

Physical quantity	Variable	Matlab name
Initial distribution width	w	`w`
Sample size	$\mathcal{N} = 10000$	`sample`
Discrete momentum range	$-250 \leq k \leq 250$	`k`
Number of bins	$B = 101$	`bin`
Quasimomentum range	$-0.5 < \beta \leq 0.5$	`beta`

Table 6.2: Parameters for initial Gaussian momentum distribution.

We systematically modify the parameters in order to investigate the dependence of the system upon each of them. A typical choice of variables may be selected with the commands:

```
clear all
% Evolution operator
    n_max  = 100; n = 0:n_max;  % Laser kicks
    Omega  = 1/4;               % Gravity parameter
    ell    = 2;                 % Number of half-Talbot times
    phid   = 0.8*pi;            % Laser intensity
```

```
% Momentum distribution
    w      = 2.5;                 % Standard deviation of initial Gaussian.
    sample = 10000;               % Number of plane waves
    k_limit= 250; k_range = -k_limit:k_limit; % Discrete basis
    bin    = 101;                 % Quasimomentum basis
```

6.2.2 Initial momentum distribution

Subjecting single eigenstates to operator (6.1) allows the evolution to be examined over the range of the quasimomentum basis. We have examined various shapes of the momentum distribution, including Gaussian, uniform and symmetric distributions. In this thesis we present results for a Gaussian initial momentum distribution, as explained in Section 5.3.

A Monte Carlo approach is used to populate the initial distribution in preference to a grid-based method, which could produce sampling errors if, for example, a disproportionate number of grid points were to coincide with strongly quantum resonant values of the initial momentum. The initial condition consists of $\mathcal{N}$ plane waves, from which k and β are extracted. The density operator is defined by a sparse 2D matrix, with a 1 denoting the k value for each plane wave, typically with the initial values close to $k = 0$, such that

$$\texttt{density\_operator} = \left.\underbrace{\begin{bmatrix} 0 & \cdots & 0 & 0 & 0 & 0 & 1 & 0 & 0 & 0 & 0 & \cdots & 0 \\ 0 & & 0 & 0 & 0 & 0 & 0 & 1 & 0 & 0 & 0 & & 0 \\ 0 & & 0 & 0 & 0 & 0 & 1 & 0 & 0 & 0 & 0 & & 0 \\ 0 & & 0 & 0 & 0 & 0 & 1 & 0 & 0 & 0 & 0 & & 0 \\ 0 & & 0 & 0 & 0 & 1 & 0 & 0 & 0 & 0 & 0 & & 0 \\ 0 & & 0 & 0 & 0 & 0 & 1 & 0 & 0 & 0 & 0 & & 0 \\ \vdots & \iddots & & & & & & & & & & \ddots & \vdots \\ 0 & \cdots & 0 & 0 & 0 & 0 & 1 & 0 & 0 & 0 & 0 & \cdots & 0 \end{bmatrix}}_{k}\right\} \texttt{sample}. \quad (6.2)$$

We have found that a discrete basis ranging from $-250 \leq k \leq 250$ is sufficient for kick numbers up to $n = 100$. This is implemented by the segment of code:

```
initial_distribution = randn(1, sample) * w;      % Gaussian distribution
beta = mod(initial_distribution+0.5,1) - 0.5;     % Extract quasimomentum
```

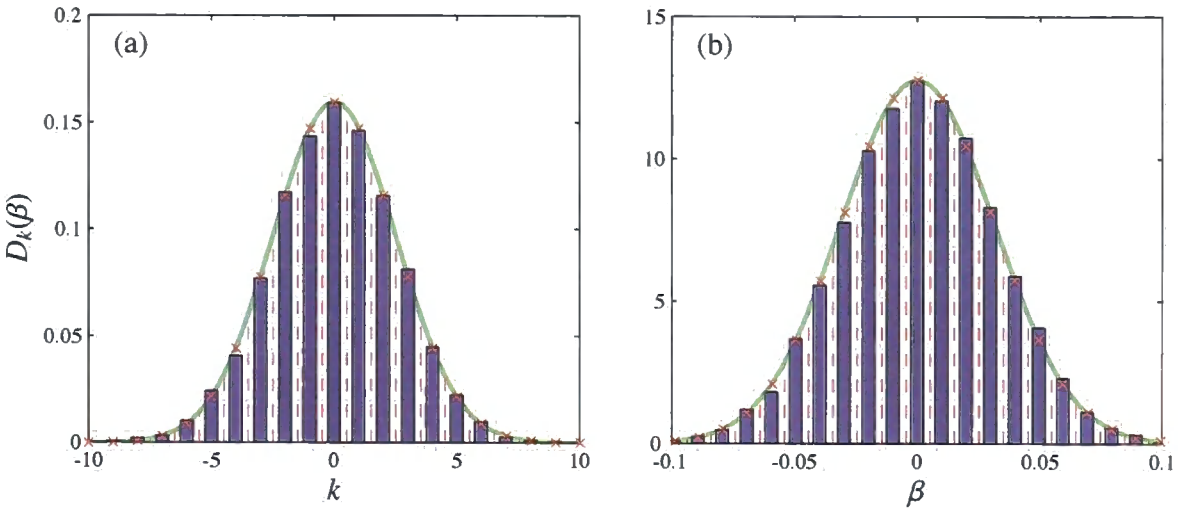

Figure 6.1: The binning process, shown for initial Gaussian distribution $D_k(\beta)$, with standard deviation (a) $w = 2.5$; and (b) $w = 1/32$. Numerical distributions (bars) closely resemble the Gaussian fit (solid curves) defined by Eq. (5.14). The continuous momentum is partitioned into bins, with momentum basis values (crosses) located at the centre of the bin boundaries (dashed lines). Distributions for $\mathcal{N} = 10000$ are normalised, with the resolution in momentum determined by the number of bins over the quasimomentum selected to be (a) $B = 1$, and (b) $B = 101$.

```
discrete_momentum = initial_distribution - beta; % Discrete k basis
basis_index = discrete_momentum + k_limit + 1;   % Discrete basis index
density_operator = zeros(2*k_limit+1,sample);    % Sparse matrix created
for k = 1:sample
    density_operator(basis_index(k),k) = 1;      % Initial density operator
end
```

6.2.3 Quasimomentum resolution

In Section 4.4.2, we expressed the momentum in units of $\hbar K$ with Eq. (4.7) and explained that the quasimomentum is conserved. In Section 5.3, the initial momentum distribution by the dimensionless parameter w, which characterised the width of a Maxwell-Boltzmann distribution of quasimomentum eigenstates. In this section we justify the required resolution of the momentum eigenstates.

In Fig. 6.1, we show the binning process used to analyse the momentum distribution. For each program run, a sample size of $\mathcal{N} = 10000$ eigenstates are evaluated. For a large

temperature, with initial standard deviation $w = 2.5$, the bar chart in Fig. 6.1(a) shows the number of eigenstates in the discrete momentum basis. This closely approximates the analytic Gaussian [green curve]. The values of the discrete momentum basis [red crosses], are placed at the centre of the bin [with edges shown by the dashed lines].

For lower temperatures, the width of the distribution is not resolved using the k basis. We show the initial condition $w = 1/32$ in Fig. 6.1(b), with the quasimomentum subdivided into $B = 101$ bins. We require an odd number of quasimomentum bins to ensure that the central bin contributes the value $k = \beta = 0$ to the momentum basis. This ensures that the odd momentum moments are negligible, and therefore the initial distribution is approximately symmetric. To resolve the quasimomentum, we make use of the code:

```
% Order momentum distribution in ascending beta
    order_beta(1:2*k_limit+1,:) = density_operator;
    order_beta(  2*k_limit+2,:) = beta;
    order_beta                  = sortrows(order_beta',2*k_limit+2)';
    beta                        = sort(beta);
    density_operator            = order_beta(1:2*k_limit+1,:);
```

We have rearranged the momentum distribution into ascending values of β, which enables the binning process in Section 6.3.1.

6.2.4 Evolution operator

The evolution operator is separated by rearranging Eq. (6.1),

$$\tilde{F}_n(\beta) = \underbrace{\exp\left(-i\pi\left[\ell\hat{k}^2 + \Omega\hat{k}\right]\right)}_{\text{discrete\_term}} \underbrace{\exp\left(i2\pi\Omega\hat{k}n\right)}_{(\text{time\_term})^n} \underbrace{\exp\left(-i2\pi\ell\hat{k}\beta\right)}_{\text{quasi\_term}} \underbrace{\sum_{k=-\infty}^{\infty} i^j J_j(\phi_d)\exp\left(ikKz\right)}_{\text{kick}}. \tag{6.3}$$

The evolution operator terms are defined by the following four matrices:

```
% Free evolution operator: Discrete component
    discrete_term = diag(exp(-i*pi*(ell*k_range.*k_range + Omega*k_range)));
    discrete_term = discrete_term*ones(size(density_operator));

% Free evolution operator: Time-dependent component
    time_term = diag(exp(i*2*pi*Omega*k_range));
```

```
    time_term = time_term*ones(size(density_operator));

% Free evolution operator: Quasimomentum component
    quasi_term = diag(beta);
    quasi_term = ones(size(density_operator))*quasi_term;
    quasi_grid = cgrid*ones(size(density_operator));
    quasi_term = exp(-i*2*pi*ell*quasi_term.*quasi_grid);

% Kick matrix
    k_grid = diag(k_range);
    kick   = k_grid*ones(size(k_grid));
    kick   = kick - kick';
    kick   = i.^kick.*besselj(kick,phid);
```

Each term in the evolution operator corresponds to a matrix, which we use in the next section to time evolve the density operator matrix.

6.3 Data generation

6.3.1 Evolution of the momentum distribution

This part of the code simulates the quantum δ-kicked accelerator. For each pulse period, the density operator matrix, defined in Section 6.2.2, is multiplied by the evolution matrices, defined in Section 6.2.4. At each iterative time step, the momentum distribution is calculated and recorded.

This step uses the loop:

```
% The momentum distributions are binned by analysing beta components
bin_limit = -0.5: (1/bin) :0.5; % Bin boundaries established
for kicks = 1:(n_max+1)         % Kicks loop
    for bin_label = 1:bin       % Bin loop
        beta_find = find(beta > bin_limit(bin_label) ...
                         & beta <= bin_limit(bin_label+1));
beta_address(bin_label, :) = bin_label: bin : bin*(2*k_limit+1);
dist_bin(:, bin_label) = sum((abs(density_operator(:, beta_find)).^2), 2);
distribution(beta_address(bin_label, :), kicks) = dist_bin(:, bin_label)';
```

```
    end                          % Bin loop
% Floquet operator iteration: Time evolution of density operator
    density_operator = kick * density_operator;
    free_evolution   = quasi_term.*(time_term.^kicks).*discrete_term;
    density_operator = free_evolution.*density_operator;
end    % Kicks loop
```

6.3.2 Evaluation of the moments and cumulants

The momentum moments, defined by equation (5.7), concisely express the distribution data. They are used to construct the momentum cumulants, as defined by the iterative process explained in Section 5.2.3.

The momentum distribution is normalised and analysed with the commands:

```
distribution = distribution / sample; % Normalise momentum
bin_offset   = 0.5*(1 - 1/bin);       % Place value at centre of correct bin.
p_range = -(k_limit+bin_offset):(1/bin):(k_limit+bin_offset); % Momentum basis

% Momentum moment definition
    moment1 = p_range    * distribution;
    moment2 = p_range.^2 * distribution;
    moment3 = p_range.^3 * distribution;
    moment4 = p_range.^4 * distribution;

% Momentum cumulant definition
    cumulant1 = moment1;
    cumulant2 = moment2 - moment1.^2;
    cumulant3 = moment3 - 3*moment1.*moment2 + moment1.^3;
    cumulant4 = moment4 - 4*moment3.*moment1 + 12*moment2.*moment1.^2 ...
                        - 3*moment2.^2 - 6*moment1.^4;
```

The fact that we employ a Monte-Carlo method means that the odd momentum moments are small, although the values are non-zero. Therefore, in numerical calculations we evaluate the momentum cumulants from their iterative definitions, as given in Section 5.2.3.

6.3.3 Data analysis

For each set of parameters selected, a data file is saved. The file name for the data is generated by the input variable, making them easily accessible. This is done with the commands:

```
% Define file name
w_string          = num2str(w);
Omega_string      = num2str(Omega, 5);
data_output_label = strcat('Omega_',Omega_string,'_w_',w_string,'.mat');

% Output data
save(data_output_label, ...
     'w',  'n',   'Omega',     'ell',       'phid',    ...
     'k_limit',   'k_range',   'bin',       'sample',  'distribution', ...
     'moment1',   'moment2',   'moment3',   'moment4', ...
     'cumulant1', 'cumulant2', 'cumulant3', 'cumulant4')
```

The results are analysed using separate Matlab plotting programs, which are presented in Chapter 10 for the atom-optical δ-kicked rotor [1], which is further generalised in Chapter 11 for the δ-kicked accelerator [3], with the prospect for precision measurement discussed in Chapter 12.

6.4 Numerical accuracy

In this section, we explain how to ensure that the time taken to run the programs is kept reasonable, whilst minimising the numerical errors. As an example, we explain why throughout this thesis, the extent of the discrete momentum basis is set to $k_{\text{limit}} = 250$.

6.4.1 Extent of the discrete momentum basis

The momentum is partitioned into discrete and continuous components according to Eq. (6.2.3). The extent of the discrete momentum is defined by the basis $-k_{\text{limit}} \leq k \leq k_{\text{limit}}$.

In Fig. 6.2, we analyse the evolution of momentum cumulants, varying the extent of the momentum basis, comparing the numerical results with the analytic solutions given

by Eqs. (5.20) and (5.23). We set $\Omega = 0$ and $w = 0$ thus considering the first-order quantum resonance feature in the ultracold limit. The second-order cumulant is plotted in Fig. 6.2(a), with errors analysed in Fig. 6.2(b). The fourth-order cumulant is plotted in Fig. 6.2(c), with errors analysed in Fig. 6.2(d). We define the error in the qth momentum cumulant by

$$E_q(\langle\langle\hat{p}^q\rangle\rangle_n^{1/q}) = \left|\langle\langle\hat{p}^q\rangle\rangle_{\text{numerical}}^{1/q} - \langle\langle\hat{p}^q\rangle\rangle_{\text{analytic}}^{1/q}\right|. \tag{6.4}$$

For low kick numbers, the numerical values are compatible with the analytic result. Following a certain number of kicks, the atoms reach the extent of the momentum basis, introducing errors into the evaluation of the momentum moments. The extent of the momentum basis is varied, with the green curves showing $k_{\text{limit}} = 200$, the blue curves showing $k_{\text{limit}} = 250$, and the red curves showing $k_{\text{limit}} = 300$.

The numerical errors in $E_q(\langle\langle\hat{p}^q\rangle\rangle_n^{1/q})$ are negligible up until the atoms encounter the edge of the momentum basis. For the results presented in this thesis, it is sufficient to choose $k_{\text{limit}} = 250$. For values of Ω for which higher-order quantum resonances occur, the atoms spread out at a lower rate, and therefore the momentum basis is sufficient for all of the parameters considered in this thesis.

6.4.2 Time taken for the programs to run

The script is a self-contained `m`-file, which generates data for a given choice of input parameters. Our computations are run on an eight node cluster, each consisting of two dual core AMD Opteron 280 processors. The nodes control a total of 32 microprocessors which each have 4 GB of random access memory (RAM) and a processing speed of 2.4 GHz.

For the quasimomentum dependence scans in Chapter 9, 11000 eigenstates were considered for each subplot. These programs each took 3 hours to run. In Chapters 10 and 11, each finite temperature evolution considered $\mathcal{N} = 10000$ sample points, again taking around 3 hours to run.

For the results in Chapter 12, we scan over the Ω parameter. For the ultracold limit, we evaluated 30000 Ω values, taking 8 hours to evolve a single eigenstate. When considering the thermal limit, we time evolved $\mathcal{N} = 1000$ sample points for 2000 Ω values, which took 80 hours to run for each value of w considered.

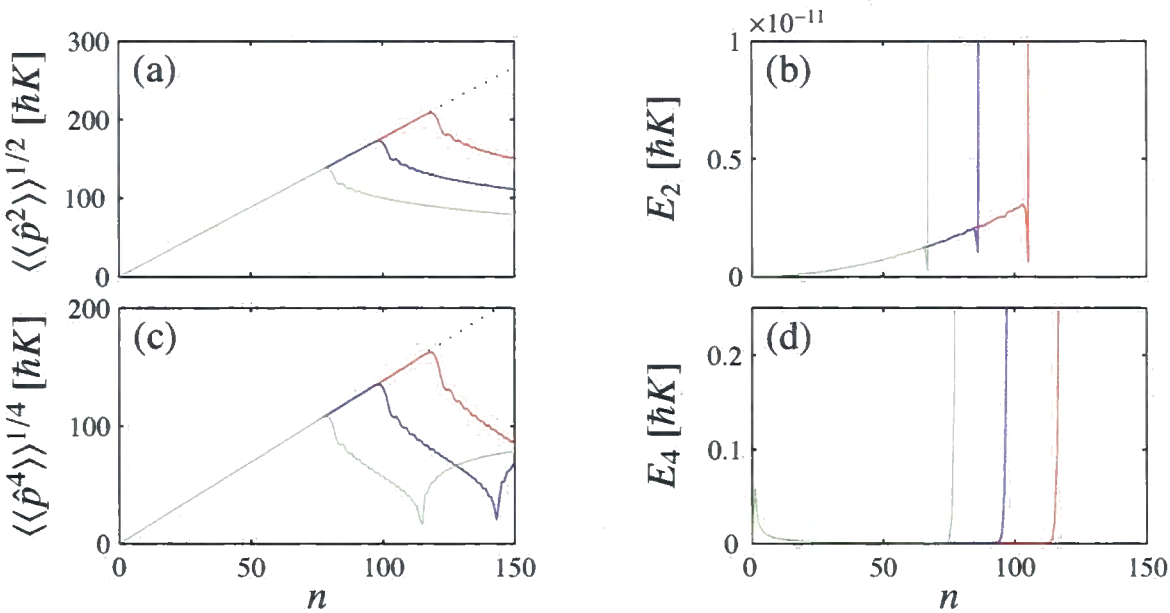

Figure 6.2: Analysis of the numerical errors in the momentum cumulants, $E_q(\langle\langle\hat{p}^q\rangle\rangle_n^{1/q})$, as defined by Eq. (6.4). Analytic results are shown by the dotted lines, corresponding to Eq. (5.20) in (a) and Eq. (5.23) in (c). The coloured lines indicating the extent of the momentum basis, with the green curves showing $k_{\text{limit}} = 200$; the blue curves showing $k_{\text{limit}} = 250$; and the red curves showing $k_{\text{limit}} = 300$. Setting $q = 2$, the cumulants are plotted in (a), and with the errors analysed in (b). Setting $q = 4$, the cumulants are plotted in (c), and with the errors analysed in (d).

6.5 Summary

We have described the program used to generate the numerical data used in this thesis. In the Chapters 7 and 8, we verify that the numerical results are consistent with the analytic predictions from Chapter 5.

In Chapter 9, we extend the analysis beyond the limiting regimes by presenting numerical results over the quasimomentum range. We assess the temperature dependence in Chapters 10 and 11. The Ω dependence is investigated in Chapter 12 first in the ultracold limit, and then for a finite temperature momentum distribution.

Chapter 7

The ultracold regime

7.1 Overview

In this chapter we present the results for an idealised ultracold gas, for which we consider the evolution of the eigenstate $|p = 0\rangle$. This is quantified by the momentum distribution, which is concisely expressed by the momentum moments. We analytically derive these moments for the zero-temperature limit.

In this thesis we present the results in two stages:

1. **The δ-kicked rotor:**
   This is a special case of Hamiltonian (4.3), for which we remove the gravitational effects by setting $a = 0$. As a consequence, the gravity parameter, defined by Eq. (4.13) simplifies to $\Omega = 0$. This enables an extension to atomic physics of the mathematical description of the quantum δ-kicked rotor as introduced in Chapter 3. We investigate the quantum resonant effects as a function of T, as shown in Fig. 4.2.

2. **The δ-kicked accelerator:**
   We consider the dependence of the system upon the gravity parameter Ω, keeping the pulse period constant by setting $T = T_T$ ($\ell = 2$). We compare integer and irrational results, before concentrating on higher-order effects by comparison of rational values of Ω.

7.2 The δ-kicked rotor: Dependence upon the pulse period T

In this section we neglect gravitational effects by setting $\Omega = 0$. We demonstrate that quantum resonance effects occur for particular values of the rescaled Planck's constant k, or equivalently, the pulse periodicity T. As expected, quantum resonance occurs in the $\beta = 0$ subspace for even ℓ while quantum antiresonance is observed for odd values of ℓ.

Figure 7.1 shows the atomic momentum distribution and the second-order momentum moment of a δ-kicked rotor, for the case where the system is initially in the zero-momentum eigenstate with unit amplitude. We have chosen $\phi_d = 0.8\pi$ as an illustrative value typical of recent experiments [16–18, 21, 55–58, 60]. The left-hand subplots show the momentum distribution evolving over $n = 10$ pulses, with the adjacent right hand subplots showing the corresponding second-order momentum moment.

As explained when describing velocity selection in Section 4.5.2, the observation of quantum resonant features depends dramatically upon the initial momentum distribution. In the ultracold limit, we impose the $p = 0$ initial condition by defining the symmetric distribution function $D(p = 0) = \delta(p)$, or equivalently, $D_{k=0}(\beta = 0) = \delta_{k0}\delta(\beta)$. Since $D(p)$ is symmetric, the odd ordered moments are zero, and $\langle \hat{p}^2 \rangle$ is equivalent to $\langle\langle \hat{p}^2 \rangle\rangle$, as seen from Eq. (5.12).

The markers in the right-hand subplots are evaluated from the numerical distributions using Eq. (5.2). The solid lines correspond to analytic solutions, which are derived in Section 5.4.

Quantum antiresonance

Figures 7.1(a) and 7.1(b) are for the case $\ell = 1$. We observe recurrence of the initial state with period $2T$, which from Eq. (3.31) is characteristic of a quantum antiresonance feature. Also note that the parameters for the distribution evolution shown in Fig. 7.1(a) are the same as for the angular momentum results for left-hand column of Fig. 4.2.

Quantum resonance

In contrast, Figs. 7.1(e) and 7.1(f) correspond to the quantum resonant case $\ell = 2$, for which each kick contributes energy to the system, as described by Eq. (3.28). Quadratic growth is observed in the second-order momentum moment, which is referred to as ballistic expansion [50]. The distributions in Fig. 7.1(e) relate to the right-hand column of Fig. 4.2.

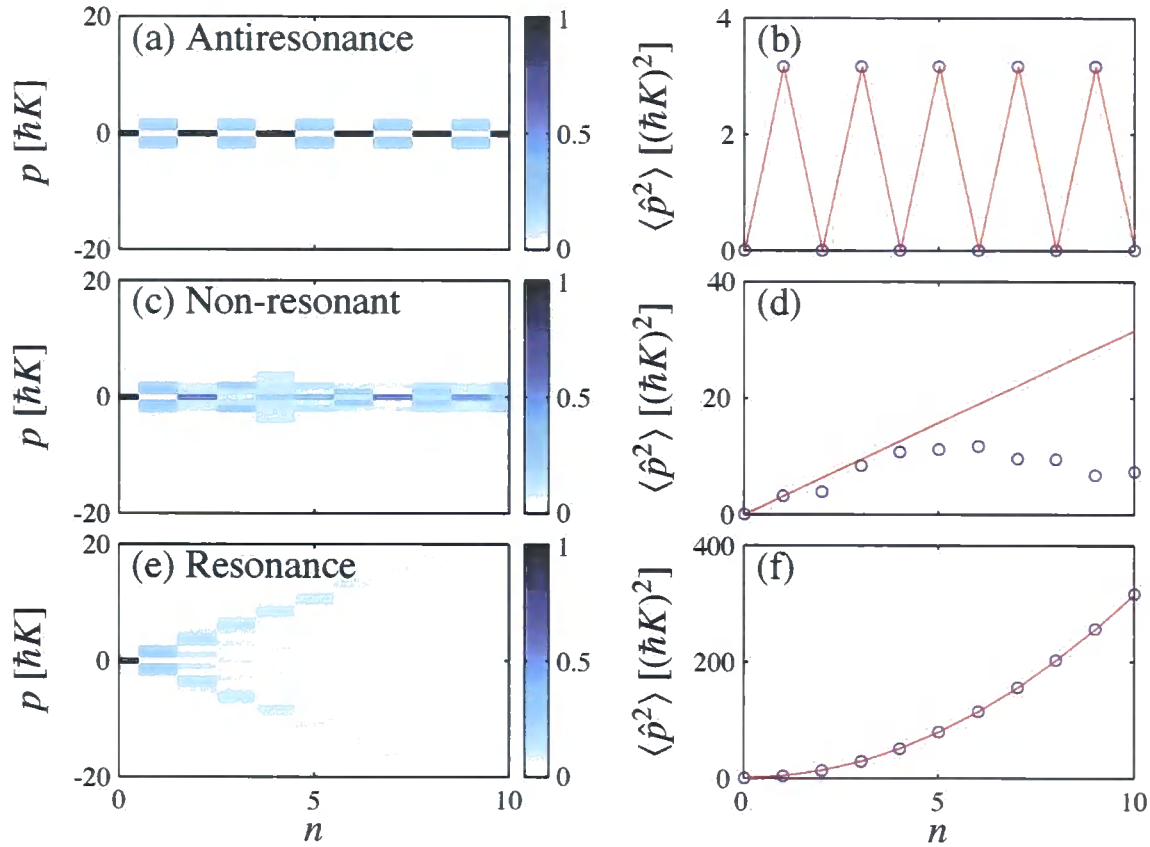

Figure 7.1: Momentum distributions $D(p)$ [left-hand column] and corresponding second-order momentum moments $\langle \hat{p}^2 \rangle$ [right-hand column] for a quantum δ-kicked rotor, as introduced in Chapter 3, described by Hamiltonian (3.1). This is a special case of the δ-kicked accelerator, as introduced in Chapter 4, by setting $\Omega = 0$ in time evolution operator (4.12). In each case the ultracold idealisation is modelled by selecting a zero-momentum eigenstate for the initial condition. Parameters are $\phi_d = 0.8\pi$, $\mathcal{N} = 1$ ($w = 0$), and (a), (b) $T = T_T/2$ [or equivalently $k = 2\pi$, setting $\ell = 1$]; (c), (d) $T = (1 + \sqrt{5})T_T/2$ [or equivalently $k = 2\pi(1 + \sqrt{5})$]; and (e), (f) $T = T_T$ [or equivalently $k = 4\pi$, setting $\ell = 2$]. The markers in (b), (d), and (f) correspond to the numerical results, whilst the solid lines are analytic results from Eqs. (5.22), (5.24) with $w = 0$, and (5.20), respectively.

Comparison with non-resonant parameters

To emphasise the dramatic nature of the quantum resonance effects, we provide a comparison to δ-kicked systems with non-resonant parameters We present the system evolution for the case where T is an irrational multiple of the Talbot time in Figs. 7.1(c) and 7.1(d). We have chosen the value

$$T = (1 + \sqrt{5})T_T/2, \tag{7.1}$$

as the irrational multiple, which is known as the golden ratio, is sufficiently far from a resonant value to ensure that quantum resonant effects do not dominate the dynamics.

The analytic line is a plot of the analytic result for the thermal limit, given by Eq. (5.24). We observe that for the first few kicks, the numerical values of $\langle \hat{p}^2 \rangle$ follow this classical-like analytic diffusion line. After a break time, the system demonstrates its quantum nature. This phenomena is often referred to as dynamical localisation [5, 6, 45, 46, 88], and is analogous to Anderson localisation [85], which has been studied extensively in the field of solid state physics [123, 124].

Realisation of the quantum δ-kicked rotor

Since quasimomentum is conserved, as explained in Section 4.4.2, the accessible momentum spectrum for the dynamics considered in Fig. 7.1 can be mapped to the spectrum of an angular momentum. The results presented in Fig. 7.1 are therefore equivalent to the study in Chapter 3 into the dynamics of a quantum δ-kicked rotor.

7.3 The δ-kicked accelerator: Dependence upon gravity parameter Ω

In this section, we generalise the model to incorporate gravitational effects, as discussed in Chapter 6. The numerical values are compared with the analytic results derived in Section 5.4 for the atom-optical δ-kicked accelerator.

7.3.1 Comparison of integer with irrational values of Ω

In order to study the δ-kicked accelerator in the ultracold regime, we investigate the effects of integer values of Ω, which we compare with an irrational value. We examine the evolution of the $\beta = 0$ subspace for $\ell = 2$ by fixing $T = T_T$. We analyse Fig. 7.2, which is similar to Fig. 7.1, except now, Ω takes the values taken previously by ℓ. To compare the momentum moments, we plot $\langle \hat{p}^q \rangle_n^{1/q}$, for $q = 2$ and $q = 4$. We observe quantum resonant effects similar to those found when varying the pulse period in Fig. 7.1.

The quantum resonant dynamics are highly sensitive to the value of Ω. In Figs. 7.2(a) and (b), quantum antiresonance is observed for $\Omega = 1$. The reconstruction of the initial state every second kick, is well characterized by the second- and fourth-order momentum

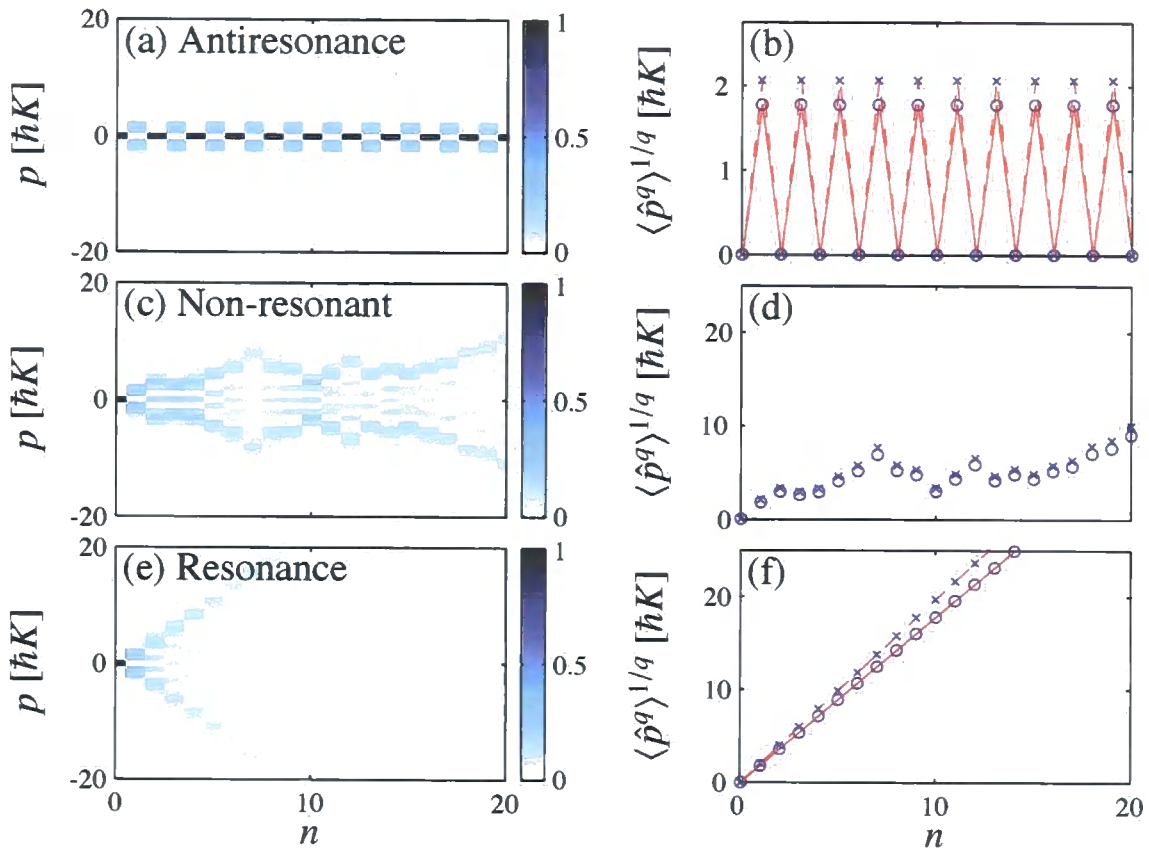

Figure 7.2: Momentum distributions with a resolution of $\hbar K$ [left-hand column], and momentum moments of order ($\circ$) $q = 2$ and ($\times$) $q = 4$ [right-hand column], for a δ-kicked accelerator. The initial condition is a zero-momentum eigenstate and parameters are $\mathcal{N} = 1$, $T = T_T$ ($\ell = 2$), $\phi_d = 0.8\pi$, and (a), (b) $\Omega = 1$; (c), (d) $\Omega = (1 + \sqrt{5})/2$; and (e), (f) $\Omega = 2$. The markers in (b), (d), and (f) denote the momentum moments evaluated directly from the distributions, whilst the solid lines correspond to Eq. (5.20) and the dashed lines correspond to Eq. (5.21).

moments, which oscillate between the $n = 0$ and $n = 1$ values of Eqs. (5.20) and (5.21), respectively.

For $\Omega = 2$ quantum resonance is observed, as shown in Figs. 7.2(e) and (f). The simulation results are consistent with the analytic results given by Eq. (5.20) for $\langle \hat{p}^2 \rangle_n$ and Eq. (5.21) for $\langle \hat{p}^4 \rangle_n$. These results therefore confirm that ballistic expansion results in quadratic growth in the second-order momentum moment and quartic growth in the fourth-order momentum moment.

For an irrational value of Ω, the momentum moments in Fig. 7.2(d) indicate that the second and fourth-order momentum moments behave erratically. Throughout this thesis,

we choose the irrational value to be the golden ratio,

$$\Omega = (1 + \sqrt{5})/2, \tag{7.2}$$

although testing various other irrational values has yielded similar dynamics, as is expected. These quantities show a general trend to increase irregularly, unlike the localisation seen in Fig. 7.1(d), for which the observables stop increasing following a break time.

7.3.2 Rational values of Ω

We further generalise our study of the δ-kicked accelerator in Fig. 7.3 by selecting the effective gravity parameter to be a rational value $\Omega = r/s$, for integers r and s.

A quantum resonance feature is presented satisfying $\Omega = 0$ in Figs. 7.3(a) and (b), which we compare with higher-order quantum resonant effects in Figs. 7.3(c) - (h). For a fractional quantum resonance, the energy transfer to the system is less efficient than the quantum resonant case observed for integer Ω values. The atomic momentum distribution expands in bursts of period $n_T = s$, and the quasi-periodic nature of the energy transfer is directly observable in the evolution of the second- and fourth-order momentum moments.

Comparing Figs. 7.2(c) and 7.3(g) we see a similarity between momentum distributions for which Ω takes irrational and fractional values. However, we see see from the momentum moments that the quasi-periodic behaviour that is observed for fractional values does not occur for non-resonant values of Ω.

Both the analytic and numerical results confirm that to leading order, that for $q = 2$ and $q = 4$, the qth-root of the qth-order momentum moment $\langle \hat{p}^q \rangle_n^{1/q}$ grows linearly in n at a rate proportional to $1/\sqrt{s}$. We observe that, when n is not an integer multiple of s, the momentum moments oscillate periodically around the analytic predictions (5.20) and (5.21).

7.4 Summary

The results of this thesis are conveyed by presenting quantum resonant effects for different values of the system parameters, including T, Ω and temperature. In this chapter, we considered the dynamics of the δ-kicked accelerator restricted to the zero temperature idealised case, for which we restrict $\beta = 0$.

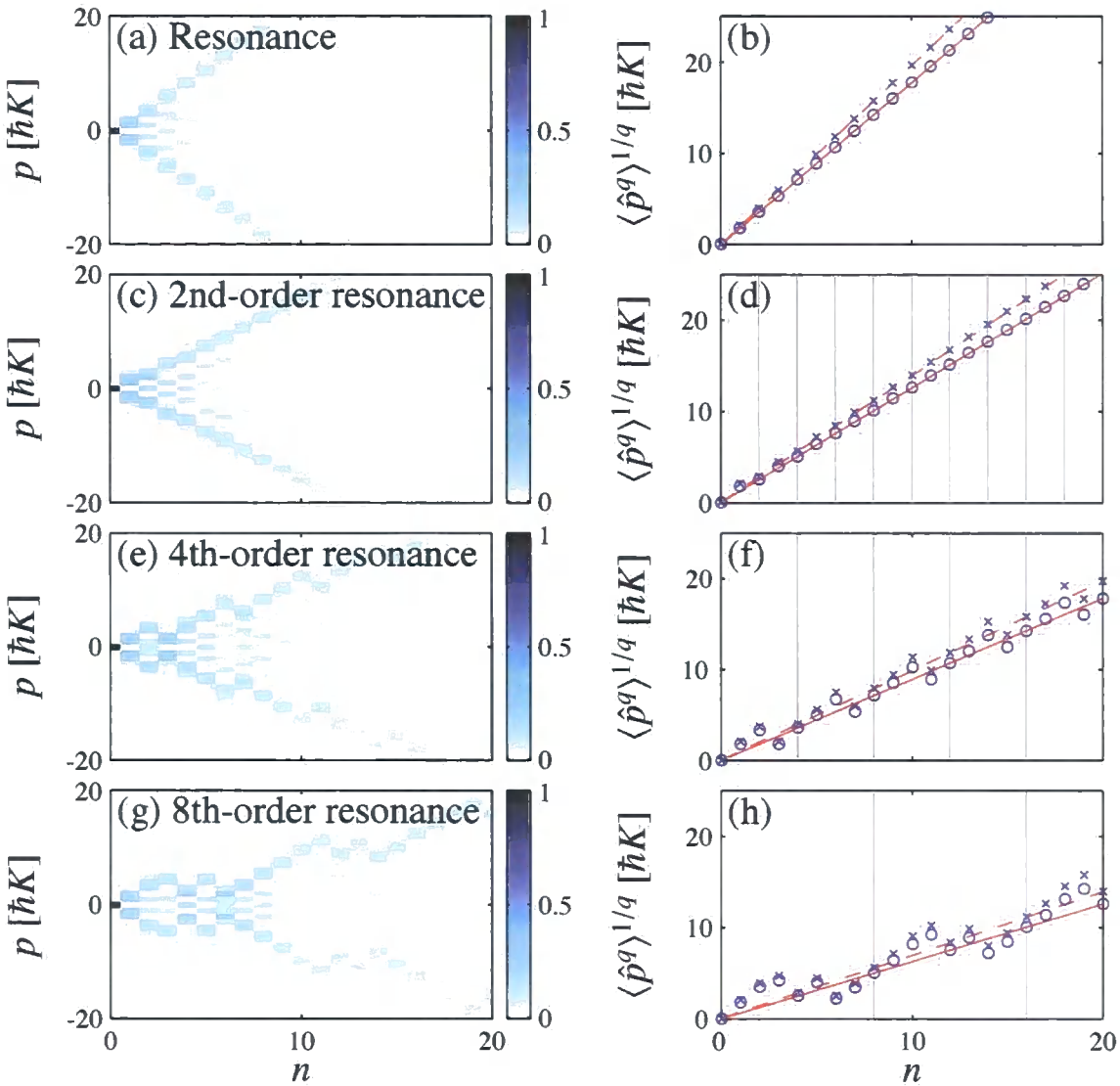

Figure 7.3: Momentum distributions $D(p)$ with a resolution of $\hbar K$ [left-hand column], and momentum moments of order ($\circ$) $q = 2$ and ($\times$) $q = 4$ [right-hand column], for a δ-kicked accelerator. The initial condition is a zero-momentum eigenstate and parameters are $\mathcal{N} = 1$, $T = T_T$ ($\ell = 2$), $\phi_d = 0.8\pi$, and (a), (b) $\Omega = 0$; (c), (d) $\Omega = 1/2$; (e), (f) $\Omega = 1/4$; and (g), (h) $\Omega = 1/8$. The markers in (b), (d), (f), and (h) denote the momentum moments evaluated directly from the distributions, whilst the solid lines correspond to Eq. (5.20) and the dashed lines correspond to Eq. (5.21). The vertical lines in (d), (f), and (h), indicate where n is an integer multiple of s (as taken from $\Omega = 1/s$).

We compared the time evolution of the momentum distribution for different values of T, and then observed fractional quantum resonances for $\Omega = 1/s$ and $T = T_T$ ($\ell = 2$). We found that the quantum resonant dynamics are highly sensitive to the value of Ω.

As explained in Chapter 5, we are interested in observables for which Ω is resolvable, allowing the fractional quantum resonant features to be distinguished. In Chapter 12, we assess the prospect of distinguishing between Ω values, with a view to potentially using this technique for precision measurement of local gravitational acceleration.

We see from Eq. (5.20) that the fractional quantum resonances are characterized by quadratic growth of the second-order momentum moment at a rate inversely proportional to s: $\langle\hat{p}^2\rangle_n \propto n^2/s$. The leading order fourth-order momentum moment characterises quantum resonance as described by Eq. (5.21): we find that the evolution dependence is given by $\langle\hat{p}^4\rangle_n \propto n^4/s^2$. These details are summarised in Table 7.1.

Order	Quantity	Observable	Low temperature	Ω resolvable	Equation
1	Mean	$\langle\hat{p}\rangle_n$	≈ 0		
2	Variance	$\langle\hat{p}^2\rangle_n$	$\propto n^2/s$	Yes	(5.20)
3	Skewness	$\langle\hat{p}^3\rangle_n$	≈ 0		
4	Kurtosis	$\langle\hat{p}^4\rangle_n$	$\propto n^4/s^2$	Yes	(5.21)

Table 7.1: The momentum moments for the quantum resonance features in the low temperature limit. The dependence of the observables upon the time and gravity parameter is summarised. Resolving $\Omega = r/s$ is possible from both the energy of the ensemble, and the shape of the momentum distribution.

We are interested in simulating this system for a finite temperature gas. In the next chapter, we make use of the simulation from Chapter 6, for a large value of w, and demonstrate that the dynamics approximates the limiting regime for a thermal gas.

Chapter 8

The thermal regime

8.1 Overview

The time evolution operator governing the dynamics in each quasimomentum subspace is explicitly dependent upon β, as seen from Eq. (4.12). In the case of a finite temperature cloud, we may consider all of the quasimomentum subspaces to be populated. Therefore, the overall dynamics exhibit some significant qualitative differences when compared with the three cases considered in Chapter 7, for which the treatment was restricted to the $\beta = 0$ subspace.

In this chapter, we investigate the dynamics in the thermal limit, by running the simulation presented in Chapter 6 for finite temperature gas which has a large value of w. We again model a finite temperature cloud by imposing the initial momentum distribution composed from quasimomentum eigenstates described by the Gaussian (5.14). A Maxwell-Boltzmann temperature of around 5 μK for the case of caesium [57, 60] corresponds to setting $w = 2.5$, as investigated experimentally in Oxford [107].

We again present the results for the following two cases:

1. **The quantum δ-kicked rotor:**
   Quantum resonance and quantum antiresonance effects are demonstrated by selecting particular values of the pulse period T.

2. **The quantum δ-kicked accelerator:**
   Higher-order quantum resonant effects are examined by the comparison of rational values of Ω with integer and irrational values.

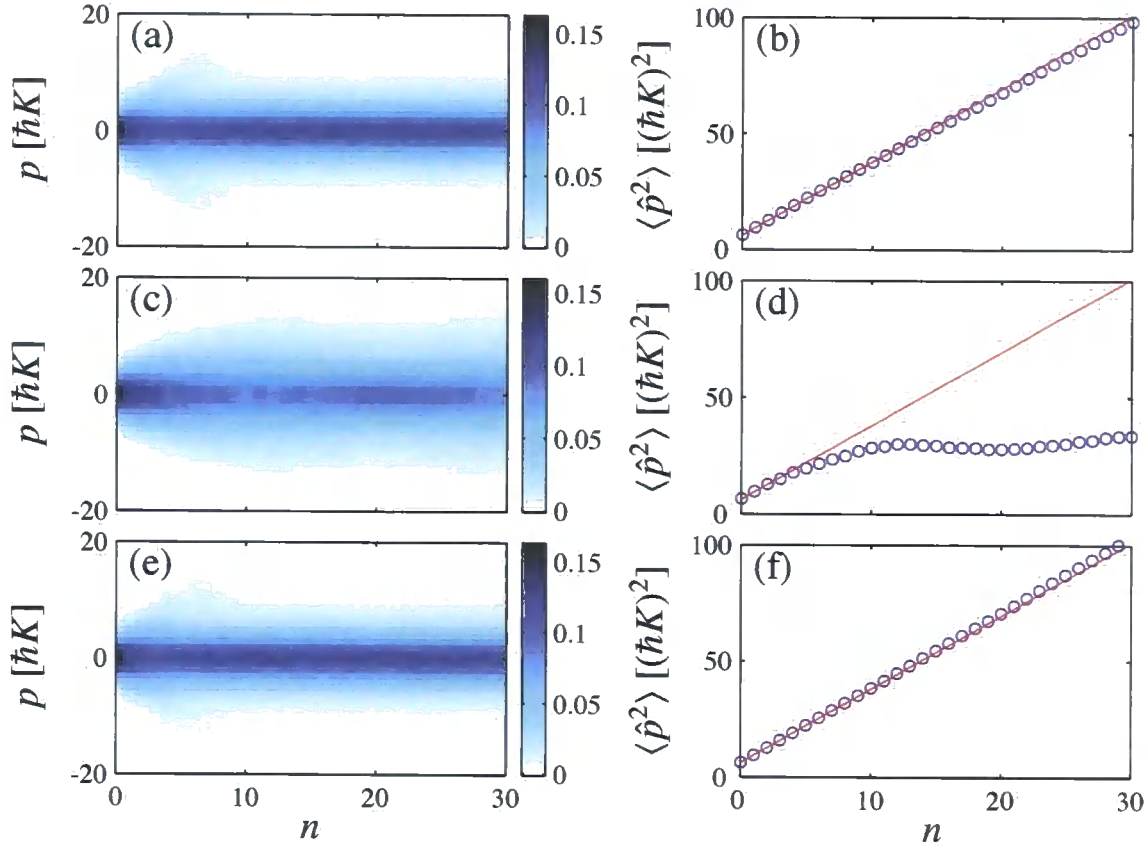

Figure 8.1: Momentum distributions $D(p)$ [left-hand column] and corresponding second-order momentum moments $\langle \hat{p}^2 \rangle$ [right-hand column] of a δ-kicked rotor, as introduced in Chapter 3, described by Hamiltonian (3.1). This is a special case of the δ-kicked accelerator, as introduced in Chapter 4, by setting $\Omega = 0$ in time evolution operator (4.12). In each case the initial thermal regime is modelled by populating Gaussian momentum distribution (5.14) via a Monte Carlo method. An initial standard $w = 2.5$ deviation corresponds to an experimental temperature of 5 μK. Parameters are $\phi_d = 0.8\pi$, $\mathcal{N} = 10000$, and (a), (b) $T = T_T/2$ ($\ell = 1$); (c), (d) $T = (1 + \sqrt{5})T_T/2$; and (e), (f) $T = T_T$ ($\ell = 2$). The solid lines in (b), (d), and (f) correspond to the linear result (5.24).

8.2 The δ-kicked rotor: Dependence upon the pulse period T

Following the procedure from Chapter 7, we again set $\Omega = 0$ and assess the dependence upon time period T, this time for a thermal cloud of atoms. We compare numerical simulation with the analytic predictions.

In Fig. 8.1, we show the atomic momentum distribution and the second-order momen-

tum moment of a δ-kicked cloud of non-interacting particles with initial width parametrised by $w = 2.5$. The values of ℓ is the same as presented in Fig. 7.1, for the case of a zero-momentum eigenstate. The finite temperature cloud appears to behave identically for $\ell = 1$ and $\ell = 2$, as seen by comparing Figs. 8.1(a) and (b) with Figs. 8.1(e) and (f). In practice W. H. Oskay *et al.* [50] have shown that at finite temperature, quatum resonance can be distinguished from quantum antiresonance because the trajectories of the ballistically expanding atoms are subtly different. We consider the duration of the pulses to satisfy the Raman-Nath regime, and therefore take the limit $t_p \to 0$, and consequently do not observe such differences.

For $\ell = 1$ or 2, a small fraction of the cloud expands ballistically, but much of the distribution remains near zero momentum. This clustering near the centre is due to quantum antiresonant effects occuring concurrently with the ballistic expansion arising from the quantum resonant dynamics. In Figs. 8.1(c) and (d), we set T to be an irrational multiple of the Talbot time, as given by Eq. (7.1). We observe dynamical localization rather than ballistic expansion. The distribution in Fig. 8.1(c), while truncated at the edges, appears flatter and broader compared to Figs. 8.1(a) and (e).

In Figs.8.1(b) and (f), we show that the second-order momentum moment grows linearly. This is dramatically different from either the periodic behaviour or the quadratic growth observed in Figs. 7.1(b) and (f), respectively. Linear energy growth is characteristic of quantum resonant phenomena in a thermal atomic cloud [50]. The numerical results are in agreement with the analytic line given by Eq. (5.24), which is valid for integer and half-integer Ω values, and also coincides with the classical result in a regime of global chaos [46, 73]. Close inspection of Figs. 8.1(b) and (f) reveals that the classical expression slightly overestimates the numerical data in the quantum antiresonant case, and underestimates in the quantum resonant case.

8.3 The δ-kicked accelerator: Dependence upon gravity parameter Ω

In this section we compare the simulation results to the analytic derivation for a thermal gas subject to the δ-kicked accelerator time-evolution. We follow the procedure from Section 7.3, for which we considered the zero temperature idealisation by restricting the initial condition to the $\beta = 0$ subspace. As explained in Section 8.2 for the case of $\Omega = 0$, a finite temperature gas exhibits significant differences in comparison to the zero

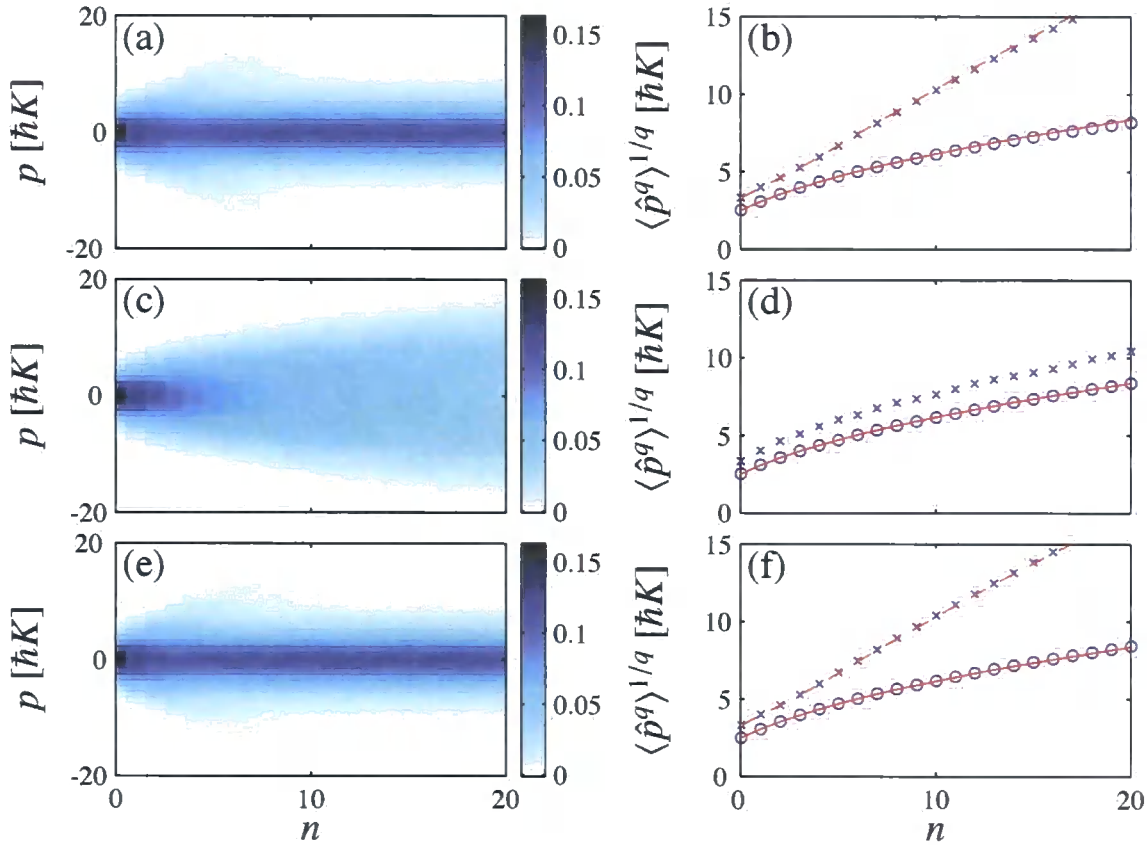

Figure 8.2: Momentum distributions $D(p)$ [left-hand column] and the corresponding qth root of the qth-order momentum moment $\langle \hat{p}^q \rangle^{1/q}$ [right-hand column], with $q = 2$ ($\circ$); and $q = 4$ ($\times$). The evolution is governed by Hamiltonian (4.3), which realises the δ-kicked accelerator for the thermal limit of the atom-optical configuration. In each case the initial atomic momentum distribution given by Eq. (5.14) is evolved by transformed evolution operator (4.12). Parameters are $T = T_T$ ($\ell = 2$), $w = 2.5$, $\phi_d = 0.8\pi$, $\mathcal{N} = 10000$, and (a), (b) $\Omega = 1$; (c),(d) $\Omega = (1+\sqrt{5})/2$; (e), (f) $\Omega = 2$. The markers in (b), (d), and (f) denote the momentum moments, evaluated directly from the distributions. The solid lines correspond to Eq. (5.24). The dashed lines in (b) and (f) correspond to Eq. (5.25).

momentum case.

We present results for integer values of Ω, which we compare to an irrational value, and then investigate higher-order effects by selecting Ω to be rational.

8.3.1 Comparison of integer with irrational values of Ω

In Fig. 8.2, we show, the momentum distributions and second- and fourth-order momentum moments as a function of kick number. The parameters are the same as those used

in Fig. 7.2, with the exception that in Fig. 8.2, the initial condition in each case is a Gaussian momentum distribution with $w = 2.5$.

There are distinct differences in this case compared to the zero momentum eigenstate evolutions shown in Fig. 7.2. For integer values of Ω, pure quantum resonant behaviour occurs for the zero momentum eigenstate, as seen in Figs. 7.2(a) and (e). In contrast, at finite temperature the momentum distribution behaves identically irrespective of whether Ω is even or odd, as seen from Figs. 8.2(a) and (e). As shown for the δ-kicked rotor in Fig. 8.1, we observe that a small fraction of the cloud expands ballistically, but much of the distribution remains clustered near zero momentum.

8.3.2 Rational values of Ω

For $\Omega = 1/s$, we again observe a small fraction of the cloud expanding ballistically at finite temperature, as shown in Figs. 8.3(a), (c), (e), and (g). However, as s increases, the rate of ballistic expansion in the wings of the distribution is reduced. This is characteristic of fractional quantum resonances and was more clearly observable in the zero-mometum eigenstate evolutions shown in Fig. 7.3. Also, with increasing s, the fraction of the cloud clustered near zero momentum becomes increasingly delocalized, as can be seen in Fig. 8.3 after 20 kicks. This indicates that, for rational values of Ω, the higher-order quantum antiresonances are not as effective at localizing the atom cloud.

The evolutions of the second-order momentum moment are extremely similar for each value of Ω illustrated in Figs. 8.2 and 8.3. We have found this to be a general property at finite temperature, which reflects the fact that quantum resonant and quantum antiresonant dynamics are occurring concurrently in the cloud. This rules out the second-order momentum moment as a useful means of concisely distinguishing different fractional quantum resonances from one another, or indeed from the non-resonant case shown in Figs. 8.2(c) and (d).

In contrast, the fourth-order momentum moment evolutions remain comparatively distinct, as shown in the right-hand panel of Figs. 8.2 and 8.3. We find that for larger values of s, the fourth-order momentum moment increases at a slower rate. This is a quantitative signature of the fact that as s increases both the higher-order quantum resonant dynamics are less efficient at transferring energy to the atoms. Consequently the momentum distributions become less peaked. The fourth-order momentum moment evolution is sensitive to the peakedness of the distribution, and provides a useful way to characterize the manifestation of fractional quantum resonant effects at finite temperature.

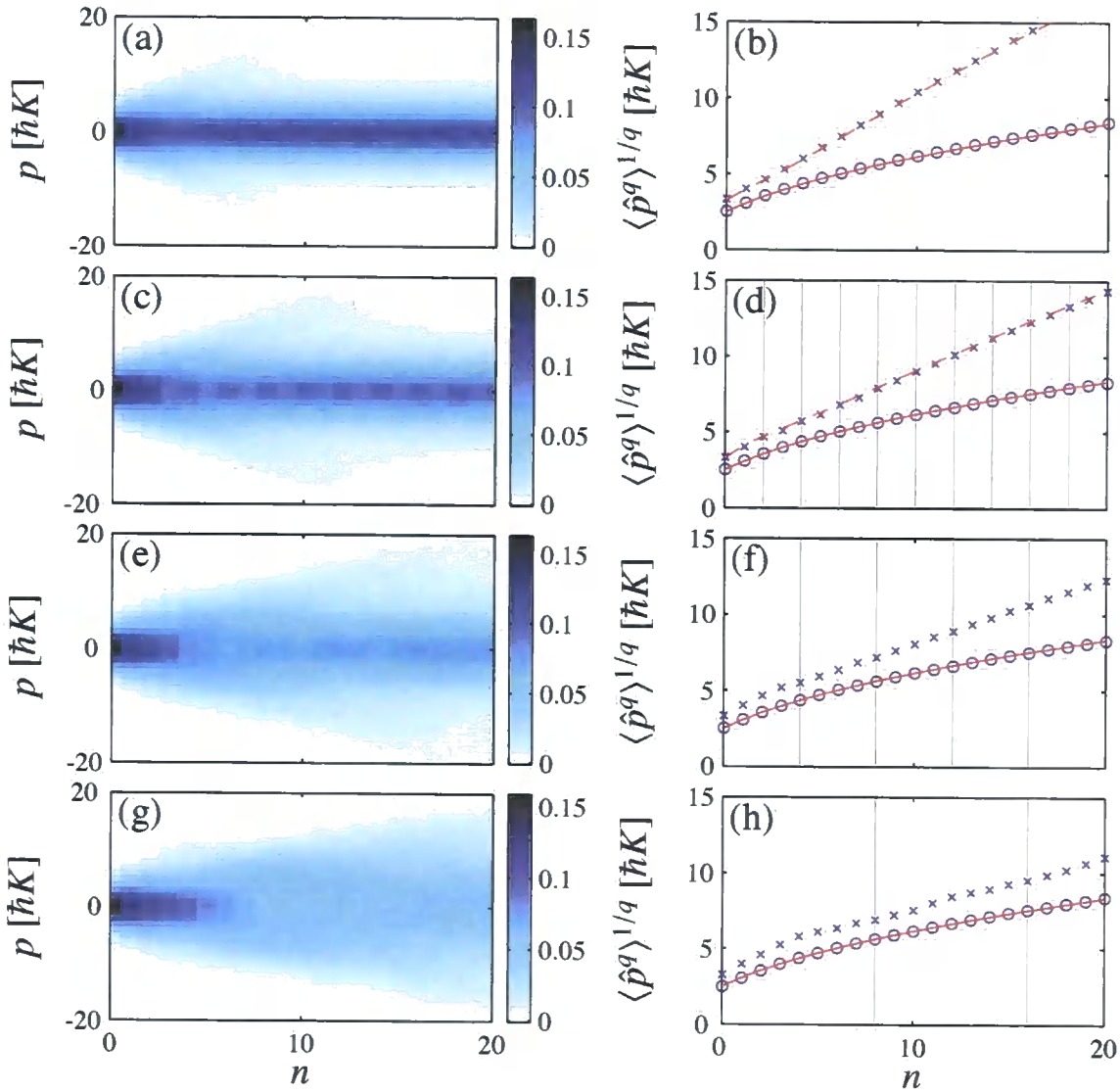

Figure 8.3: Momentum distributions $D(p)$ [left-hand column] and the corresponding qth root of the qth-order momentum moment $\langle \hat{p}^q \rangle^{1/q}$ [right-hand column], with $q = 2$ ($\circ$); and $q = 4$ ($\times$). The evolution is governed by Hamiltonian (4.3), which realises the δ-kicked accelerator for the thermal limit of the atom-optical configuration. In each case the initial atomic momentum distribution given by Eq. (5.14) is evolved by transformed evolution operator (4.12). Parameters are $T = T_T$ ($\ell = 2$), $w = 2.5$, $\phi_d = 0.8\pi$, $\mathcal{N} = 10000$, and (a), (b) $\Omega = 0$; (c),(d) $\Omega = 1/2$; (e), (f) $\Omega = 1/4$; (g), (h) $\Omega = 1/8$. The markers in (b), (d), (f), and (h) denote the momentum moments, evaluated directly from the distributions. The solid lines correspond to Eq. (5.24). The dashed lines corresponds to Eq. (5.25) in (b); and Eq. (5.26) in (d). The vertical lines in (d), (f), and (h), indicate where n is an integer multiple of s (as taken from $\Omega = 1/s$).

However, we note that for integer Ω, the fourth-order momentum moment evolutions are

essentially indistinguishable, as seen from Figs. 8.2(b), 8.2(f), and 8.3(b).

8.4 Summary

In this chapter, we have demonstrated that a broad initial momentum distribution approaches the thermal limit, characterised by the second-order momentum moment growing linearly with n, at a rate that appears to be independent of Ω: from Eq. (5.24) we note the trend that on average, $\langle \hat{p}^2 \rangle_n \propto n$. The fourth-order momentum moment appears to evolve, to leading order, cubically as $\langle \hat{p}^4 \rangle_n \propto n^3/s$: we emphasize that while we have only shown these trends to be exactly true for $s = 1$ in Eq. (5.25), and $s = 2$ in Eq. (5.26), the generalization to higher values of s is strongly supported by our numerical calculations. These details are summarised in Table 8.1.

Order	Quantity	Observable	High temperature	Ω resolvable	Equation
1	Mean	$\langle \hat{p} \rangle_n$	≈ 0		
2	Variance	$\langle \hat{p}^2 \rangle_n$	$\propto n$	No	(5.24)
3	Skewness	$\langle \hat{p}^3 \rangle_n$	≈ 0		
4	Kurtosis	$\langle \hat{p}^4 \rangle_n$	$\propto n^3/s$	Yes	(5.25) & (5.26)

Table 8.1: The momentum moments in the high temperature limit. The dependence of the observables upon the time and gravity parameter is summarised. Resolving $\Omega = r/s$ is not possible from the energy of the ensemble, but is possible from the shape of the momentum distribution.

In the next chapter we examine the underlying mechanisms that give rise to the ultracold and thermal regimes by dissecting the initial atom cloud into its constituent momentum eigenstates.

Chapter 9

Quasimomentum dependence

9.1 Overview

In this chapter, we investigate in detail the quasimomentum dependence for various values of the system parameters. We follow the procedure from Chapters 7 and 8, examining values of the pulse period, before focussing on the gravity parameter, and investigating the fractional quantum resonance effects in detail.

The differences observed between the zero-temperature limit, as summarised in Table 7.1, and the thermal limit, as summarised in Table 8.1, arise because different quasimomentum eigenstates evolve according to the β-dependent transformed Floquet operator (4.12). For a broad initial momentum distribution, all quasimomentum eigenstates are populated and the observed momentum moment dynamics is determined by averaging over all the different eigenstate evolutions. It is therefore instructive to consider the dynamics of the different β eigenstates independently.

9.2 The δ-kicked rotor: Dependence upon the pulse period T

We introduced the Talbot effect in Chapter 3, and analytically examined the evolution operator as a function of the pulse period. A pulse period of a half-integer multiple of the Talbot time, as imposed by Eq. (3.33), results in the observation of quantum resonance for even values of ℓ and quantum antiresonance for odd values of ℓ. In Chapter 7 we considered the $\beta = 0$ subspace, and found that quantum resonance and quantum antiresonance are

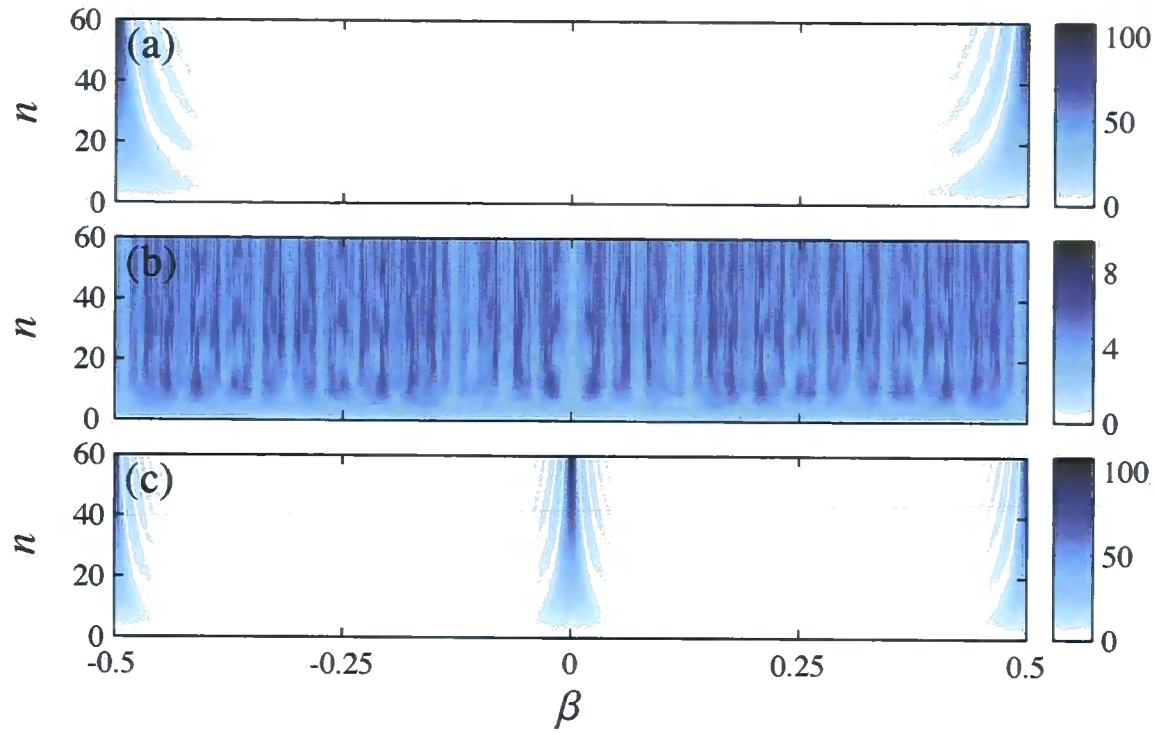

Figure 9.1: The evolution of the δ-kicked particle, initially in the plane-wave state $|\beta\rangle$, subject to subsequent applications of Floquet operator (4.12). The colour scale quantifies $\langle\langle\hat{p}^2\rangle\rangle_n^{1/2}$, in units of $\hbar K$, which is proportional to the kinetic energy of the particle. Pulse period (a) $T = T_T/2$ ($\ell = 1$); (b) $T = (1+\sqrt{5})T_T/2$; and (c) $T = T_T$ ($\ell = 2$). Parameters are $\Omega = 0$, $\phi_d = 0.8\pi$, and $\mathcal{N} = 1$ ($w = 0$). The quantum resonant features are summarised in Table 9.1, and analysed in detail for (a) in Fig. 9.2; and (c) in Fig. 9.3.

Pulse period	$\beta = 0$	$\beta = \pm 1/4$	$\beta = \pm 1/2$
$T = T_T/2$ ($\ell = 1$)	Antiresonance	Higher-order	Resonance
$T = (1+\sqrt{5})T_T/2$	Non-resonant	Non-resonant	Non-resonant
$T = T_T$ ($\ell = 2$)	Resonance	Antiresonance	Resonance

Table 9.1: The quantum resonant features for the δ-kicked rotor, for which $\Omega = 0$. Results are summarised for the pulse period values presented in Fig. 9.1.

clearly distinct, as seen from Fig. 7.1. In contrast, we showed in Chapter 8 that at finite temperature, the system appears to behave identically irrespective of whether ℓ is even or odd, as seen from Fig. 8.1.

9.2.1 Quantum resonant features

In this section we look at the effect of the quasimomentum β on quantum resonant dynamics for the δ-kicked rotor. We illustrates this β dependence in Fig. 9.1, with the quantum resonant features summarised in Table 9.1. In Fig. 9.1(a), for $\ell = 1$, quantum antiresonance occurs at $\beta = 0$, as was observed in Figs. 7.1(a) and (b). Quantum resonances occur at $\beta = \pm 1/2$. In Fig. 9.1(c), for $\ell = 2$, a quantum resonance occurs at $\beta = 0$, as observed in Figs. 7.1(e) and (f), and also at $\beta = \pm 1/2$. Quantum antiresonances are observed at $\beta = \pm 1/4$.

For comparison, in Fig. 9.1(b) we show the quasimomentum dependence for a pulse period of an irrational multiple of the Talbot time, as given by Eq. (7.1). We find that the quantum resonant structure breaks down, such that it is no longer possible to distinguish the value of β by examining the evolution of the observable $\langle\langle \hat{p}^2 \rangle\rangle_n^{1/2}$.

9.2.2 Quantum resonant conditions

In Appendix D, we explain that the probability amplitude, from which we extract the momentum moments, is given by Eq. (D.3),

$$|c_{kj}(\beta, nT)|^2 = J_{j-k}^2(\omega). \tag{9.1}$$

For the δ-kicked rotor, ω is given by Eq. (D.17) [47],

$$\omega = \phi_d \frac{\sin(n\Upsilon)}{\sin(\Upsilon)}, \tag{9.2}$$

with the quasimomentum and pulse period incorporated into the parameter (D.8) with the definition

$$\Upsilon = \frac{1}{2}\pi(1 + 2\beta)\ell. \tag{9.3}$$

Quantum resonance

Quantum resonance occurs when setting $\Upsilon = m\pi$, where m is an integer, for which a resonant value of the quasimomentum is given by

$$\beta_m^R = \frac{m}{\ell} - \frac{1}{2}. \tag{9.4}$$

Since $\sin(n\Upsilon) = 0$, we obtain $\omega = n\phi_d$ using l'Hôpital's rule. Therefore, the probability amplitudes are determined to be

$$|c_{kj}(\beta, nT)|^2 = [J_{j-k}(n\phi_d)]^2. \tag{9.5}$$

This is consistent with our observation that under resonant conditions, the application of n kicks is equivalent to the application of one kick with amplitude $n\phi_d$.

Quantum antiresonance

Quantum antiresonance occurs when setting $\Upsilon = (m + 1/2)\pi$, where m is an integer, for which an antiresonant value of the quasimomentum is given by

$$\beta_m^A = \frac{m}{\ell} + \frac{1}{2\ell} - \frac{1}{2}. \tag{9.6}$$

The Bessel function argument is given by $\omega = \phi_d \sin(n\pi/2)$, and therefore the probability that the initial state is measured to have momentum $\hbar K(j + \beta)$ is

$$|c_{kj}(\beta, nT)|^2 = [J_{j-k}(\phi_d \sin(n\pi/2))]^2. \tag{9.7}$$

This is consistent with our observation that under the conditions of a quantum antiresonance, the momentum distribution oscillates with every two kicks.

Spacing of the features

The spacing between quantum resonances is found to be

$$\beta_{m+1}^R - \beta_m^R = \frac{1}{\ell}. \tag{9.8}$$

Quantum antiresonances have separation

$$\beta_{m+1}^A - \beta_m^A = \frac{1}{\ell}, \tag{9.9}$$

as expected, since they occur half way between the quantum resonances. These analytic result are in agreement with the numerical observations from Figs. 9.1(a) and 9.1(c).

9.2.3 The width of the quantum resonant features

The quantum resonant features in Fig. 9.1 have a momentum width associated with them, which depends on ℓ and the kick number n, which we explore further in this section. We zoom in on these features for $\ell = 1$ in Fig. 9.2 and $\ell = 2$ in Fig. 9.3.

In close proximity to the main quantum resonance and quantum antiresonance features, the red lines correspond to hyperbolic curves of zero momentum variance. We call these reconstruction loci, as they each correspond to a discontinuous series of points in time where high-order quantum antiresonances cause the initial condition to be periodically reconstructed. In this section, we summarise the procedure developed by K. J. Challis to quantify the width of the quantum resonance features. We verify that the numerical and analytic results are consistent.

High-order quantum antiresonance

As explained in Section 4.5.2, an understanding of the evolution of the momentum eigenstates in the vicinity of a quantum resonant feature provides an application to precision measurement of atom velocity. The reconstruction loci are defined in terms of the high-order quantum antiresonance, which we use to quantify the width of the quantum resonant features.

An Nth order quantum antiresonance occurs when the system returns to its initial state every Nth kick. From Eq. (9.2) this corresponds to

$$\Upsilon = \frac{1}{2}\pi(1+2\beta)\ell = \pi\frac{m}{N}, \tag{9.10}$$

where m is a nonzero integer, and m and N have no common factors. In this case,

$$|c_{kj}(\beta, nT)|^2 = \left[J_{j-k}\left(\phi_d \frac{\sin(nm\pi/N)}{\sin(m\pi/N)}\right)\right]^2. \tag{9.11}$$

When n is a multiple of the order N, $|c_{kj}(\beta, nT)|^2 = \delta_{jk}$, and the system returns to its initial state[1].

[1]Note that when $N = 2$, we regain the results of Eq. (9.7)

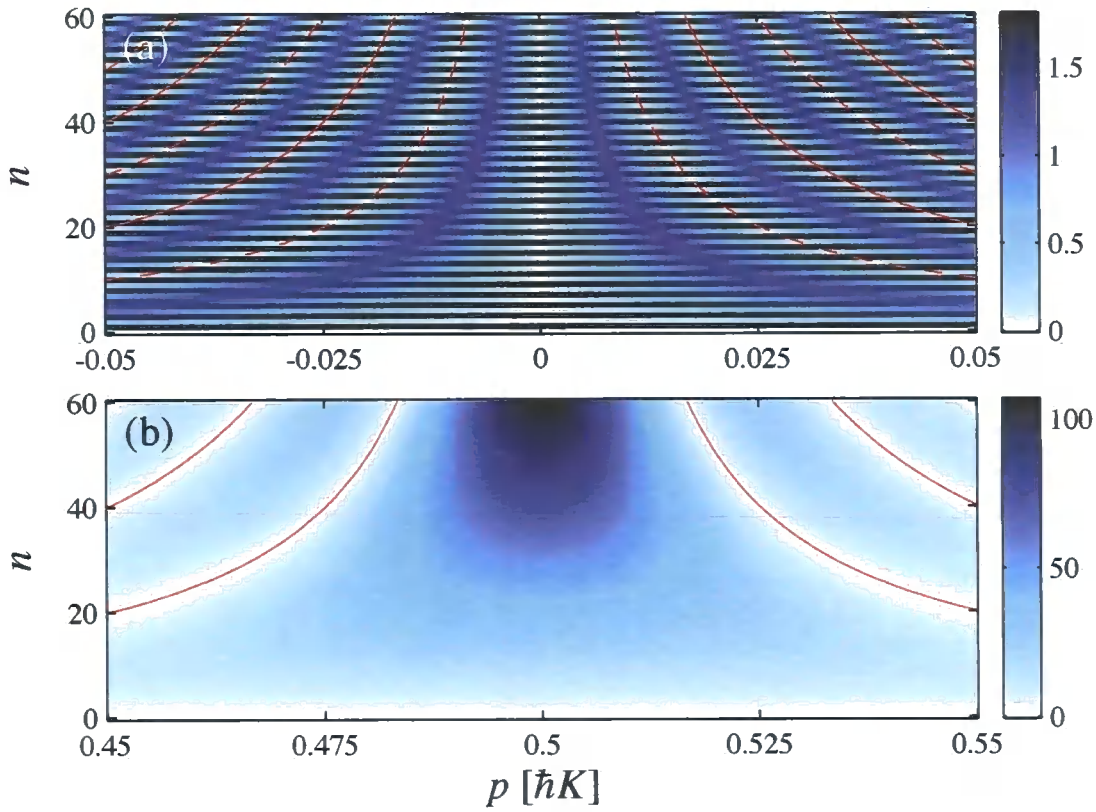

Figure 9.2: The evolution of the δ-kicked particle, initially in the plane-wave state $|\beta\rangle$, subject to subsequent applications of Floquet operator (4.12). The colour scale quantifies $\langle\langle\hat{p}^2\rangle\rangle_n^{1/2}$, in units of $\hbar K$, which is proportional to the kinetic energy of the particle. Parameters are $T = T_T/2$ ($\ell = 1$), $\Omega = 0$, $\phi_d = 0.8\pi$, and $\mathcal{N} = 1$ ($w = 0$). We show the features from Fig. 9.1(a) in detail: the quantum antiresonance in the vicinity of $\beta = 0$ (a), with the analytic asymptotes corresponding to Eq. (9.14); and the quantum resonance in the vicinity of $\beta = 0.5$ (b), with the analytic asymptotes corresponding to Eq. (9.12).

Quantum resonance width

In close proximity to a quantum resonance, we evaluate the difference $\bar{\beta} = \beta - \beta_m^{\mathrm{R}}$ for which β satisfies the Nth-order quantum antiresonance condition (9.10). It was shown analytically by K. J. Challis that the solid red lines in Figs. 9.2(b) and 9.3(a), correspond to reconstruction loci [1]

$$\bar{\beta}^R = \mu/N\ell, \tag{9.12}$$

where μ is an integer. The hyperbolic curves lying halfway between the quantum resonance at β_m^{R} and the reconstruction loci $\bar{\beta}^R = \pm 1/N\ell$ we call transition loci, as they are the sequence of points at which the wave-function begins the process of reconstruction. The

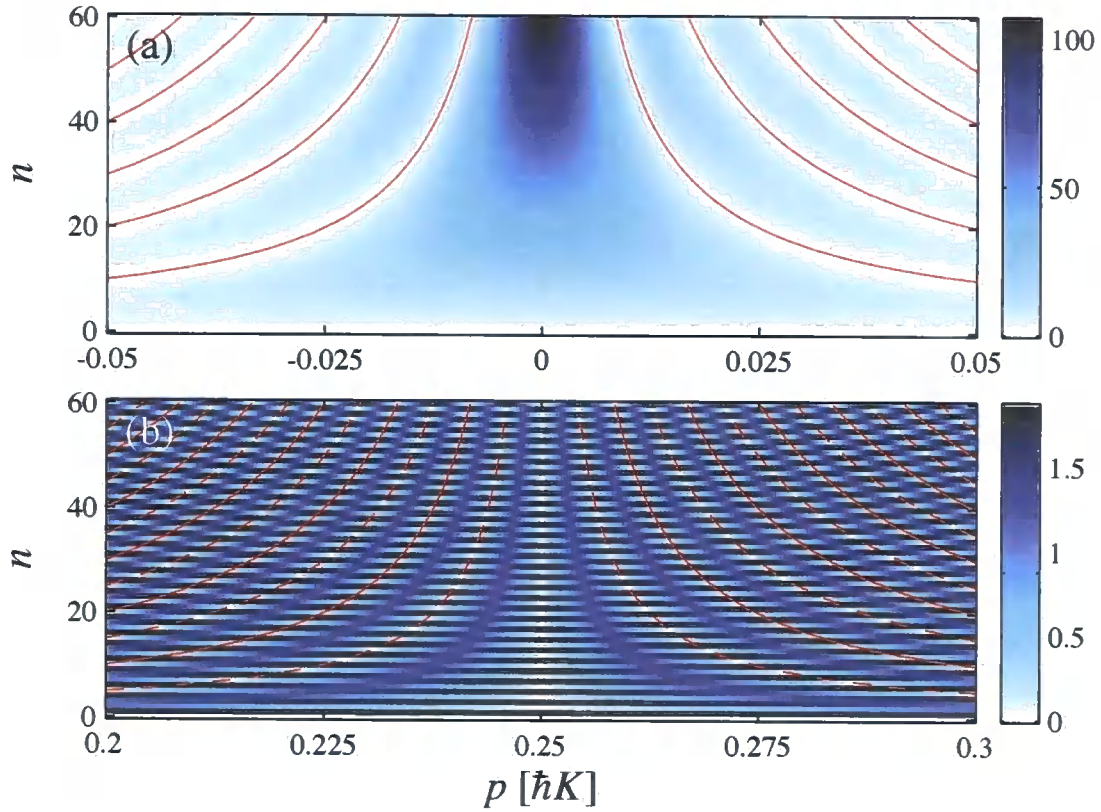

Figure 9.3: The evolution of the δ-kicked particle, initially in the plane-wave state $|\beta\rangle$, subject to subsequent applications of Floquet operator (4.12). The colour scale quantifies $\langle\langle\hat{p}^2\rangle\rangle_n^{1/2}$, in units of $\hbar K$, which is proportional to the kinetic energy of the particle. Parameters are $T = T_T$ ($\ell = 2$), $\Omega = 0$, $\phi_d = 0.8\pi$, and $\mathcal{N} = 1$ ($w = 0$). We show the features from Fig. 9.1(c) in detail: the quantum resonance in the vicinity of $\beta = 0$ (a), with the analytic asymptotes corresponding to Eq. (9.12); and the quantum antiresonance in the vicinity of $\beta = 0.25$ (b), with the analytic asymptotes corresponding to Eq. (9.14).

transition loci are described by $\bar{\beta}^R = \pm 1/2N\ell$. We quantify the quantum resonance width by the separation in β between the two transition loci adjacent to the quantum resonance, which is evaluated to be

$$\delta\beta_R = \frac{1}{N\ell}. \tag{9.13}$$

Quantum antiresonance width

A measure of the second-order quantum antiresonance width can be determined in a similar way to the quantum resonance case, by considering the closest Nth-order quantum antiresonances near an $N = 2$ quantum antiresonance. In general, the high-order quantum antiresonances in close proximity to an $N = 2$ quantum antiresonance occur for $\bar{\beta} =$

$\beta - \beta_m^A$, where β satisfies the high-order quantum antiresonance condition (9.10).

The reconstruction loci, given by the red lines in Figs. 9.2(a) and 9.3(b), are in agreement with the analytic lines derived by K. J. Challis to be [1]

$$\bar{\beta}^A = \mu'/2N\ell, \tag{9.14}$$

where μ' is an integer.

Looking closely at the reconstruction loci adjacent to the quantum antiresonances in Figs. 9.2(a) and 9.3(b), it is possible to confirm that adjacent reconstruction loci correspond to opposite parity[2], with the dashed lines corresponding to odd values of μ' and the solid lines corresponding to even values of μ'.

Transition loci can be defined which lie halfway between the $N = 2$ quantum antiresonance at β_m^A and the closest reconstruction loci described by $\bar{\beta} = \pm 1/2N\ell$. In the quantum antiresonance case the transition loci $\bar{\beta}^A = \pm 1/4N\ell$ are the sequence of points for which the even parity of the $N = 2$ quantum antiresonance changes over to the odd parity of the closest higher-order quantum antiresonances. The width of a second-order quantum antiresonance can be characterised by the separation in β between the transition loci $\bar{\beta}^A = \pm 1/4N\ell$, given by

$$\delta\beta_A = \frac{1}{2N\ell}. \tag{9.15}$$

The quantum antiresonance width (9.15) is a factor of two narrower than the quantum resonance width $\delta\beta_R$, as is evident from Figs. 9.2 and 9.3.

Temperature dependence

For an atomic gas with low w, the initial momentum distribution is centred around the quantum resonance or quantum antiresonance feature, and thus evolves in accordance with the ultracold limit. For high w values, the initial momentum distribution is spread across the full range of β, and therefore evolves as a superposition of the individual eigenstates.

Developing an understanding of the quasimomentum dependence develops our understanding of the transition between the behaviour for a zero-momentum eigenstate, and for a broad thermal distribution. In Chapter 10, we make use of this information to explore this transition for a finite temperature cloud of atoms.

[2]Due to the different colour scale, this level of detail is impossible to resolve in Fig. 9.1.

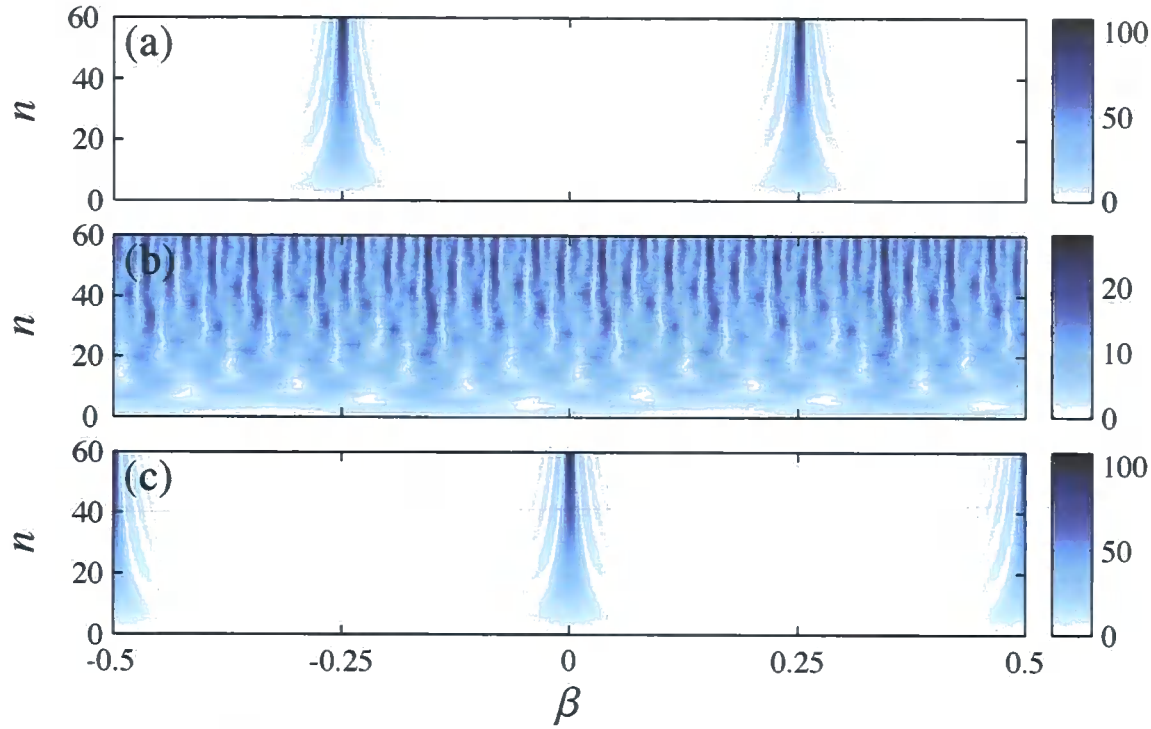

Figure 9.4: The evolution of the δ-kicked particle, initially in the plane-wave state $|\beta\rangle$, subject to subsequent applications of Floquet operator (4.12). The colour scale quantifies $\langle\langle\hat{p}^2\rangle\rangle_n^{1/2}$, in units of $\hbar K$, which is proportional to the kinetic energy of the particle. Gravity parameter, (a) $\Omega = 1$; (b) $\Omega = (1+\sqrt{5})/2$; and (c) $\Omega = 2$. Parameters are $T = T_T$ ($\ell = 2$), $\phi_d = 0.8\pi$, and $\mathcal{N} = 1$ ($w = 0$). The quantum resonance features are summarised in Table 9.2.

9.3 The δ-kicked accelerator: Dependence upon gravity parameter Ω

We follow the procedure from Chapters 7 and 8, comparing integer and irrational values of Ω before investigating high order effects by selecting a rational value of Ω

9.3.1 Comparison of integer with irrational values of Ω

In this section, we investigate the quasimomentum dependence, in order to investigate the effect of setting the Ω value to an integer. In Fig. 9.4, we present the evolution of $\langle\langle\hat{p}^2\rangle\rangle_n^{1/2}$, comparing integer values of Ω with an irrational value. We show results for $\Omega = 1$ in Fig. 9.4(a), and $\Omega = 2$ in Fig. 9.4(c). In Fig. 9.4(b) we present the results when setting Ω to an irrational value known as golden ratio, as discussed in Section 7.3.1. We

Gravity parameter	$\beta = 0$	$\beta = \pm 1/4$	$\beta = \pm 1/2$
$\Omega = 1$	Antiresonance	Resonance	Antiresonance
$\Omega = (1 + \sqrt{5})/2$	Non-resonant	Non-resonant	Non-resonant
$\Omega = 2$	Resonance	Antiresonance	Resonance

Table 9.2: The quantum resonant features for the δ-kicked accerator, for which $T = T_T$ ($\ell = 2$). Results are summarised for the pulse period values presented in Fig. 9.4.

find that the quantum resonant features observed for rational values become irregular and less well defined.

For $T = T_T$ ($\ell = 2$), there are two quantum resonance features across the range of β, as seen in Figs. 9.4(a) and (c). For $\Omega = 1$ the quantum resonance and quantum antiresonance features are shifted in momentum by 1/4 compared to the $\Omega = 2$ case. This is consistent with results for the $\beta = 0$ subspace, corresponding to the features shown in Fig. 7.2. The results for a thermal distribution, shown in Fig. 8.2 are obtained by taking an average over the evolution results for a Gaussian distribution of the initial momentum states.

9.3.2 Rational values of Ω

In Fig. 9.5 we present the quasimomentum dependence for rational values of Ω. We draw a comparison with the δ-kicked rotor by setting $\Omega = 0$ in Fig. 9.5(a). The parameters are the same as for Fig. 9.1(c), for which quantum resonances occur for $\beta = 0$ and $\beta = \pm 1/2$, and quantum antiresonances occur for $\beta = \pm 1/4$. This quasimomentum scan is also identical to Fig. 9.4(a), for which $\Omega = 2$.

For $\Omega = 1/s$, Figs. 9.5(b)–(d) show that increasing s increases the density in β of the quantum resonant features. However, the quantum resonances and quantum antiresonances remain evenly spaced and, as we discuss in the next section, the width of the fractional quantum resonances are independent of s.

Fractional quantum resonance conditions

It is possible to quantify the β separation between fractional quantum resonances. Fractional quantum resonances occur when [2]

$$s[r - (1 + 2\beta)\ell] = 2m \tag{9.16}$$

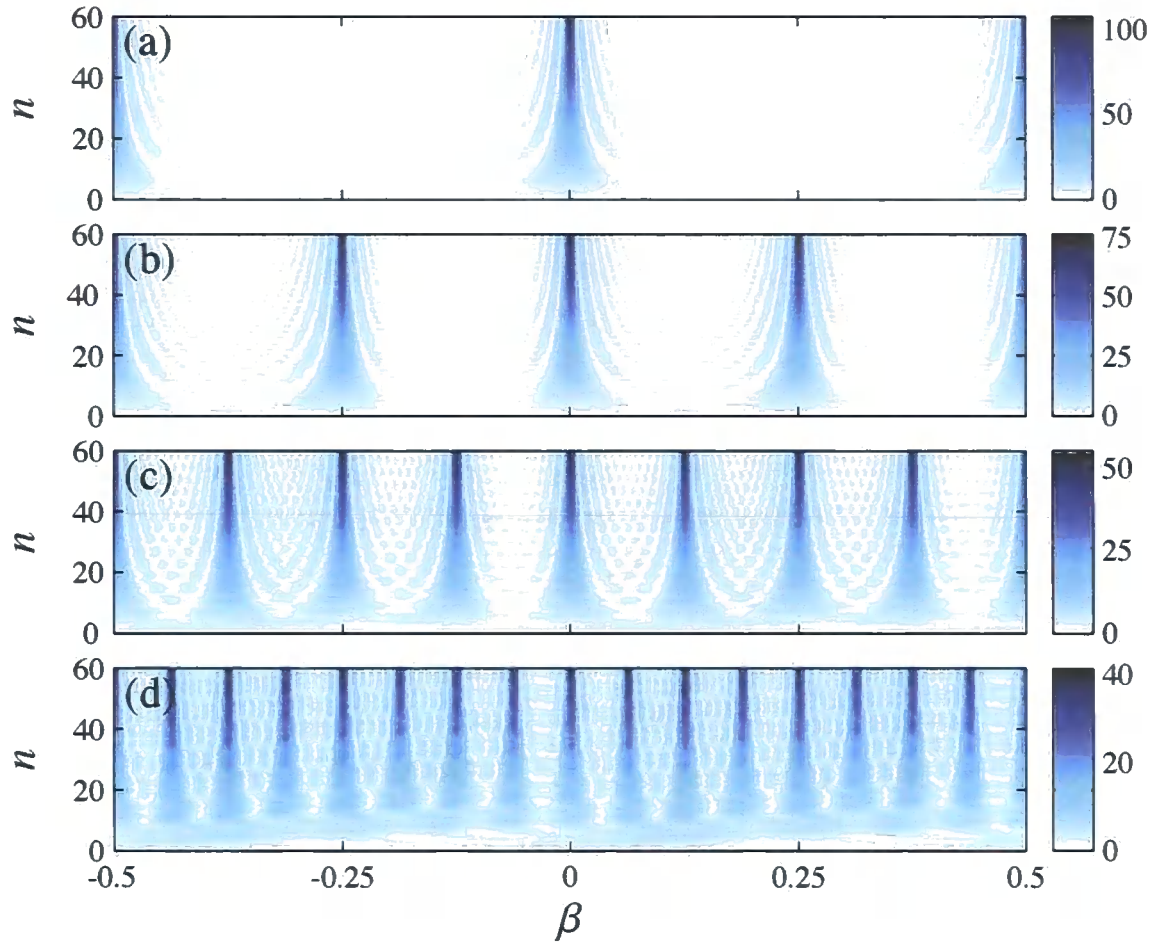

Figure 9.5: The evolution of the δ-kicked particle, initially in the plane-wave state $|\beta\rangle$, subject to subsequent applications of Floquet operator (4.12). The colour scale quantifies $\langle\langle\hat{p}^2\rangle\rangle_n^{1/2}$, in units of $\hbar K$, which is proportional to the kinetic energy of the particle. Gravity parameter, (a) $\Omega = 0$; (b) $\Omega = 1/2$; (c) $\Omega = 1/4$; (d) $\Omega = 1/8$. Parameters are $T = T_T$ ($\ell = 2$), $\phi_d = 0.8\pi$, and $\mathcal{N} = 1$ ($w = 0$). The high-order quantum resonance features are summarised in Table 9.3, and analysed in detail for in Fig. 9.6

for integer values of m. Inverting this, we find that fractional quantum resonances occur for quasimomentum values

$$\beta_m^{\mathrm{FR}} = \frac{r-\ell}{2\ell} - \frac{m}{\ell s}. \tag{9.17}$$

The fractional quantum resonances are separated in momentum by $1/\ell s$, breaking up momentum space into qualitatively similar, although not identical regions. The fractional quantum resonances observed in Fig. 9.5 are consistent with Eq. (9.17).

Gravity parameter	Resonance	β_m^{FR}
$\Omega = 0$	1st-order	$0, \pm 1/2$
$\Omega = 1/2$	2nd-order	$0, \pm 1/2, \pm 1/4$
$\Omega = 1/4$	4th-order	$m/8$
$\Omega = 1/8$	8th-order	$m/16$

Table 9.3: The quantum resonant features for the δ-kicked accerator, for which $T = T_T$ ($\ell = 2$). Results are summarised for the pulse period values presented in Fig. 9.5. For rational values of $\Omega = r/s$, quantum resonances of order s are located at quasimomentum values $\beta = \beta_m^{\mathrm{FR}}$, given by Eq. (9.17). Quantum antiresonance features are located between each quantum resonance.

Fractional quantum resonance width

Fractional quantum resonances have a momentum width that depends on ℓ and the kick number n. As shown for the δ-kicked rotor in Section 9.2.3, an expression for the fractional quantum resonance width can be derived by considering the quantum antiresonance features in close proximity to the fractional quantum resonances. In Fig. 9.6, we show in detail the $\beta = 0$ fractional quantum resonances from Figs. 9.5.

We find that the reconstruction loci are described by Eq. (9.12) [3]. Our analytic results indicate that the quantum resonance width given by Eq. (9.13) is independent of s, for $s = 1$ and $s = 2$. The numerical calculations in Figs. 9.6(c) and (d) indicate that the width of the fractional quantum resonances are independent of s.

9.4 Conclusions

In this chapter, we have shown the evolution of individual momentum eigenstates.

Quantum resonant effects may be observed by tuning to specific values of the system parameters, as seen in Section 9.2 for integer multiples of the half-Talbot time, and in Section 9.3 for rational values of gravity parameter Ω. The width of the quantum resonant features is inversely proportional to N, corresponding to the Nth-order quantum antiresonance feature. Since the Nth order quantum antiresonance recovers its initial state following n kicks, a precision measurement of β may be performed by tuning to a quantum resonance feature for a large number of laser pulses, as introduced in Section 4.5.2. We observed that the density of the fractional quantum resonance features is dependent upon the value of Ω, while the width of the quantum resonant features is found to be independent of Ω.

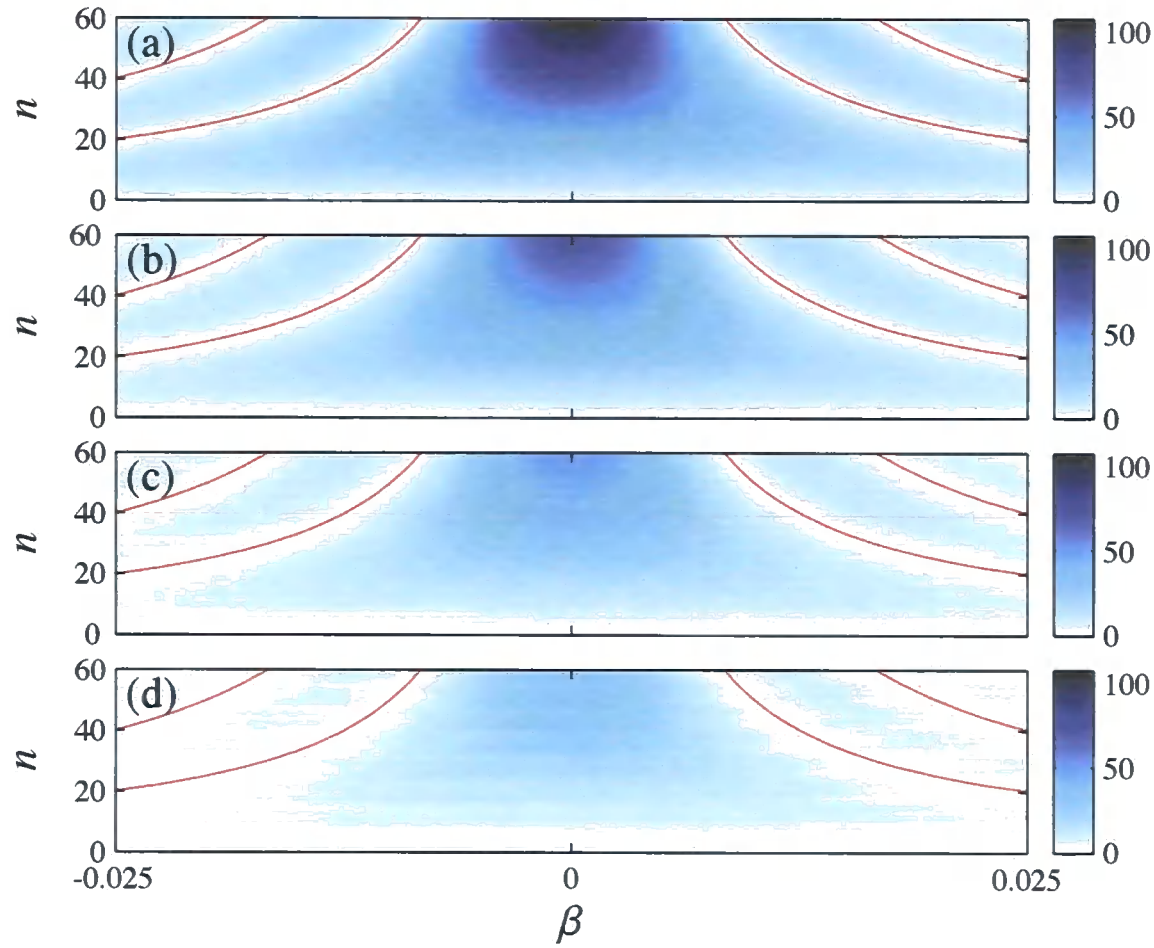

Figure 9.6: The evolution of the δ-kicked particle, initially in the plane-wave state $|\beta\rangle$, subject to subsequent applications of Floquet operator (4.12). The colour scale quantifies $\langle\langle\hat{p}^2\rangle\rangle_n^{1/2}$, in units of $\hbar K$, which is proportional to the kinetic energy of the particle. Gravity parameter, (a) $\Omega = 0$; (b) $\Omega = 1/2$; (c) $\Omega = 1/4$; (d) $\Omega = 1/8$. Parameters are $\mathcal{N} = 1$ ($w = 0$), $\phi_d = 0.8\pi$, $T = T_T$ ($\ell = 2$). We show the fractional quantum resonances from Fig. 9.5 in detail, with the analytic asymptotes corresponding to Eq. (9.12).

We have demonstrated agreement between numerical simulation and analytic results:

1. In Chapter 7, we applied the time evolution operator to a zero temperature initial condition, and showed that this coincided with the expected momentum moments summarised in Table 7.1.

2. In Chapter 8, we evaluated the numerical simulations for a thermal initial condition, which is compatible to the expected momentum moments summarised in Table 8.1.

3. In this chapter, we showed Eqs. (9.12) and (9.14) coincide with the Nth order

quantum antiresonances in Figs. 9.2, 9.3, and 9.6.

We now extend the analysis to intermediate temperatures, modelled by a Gaussian distribution of the momentum eigenstates presented in this chapter. We consider the δ-kicked rotor in Chapter 10 for various values of T, and the δ-kicked accelerator in Chapter 11 for various values of Ω.

Chapter 10

Temperature dependence of the δ-kicked rotor

10.1 Overview

In Chapter 9 we found that the evolution of the momentum variance for momentum eigenstates $|k+\beta\rangle$ depends dramatically on the quasimomentum β, but is independent of the discrete momentum k. This means that the evolution of a δ-kicked rotor, with a Gaussian initial momentum distribution given by Eq. (5.14), depends sensitively on the initial population of β eigenstates [32]. In particular, if the initial momentum distribution is broad compared to the momentum separation $1/\ell$ between consecutive quantum resonance features, the range of individual momentum eigenstate evolutions occur simultaneously. In this case an averaged evolution results [47, 50, 52].

In this chapter we investigate in detail the effect of the initial momentum distribution width w on the evolution of a δ-kicked rotor. We give analytic expressions for the second-order momentum moment evolution for both a zero-momentum eigenstate, as seen in Fig. 7.1, and for a finite temperature cloud, as seen in Fig. 8.1.

We make use of the quasimomentum dependence, as described in Chapter 9, to understand the changeover between the zero-temperature regime where quantum resonant and quantum antiresonant features are distinct, and the finite temperature case where the system energy is observed to grow linearly, as seen from Figs. 8.1(b) and (f).

Note that in this chapter, we consider atomic momentum distributions that are symmetric around zero. Thus, it is equivalent to consider either the second-order momentum moment or the momentum variance, as seen from Eq. (5.12). We consider the former for

notational convenience.

10.2 Quantum resonant dynamics

In this chapter, we consider the δ-kicked rotor, for which $\Omega = 0$. As we are in an integer Ω regime, for which first-order quantum resonant effects are exhibited, we set $s = 1$. For a zero-momentum eigenstate, quantum resonance occurs for even values of ℓ, as defined with Eq. (3.33). At a quantum resonance, the second-order momentum moment evolves quadratically according to Eq. (5.20) setting $\beta = 0$, $s = 1$, and ℓ even. The quadratic dependence of the second-order momentum moment with the kick number n is illustrated in Fig 7.1(f). In contrast, the energy of a finite temperature cloud grows linearly at a quantum resonance, as shown in Fig. 8.1(f).

10.2.1 Comparison of numerical results with the analytic limiting cases.

In Fig. 10.1, the markers show the numerical results for the evolution of the second-order momentum moment for three initial Gaussian momentum distributions with different values of the standard deviation w. We observe that the momentum moment initially follows the quadratic growth of the zero-momentum eigenstate case, as indicated by the dashed line in Fig. 10.1. For a finite temperature cloud, the ballistic expansion becomes limited at a particular kick number, denoted n_R. Above n_R the rate of energy growth begins to revert to the classical diffusion result (5.24), as indicated by the lower dotted line in Fig. 10.1. For large w, the energy growth is bounded below by the classical result (5.24), as seen previously in Fig. 8.1(f).

10.2.2 The quantum resonance transition time, n_R

The behaviour observed in Fig. 10.1 can be understood by considering the range of β subspaces initially populated. The quantum resonance width was found in Section 9.2.3 to be $\delta\beta_R = 1/N\ell$, as given by Eq. (9.13). Provided that the initial momentum width of the cloud is well within the quantum resonance width, quantum resonant dynamics dominates the system evolution. Conversely, if the initial momentum width is larger than the quantum resonance width, the higher-order quantum antiresonances play a significant role and the ballistic expansion is limited.

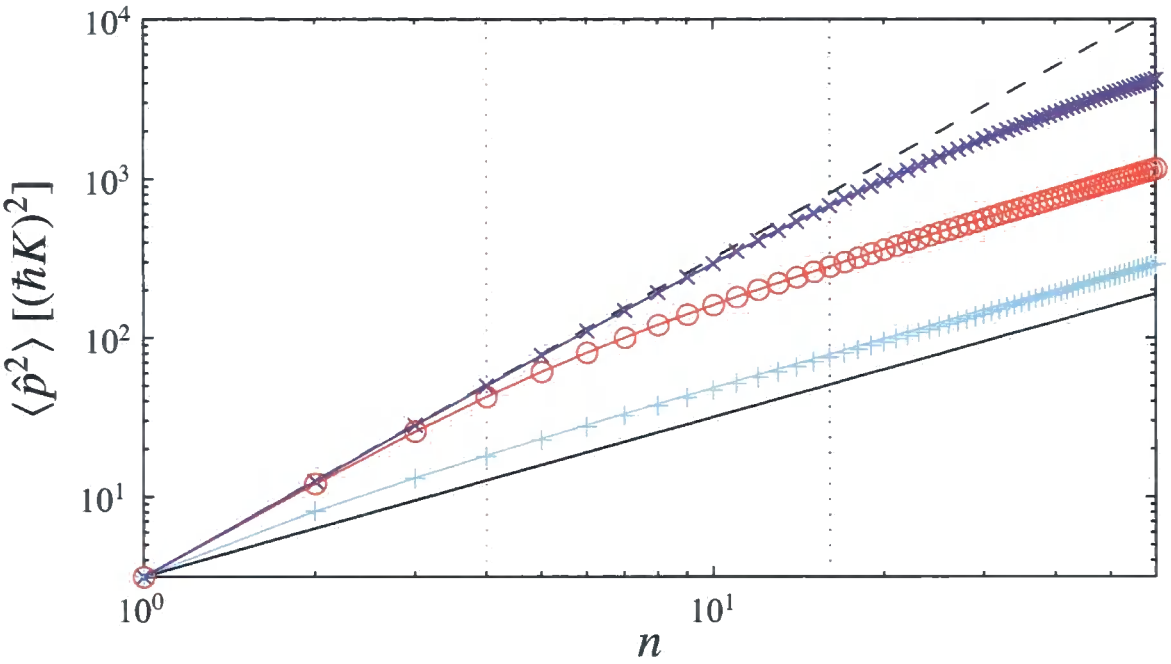

Figure 10.1: The second-order momentum moment $\langle \hat{p}^2 \rangle$ of a δ-kicked atom cloud. The initial state is a Gaussian momentum distribution with standard deviation ($\times$) $w = 1/128$; ($\circ$) $w = 1/32$; and ($+$) $w = 1/8$. Parameters are $T = T_T$, $\Omega = 0$, $\phi_d = 0.8\pi$, and $\mathcal{N} = 10000$. The analytic result from Eq. (10.2) are shown by the solid lines, with the colour of these lines indicating the value of w, corresponding to the same colour as the markers used to plot the numerical results. The black lines show the analytic limiting cases, with the dashed line corresponds to the quadratic growth (5.20), and the solid line corresponds to the classical linear growth (5.24) setting $w = 0$. The vertical dotted lines indicate $n = n_R$, as defined in Eq. (10.1).

Quantitatively, we define a kick number n_R to indicate the number of kicks at which the ballistic expansion becomes limited. We define the quantum resonance transition time n_R so that two standard deviations of the initial Gaussian momentum distribution lie within the quantum resonance width $\delta\beta_R$, such that

$$n_R \equiv \frac{1}{4w\ell}. \tag{10.1}$$

This equation (10.1) ensures that 95.4 % of the atom cloud expands ballistically up until the kick number n_R, as indicated by the red and blue vertical dotted lines in Fig. 10.1.

10.2.3 Analytic results for a finite temperature gas

In Appendix E, we derive expressions for the momentum moments for a finite temperature gas. We follow a method developed by P. L. Halkyard [2], which considered integer values of Ω, with the initial momentum distribution approximated by Gaussian function (5.14). For the δ-kicked rotor, the second-order momentum moment evolves according to

$$\frac{\langle \hat{p}^2 \rangle_n}{(\hbar K)^2} = w^2 + \frac{\phi_d^2}{2} n + \phi_d^2 \sum_{m=1}^{n-1} (n-m)(-1)^{m(r_1+\ell)} e^{-2m^2\ell^2\pi^2 w^2}. \tag{10.2}$$

The analytic lines shown Fig. 10.1 demonstrate good agreement with our numerical results. In Chapter 10, we extend the numerical analysis by varying the value of the gravity parameter Ω.

10.3 Quantum antiresonant dynamics

The effect of the initial atomic momentum width on the second-order momentum moment evolution at a quantum antiresonance is shown in Fig. 10.2. The evolution can be separated into two regimes: (i) when $w \ll 1/2\ell$ periodic oscillations are observed, as seen in Fig. 10.2(a), and (ii) for $w \gtrsim 1/2\ell$ for which the momentum moment grows linearly, as seen in Fig. 10.2(b). For large w, the energy growth is bounded above by the classical result (5.24), which was demonstrated in Fig. 8.1(b).

10.3.1 The quantum antiresonance transition time, n_A

As in the quantum resonance case, we can define a kick number n_A below which the majority of plane-wave components in the distribution exhibit a first order quantum antiresonance effects, with period $2T$. Requiring that two standard deviations of the initial Gaussian atomic momentum distribution lie within the quantum antiresonance width $\delta\beta_A$, as derived with Eq. (9.15), we find that

$$n_A = \frac{1}{8w\ell}. \tag{10.3}$$

In Fig. 10.2(a), the kick numbers n_A are indicated by the vertical dotted lines. For kick numbers less than n_A the initial state recurrence with period $2T$ is clearly observed.

In the low temperature regime, where $w \ll 1/2\ell$, as in Fig. 10.2(a), we observe oscil-

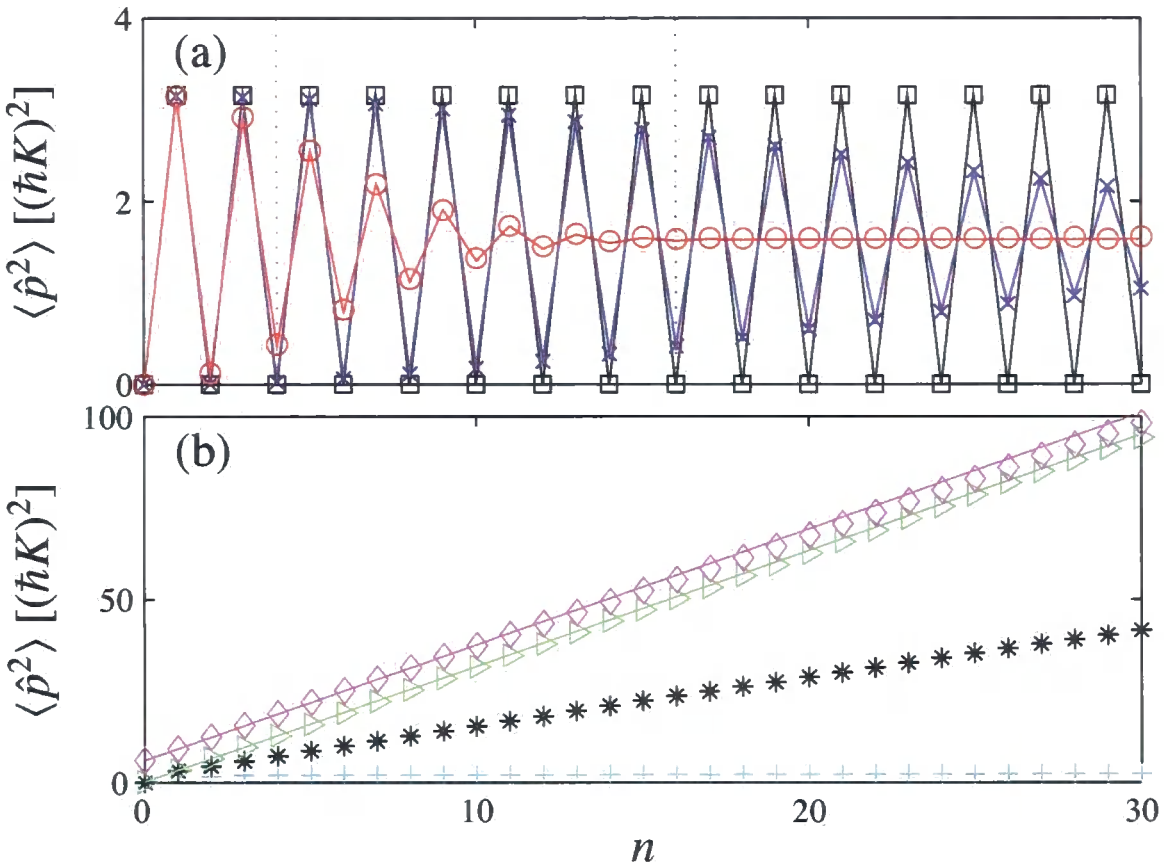

Figure 10.2: The second-order momentum moment $\langle \hat{p}^2 \rangle$ of a δ-kicked atom cloud. The initial state is a Gaussian momentum distribution with standard deviation (a) ($\square$) $w = 0$; ($\times$) $w = 1/128$; and ($\circ$) $w = 1/32$; and (b) ($+$) $w = 1/8$; ($*$) $w = 1/4$; ($\triangleright$) $w = 1/2$; and ($\diamond$) $w = 2.5$. Parameters are $T = T_T/2$, $\Omega = 0$, $\phi_d = 0.8\pi$, and $\mathcal{N} = 10000$. In (a) the solid lines are given by Eq. (10.4) and the vertical dotted lines indicate $n = n_A$, as defined by Eq. (10.3). The solid lines in (b) are given by Eq. (5.24).

lations with period $2T$ even after $n = n_A$. However, the oscillations decay to a constant value. The momentum moment evolution in the low temperature regime is well approximated by [1]

$$\langle \hat{p}^2 \rangle_n \approx \frac{1}{4}\hbar^2 K^2 \phi_d^2 \left[1 - \cos(n\pi) e^{-2n^2\pi^2\ell^2 w^2}\right] + \hbar^2 K^2 w^2, \tag{10.4}$$

as shown by the solid lines in Fig. 10.2(a). The derivation of Eq. (10.4) is due to K. J. Challis.

The observed decay in the periodic oscillations occurs when the initial momentum width of the cloud is comparable to, or larger than, the quantum antiresonance width $\delta\beta_A$. Provided that $w \ll 1/2\ell$, higher-order quantum antiresonances begin to play a role

in the system dynamics, but quantum resonances do not. In this regime the evolution of the different β subspaces can be described as an oscillation of the same amplitude as the $\beta = 0$ subspace, but with a different phase. This means that the different β subspaces gradually become out of phase with each other, leading to a decay in the oscillation of the second-order momentum moment. The decay of the oscillations has been observed experimentally by Duffy *et al.* [63].

For the case where $w \gtrsim 1/2\ell$, as shown in Fig. 10.2(b), certain initially populated β subspaces fulfill the quantum resonance condition (9.4), and consequently the second-order momentum moment is observed to grow linearly. For broad momentum distributions, the gradient of the moment growth tends to the thermal limit given by Eq. (5.24).

10.4 Conclusions

In this chapter we have theoretically investigated the quantum resonant dynamics of δ-kicked cold atoms. In particular we have shown how the behaviour of the second-order momentum moment changes for progressively broader initial momentum distributions. By increasing the initial temperature of the atomic cloud from the ideal case of zero Kelvin, we have identified transition times, as a function of the initial momentum width, after which the dynamics of the quantum resonance and quantum antiresonance clearly deviate from the ideal zero temperature case. This can be understood from the time evolution of individual momentum eigenstates, which we showed in Chapter 9 varies greatly with the quasimomentum.

Laser cooling below the photon recoil limit, discovered by Philips [113], with significant developments by Chu [134–136] and Cohen-Tannoudji [137, 138], enabled the dynamics of quantum systems to be analysed by reducing the kinetic energy along the axis of the time-of-flight momentum measurement. Typical temperatures achieved with an initially magneto-optically trapped sample, such as for the value of $w = 2.5$ used in the Oxford experiment [16–18, 21, 55–58, 60], observe a linear-with-time increase of the mean kinetic energy. In this case there is very little to distinguish quantum resonant from quantum antiresonant evolution [47, 50, 57, 139]. However, along one dimension, narrower initial momentum distributions are achievable, with examples shown in Table 10.1. In three-dimensions, it has been shown that a Bose-Einstein condensate has been cooled below 500 pK [140], using a technique known as velocity-selective coherent population trapping [141].

Species	Technique	λ [nm]	$\mathcal{T}_w$	w	Reference
^{87}Rb	BEC	780	3 nK	0.043	[63]
^{133}Cs	1D Raman	895	3 nK	0.062	[142]
^{133}Cs	BEC	895	46 pK	0.008	[119]
^{23}Na	1D Raman	589	24 pK	0.0016	[134]

Table 10.1: Experimental accessibility of the ultracold temperature regime. Various cooling mechanisms are possible, with results obtained for alkali-earth metals from group I of the periodic table. The effective one-dimensional temperature $\mathcal{T}_w$ is determined from the momentum distribution spread, which we approximate to a Gaussian function, as explained in Section 5.3. The width of the momentum distribution, $w\ \hbar K$, is extracted from the standard deviation of the thermal distribution using Eq. (5.15).

Chapter 11

Temperature dependence of the δ-kicked accelerator

11.1 Overview

We now generalise the discussion of the time evolution for a finite temperature gas by varying the value of gravity parameter Ω, thus realising the δ-kicked accelerator. To investigate the correspondence between classical and quantum counterparts of the δ-kicked accelerator, we analyse the fourth-order momentum cumulant using linear regression analysis. We present the results from Publication [3].

11.2 Momentum moment evolution

We investigate the dependence of the initial atom cloud temperature on the system dynamics by considering the evolution of the momentum moments for a Gaussian initial atomic momentum distribution. We vary the widths of the distribution, as given by Eq. (5.14). In Fig. 11.1, we show the evolution of $\langle \hat{p}^2 \rangle_n$ and $\langle \hat{p}^4 \rangle_n$ for different values of w and Ω.

11.2.1 Comparison of the numerical results to the analytic limiting cases

As w increases, for a given Ω, the momentum moment evolutions make a gradual transition from the zero-temperature limit behaviour discussed in Chapter 7, towards the thermal

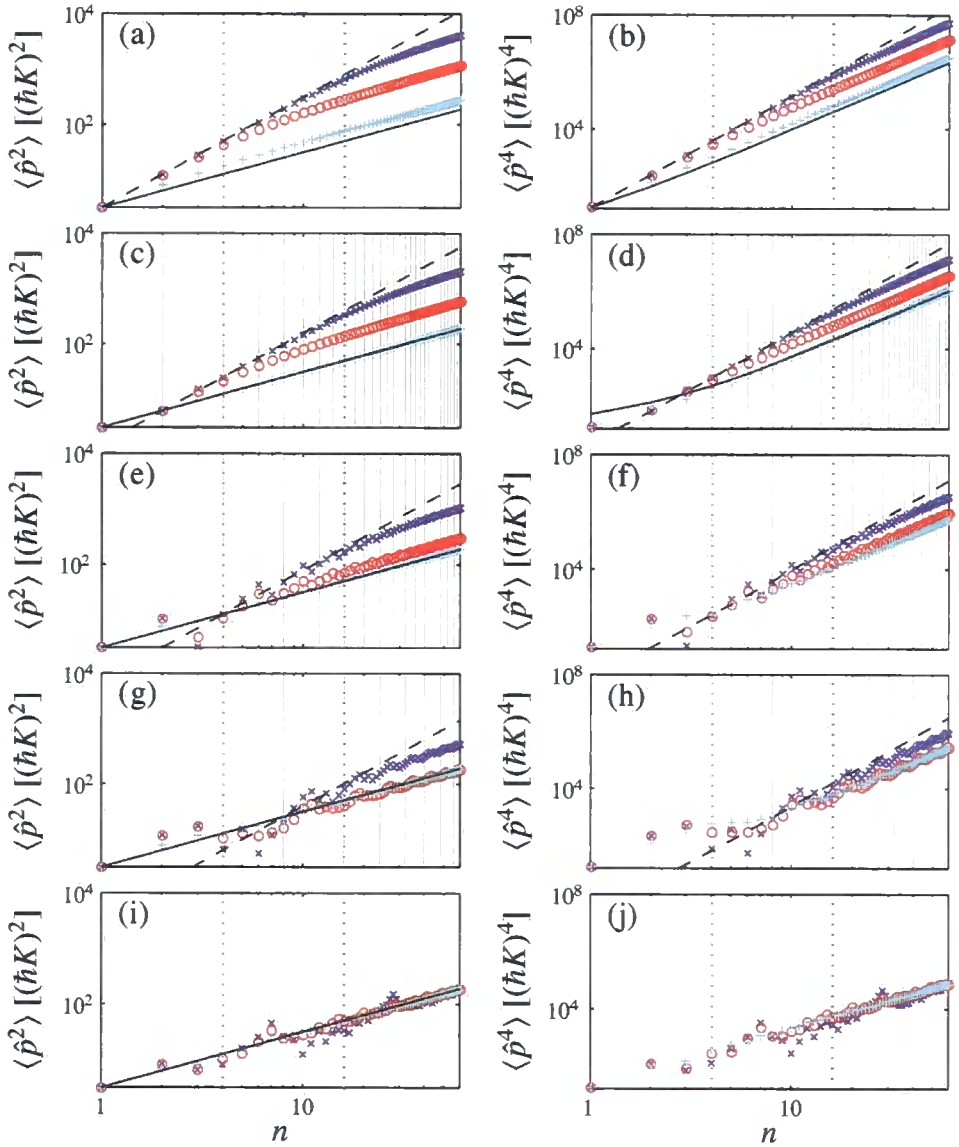

Figure 11.1: The momentum moments $\langle \hat{p}^q \rangle_n$ of order $q = 2$ [left-hand column] and $q = 4$ [right-hand column], for a Gaussian initial atomic momentum distribution with ($\times$) $w = 1/128$; ($\circ$) $w = 1/32$; and ($+$) $w = 1/8$. Parameters are $T = T_T$ ($\ell = 2$), $\phi_d = 0.8\pi$, $\mathcal{N} = 10000$, and (a), (b) $\Omega = 0$; (c), (d) $\Omega = 1/2$; (e), (f) $\Omega = 1/4$; (g), (h) $\Omega = 1/8$; and (i), (j) $\Omega = (1+\sqrt{5})/2$. The dashed lines correspond to the $w = 0$ analytic predictions [Eq. (5.20) for $\langle \hat{p}^2 \rangle_n$ and Eq. (5.21) for $\langle \hat{p}^4 \rangle_n$]. The solid lines correspond to the large-w limit lower bound [Eq. (5.24) for $\langle \hat{p}^2 \rangle_n$; Eq. (5.25) in (b); and Eq. (5.26) in (d), all with $w = 0$]. The vertical dotted lines indicate $n = n_{\rm FR}$ [see Eq. (11.1)], and the solid vertical lines in (c) – (h) indicate where n is an integer multiple of s (as taken from $\Omega = 1/s$), for which values the analytic equations are valid. The quantum resonance features in (a) are equivalent to the results presented in Fig. 10.1 for the δ-kicked rotor.

limit described in Chapter 8. The dashed lines in Fig. 11.1 indicate the zero-temperature limit, given by Eq. (5.20) for the second-order momentum moment, and (5.21) for the fourth-order momentum moment.

The solid lines in the figure are lower bounds to the momentum moment evolutions in the thermal limit. The analytic expressions in the thermal limit are summarised in Table 8.1, evaluated with $w = 0$. For the second-order momentum moment, the solid lines correspond to Eq. (5.24) with $w = 0$. Note that for finite w, the thermal limit of $\langle \hat{p}^2 \rangle_n$ is larger than that for $w = 0$, but will increase at the same rate. For the fourth-order momentum moment evolution, the lower bounds depend on Ω and are defined by setting $w = 0$ in Eq. (5.25) for integer Ω, and Eq. (5.26) for half-integer Ω. We have not evaluated analytic expressions for the lower bounds for general rational Ω, although Figs. 11.1(f) and 11.1(h) strongly indicate that similar behaviour exists in the thermal limit.

11.2.2 The fractional quantum resonance transition time n_{FR}

The deviation of the momentum moment evolution from the zero-temperature limit occurs at a particular kick number n_{FR}, indicated by the vertical dotted lines in Fig. 11.1. As explained for the case of the δ-kicked rotor in Chapter 10, the energy transferred to the system becomes limited when the initial momentum width of the atom cloud becomes comparable with the momentum width of a quantum resonance.

If the initial momentum width is large compared to the quantum resonance width, the quantum antiresonances play a role in the system dynamics and the momentum moment evolution tends towards the thermal limit. We define n_{FR} such that two standard deviations of the initial Gaussian momentum distribution lie within the quantum resonance width $\delta\beta_{\mathrm{FR}}$,

$$n_{\mathrm{FR}} = \frac{1}{4w\ell}. \tag{11.1}$$

As described in Section 9.3.2, the width of a fractional quantum resonance feature is independent of Ω, and therefore, the expression for n_{FR} gives the same result as for the case of the δ-kicked rotor, seen from Eq. (10.1).

11.2.3 Thermalisation transition w_{th}

To study fractional quantum resonances, we set the gravity parameter to the rational value $\Omega = r/s$, where r and s are integers. In Fig. 11.1 we find that as the denominator s increases, the fractional quantum resonances become increasingly sensitive to the initial

temperature of the system. This effect is most clear from the second-order momentum moment[1], with the thermal limit given by Eq. (5.24), appearing to be independent of the gravity parameter.

We observe that as s increases, the momentum moments approach the thermal limiting behaviour for lower values of w. This is explained in terms of the number of quantum resonance features spanned by the initial atomic momentum distribution. The fractional quantum resonances are separated in momentum by $1/\ell s$, as seen from Fig. 9.5 and described in Section 9.3.2. Thus, we can define a thermalisation width w_{th}, above which the atomic momentum distribution initially spans more than a single quantum resonance feature and the atomic dynamics reach a thermal limit.

As explained in Chapter 5, thermalisation is manifest in linear rather than quadratic growth of $\langle \hat{p}^2 \rangle_n$, and cubic rather than quartic growth of $\langle \hat{p}^4 \rangle_n$. Quantitatively, we define w_{th} such that one standard deviation of the initial Gaussian momentum distribution lies within the separation of the fractional quantum resonance features, such that

$$w_{\text{th}} = \frac{1}{2\ell s}. \tag{11.2}$$

Finally, we note that if Ω is chosen to be irrational, as shown in Figs. 11.1(i) and 11.1(j), we observe that the second-order momentum moment grows linearly with n, and the fourth-order momentum moment grows quadratically. The data becomes smoother as w increases, but the growth rate appears to be largely independent of w.

11.3 Momentum cumulant evolution

We now examine the momentum cumulants, verifying that the analytic equations derived in Chapter 5 for limiting cases, and investigating the temperature dependence presenting the results of the numerical simulation described in Chapter 6.

11.3.1 Second-order cumulants

The second-order momentum cumulant evolution is essentially described by the second-order momentum moment evolution, since $\langle \hat{p} \rangle_n$ is negligible for a thermal distribution. However, by analysing the evolution of the change in the second-order momentum cumulant in Fig. 11.2, we find that the distinction between the ultracold and thermal regimes

[1]Note that Fig. 11.1(a), showing the numerical results for $\langle \hat{p}^2 \rangle$ with $\Omega = 0$, is equivalent to Fig. 10.1.

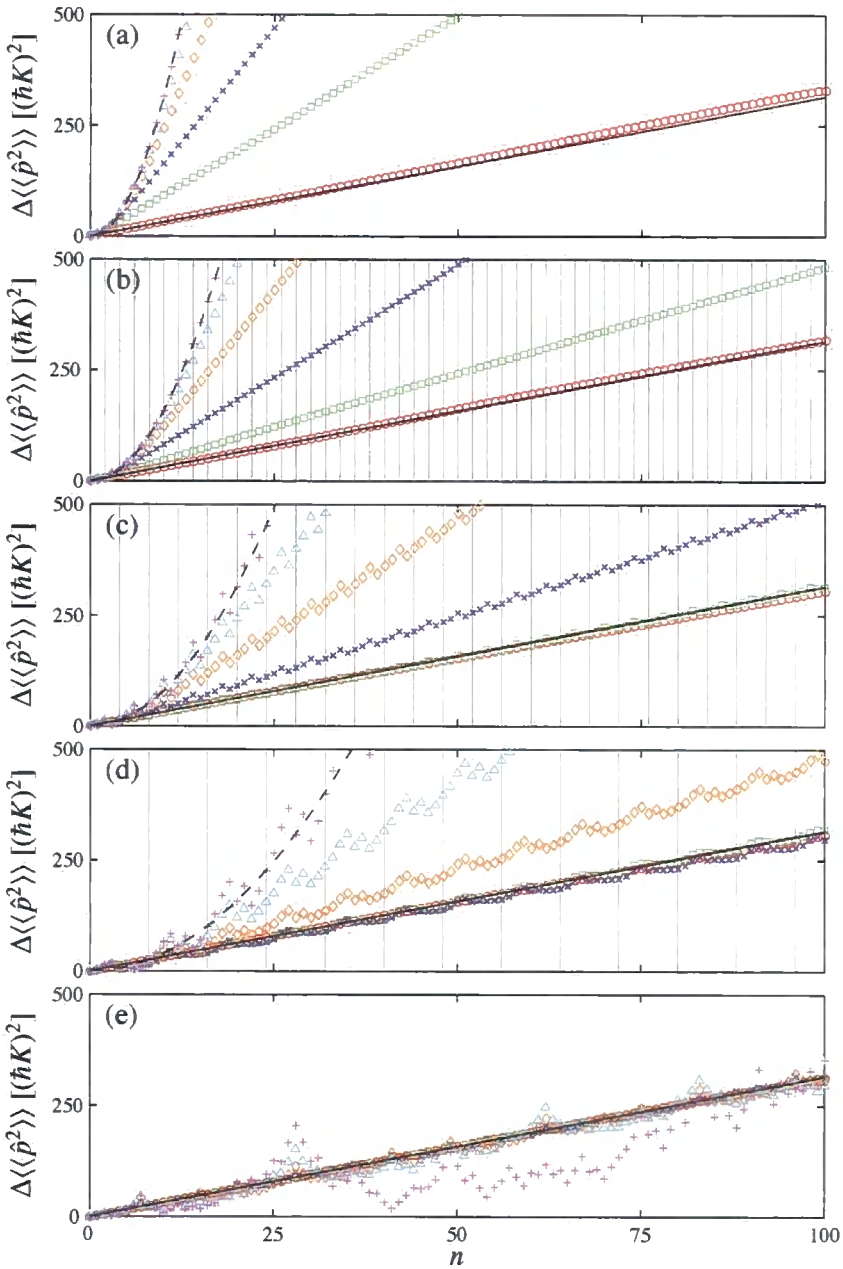

Figure 11.2: The increase in energy of an atom cloud ensemble, quantified by $\Delta\langle\langle\hat{p}^2\rangle\rangle_n$, subject to a δ-kicked accelerator with Gaussian initial momentum distribution of standard deviation ($\circ$) $w = 1/4$; ($\square$) $w = 1/16$; ($\times$) $w = 1/32$; ($\diamond$) $w = 1/64$; ($\triangle$) $w = 1/128$; and ($+$) $w = 1/1024$. Parameters are $T = T_T$ ($\ell = 2$), $\phi_d = 0.8\pi$, $\mathcal{N} = 10000$, and (a) $\Omega = 0$; (b) $\Omega = 1/2$; (c) $\Omega = 1/4$; (d) $\Omega = 1/8$; and (e) $\Omega = (1 + \sqrt{5})/2$. The dashed lines correspond to Eq. (5.20), and the solid lines correspond to Eq. (5.27). The vertical lines in (b)–(d) indicate where n is an integer multiple of s, where $\Omega = r/s$, for which values the analytic equations are valid.

is magnified. In this plot, we are simply presenting the data from the left-hand column of Fig. 11.1 in a slightly different format.

It is clear from Fig. 11.1(a) that the analytic and numerical methods are consistent for describing the ultracold and thermal regimes. Furthermore, intermediate temperatures exhibit dynamics in between these regimes, as previously discussed in Chapter 10. Varying the denominator of $\Omega = r/s$ in Figs. 11.1(b)–(d), the result given by Eq. (11.2) is verified. We observe that increasing the denominator s by a factor of two, the momentum width for which the thermal regime is adopted also scales by a factor of two. The vertical lines denote the kick numbers for which the analytic results are valid. We note that the numerical results are consistent with the equations where they are applicable, however, for intermediate kicks, it is apparent that dynamics deviates from the theoretical curves. It is clear from Fig. 11.1(e) that the fluctuations about the thermal result become erratic when the quantum resonant effects are removed by setting Ω to an irrational value.

11.3.2 Fourth-order cumulants

By analysing the evolution of the fourth-order momentum cumulant, we extract additional information about the dependence of the system upon temperature and gravity. In Fig. 11.3 we present the evolution of the cube root of the fourth-order momentum cumulant for different values of w and Ω. The reason for taking the cube root is that the thermal regime is then indicated by a straight line. Also, the sign of the cumulant value is preserved, which is important for understanding the shape of the distribution represented.

We observe that $\langle\langle \hat{p}^4 \rangle\rangle_n^{1/3}$ initially evolves according to the zero-temperature limit, indicated by the dashed lines in the figure. The fact that it is negative indicates a broad momentum distribution characteristic of quantum resonance phenomena. At the kick number $n = n_{\mathrm{FR}}$, defined in Eq. (11.1), the cumulants deviate from the zero-temperature limit, eventually becoming positive, indicating a sharply peaked momentum distribution which is caused by quantum antiresonances playing a significant role in the dynamics.

For irrational values of Ω, as seen from Fig. 11.3(e), the absence of quantum resonant features leads to the distribution gradually becoming broader, as indicated for a thermal distribution in Fig. 8.2(c). For low temperatures, the cumulant dynamics fluctuates erratically, as expected from Fig. 7.2(c).

For sufficiently large values of w, the fourth-order momentum cumulant tends to the thermal limit, indicated by the solid lines in Figs. 11.3(a) and (b). In the thermal limit,

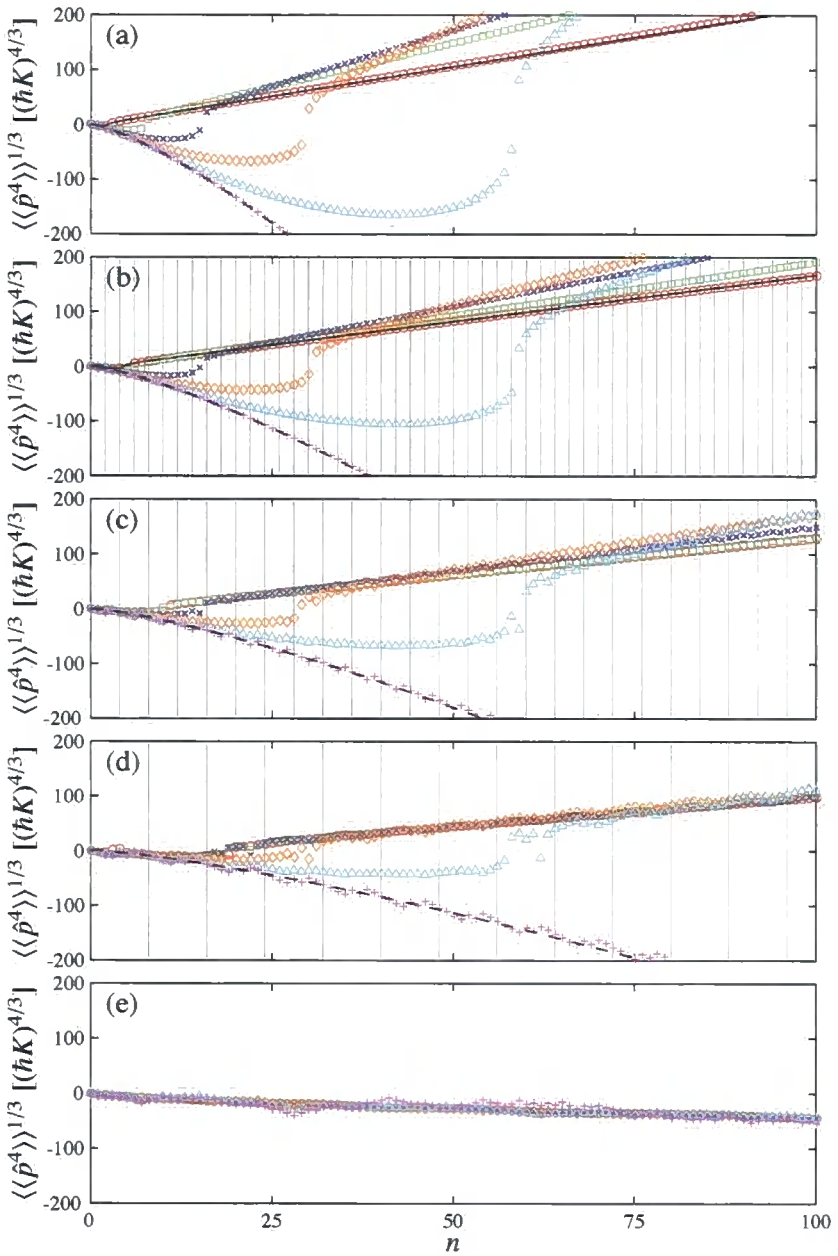

Figure 11.3: The change in shape of atom cloud ensemble, quantified by $\langle\langle\hat{p}^4\rangle\rangle_n^{1/3}$, subject to a δ-kicked accelerator with Gaussian initial momentum distribution of standard deviation (○) $w = 1/4$; (□) $w = 1/16$; (×) $w = 1/32$; (◇) $w = 1/64$; (△) $w = 1/128$; and (+) $w = 1/1024$. Parameters are $T = T_T$ ($\ell = 2$), $\phi_d = 0.8\pi$, $\mathcal{N} = 10000$, and (a) $\Omega = 0$; (b) $\Omega = 1/2$; (c) $\Omega = 1/4$; (d) $\Omega = 1/8$; and (e) $\Omega = (1+\sqrt{5})/2$. The dashed lines correspond to Eq. (5.23), and the solid lines correspond to (a) Eq. (5.28) and (b) Eq. (5.29). The vertical lines in (b)–(d) indicate where n is an integer multiple of s, where $\Omega = r/s$, for which values the analytic equations are valid.

the fourth-order momentum cumulant evolution, as described by Eqs. (5.28) and (5.29), is independent of w and is characterized by cubic growth with n. The growth rate is smaller for high values of denominator s, indicating that high-ordered fractional quantum resonances have less peaked momentum distributions, as seen in Fig. 8.3.

11.3.3 Linear regression analysis

In this section, we use a statistical tool to quantify the transition from an ultracold to a thermal regime. We choose the fourth-order momentum cumulant as the observable since the value of Ω has been shown to be resolvable in the thermal limit. We use linear regression analysis to determine the value of w for which $\langle\langle \hat{p}^4 \rangle\rangle^{1/3}$ adopts a linear profile [143].

For rational values of $\Omega = r/s$, we observe that for larger values of s, the cumulant evolution tends to the thermal limit behaviour more readily, adopting the thermal regime with smaller values of w. We have investigated this quantitatively by determining the asymptotic dependence of the fourth-order cumulant. This was done by fitting a particular number of asymptotic points using a least-squares method according to

$$\langle\langle \hat{p}^4 \rangle\rangle_n^{1/3} = bn + c. \tag{11.3}$$

Note that the linear fit values b and c incorporate the momentum units $[(\hbar K)^{4/3}]$. The most appropriate asymptote, with $b = b_{\mathrm{opt}}$, was identified by choosing the number of asymptotic points such that the standard error in the gradient b was minimized.

In Fig. 11.4 we show the optimum asymptote gradient b_{opt} as the width w of the Gaussian distribution is varied. We find that as w increases, the asymptote gradient saturates to its thermal limit value b_{th}, as indicated by the solid horizontal lines in Fig. 11.4. For integer values of Ω, we determine from Eq. (5.28) that

$$b_{\mathrm{th}} = (\phi_d^4/4)^{1/3}(\hbar K)^{4/3}, \tag{11.4}$$

as shown by the red line. For half-integer values of Ω, we determine from Eq. (5.29) that

$$b_{\mathrm{th}} = (\phi_d^4/8)^{1/3}(\hbar K)^{4/3}, \tag{11.5}$$

as shown by the green line.

Saturation to thermal value b_{th} occurs when the width of the initial atomic momentum

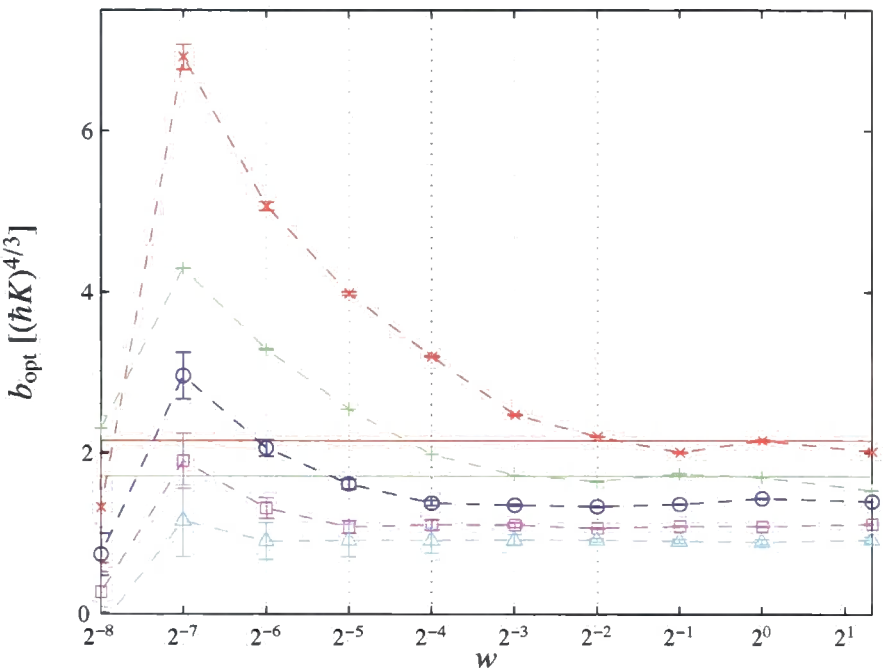

Figure 11.4: The asymptote gradient b_{opt} of $\langle\langle\hat{p}^4\rangle\rangle^{1/3}$, determined from Fig. 11.3 using linear regression analysis. Parameters are $T = T_T$ ($\ell = 2$), $\phi_d = 0.8\pi$, $\mathcal{N} = 10000$, and (×) $\Omega = 0$; (+) $\Omega = 1/2$; (○) $\Omega = 1/4$; (□) $\Omega = 1/8$; and (△) $\Omega = 1/16$. The dashed lines are shown to guide the eye. The horizontal solid lines correspond to the thermal asymptote gradients of Eqs. (5.28) and (5.29). The vertical dotted lines correspond to Eq. (11.2).

distribution spans a fractional quantum resonance feature. Quantitatively, the thermalisation width w_{th} is defined by Eq. (11.2), and as indicated by the vertical dotted lines in Fig. 11.4 it accurately predicts the temperature at which the fractional quantum resonant dynamics saturates in the thermal limit.

11.4 Conclusions

We demonstrated with Fig. 11.1 that for a low temperature gas, the energy of the ensemble, quantified by $\langle\hat{p}^2\rangle_n$, provides a signature for quantum resonance in the δ-kicked accelerator. For sufficiently high temperatures, the linear growth of $\langle\hat{p}^2\rangle_n$ is not resolvable. We demonstrated that with finite temperatures, $\langle\hat{p}^4\rangle_n$ is resolvable. However, since $\langle\hat{p}^4\rangle_n$ is dependent upon $\langle\hat{p}^2\rangle_n$, we found that it is informative to investigate the mutually independent momentum cumulants.

In Figs. 11.2 and 11.3, we presented the cumulant evolution comparing their depen-

dence upon w and Ω. In Fig. 11.2, we plotted $\Delta\langle\langle\hat{p}^2\rangle\rangle_n$ in the ultracold and thermal regimes, as well as for intermediate temperatures. We observed the linear trend for the thermal regime, which is consistent with the result expected for a classically chaotic δ-kicked rotor. However, we also observe fluctuations for this thermal case which are dependent upon the value of Ω. These fluctuations demonstrate the inherent quantum mechanical nature of the system, which we exploit in the next chapter to quantify the Ω dependence.

With Fig. 11.3, we demonstrated the merit of using $\langle\langle\hat{p}^4\rangle\rangle_n^{1/3}$ to quantify the transition of a finite-temperature gas from an ultracold to a thermal regime. We have determined that a narrow Gaussian momentum distribution initially exhibits dynamics compatible with the ultracold regime, and adopts the thermal regime following a sufficient number of laser pulses. We find the transition between these two extremes to be independent of the value of Ω, as indicated by comparing Eq. (11.1) to our numerical data. The dependence upon w for this transition was investigated using linear regression analysis, with the gradient of $\langle\langle\hat{p}^4\rangle\rangle_n^{1/3}$ plotted in Fig. 11.4. The thermalisation temperature was found to be dependent upon Ω, as given by Eq. (11.2).

Movies showing the time evolution of the observables are available to download at:

`http://massey.dur.ac.uk/ms/movies.html`

Chapter 12

Gravitational sensitivity

12.1 Overview

In this chapter, we assess the sensitivity of the fractional quantum resonances to Ω. In Section 12.2, we consider the simplest case possible by taking the ultracold limit, analysing the time evolution of a single momentum eigenstate. It is constructive to learn more about quantum resonance widths to develop our understanding of the δ-kicked accelerator.

An application to rotation measurement has been performed by the Prentiss group at Harvard [144–147]. Analysing decoherence times of an atom interferometer perturbed by a δ-kicked rotor potential, the quantum resonance width was found to be given by

$$\delta\Omega_R \propto \frac{1}{ns\ell}. \tag{12.1}$$

In this chapter, we demonstrate that this experimental result is consistent with our model.

We follow the procedure from Chapter 9 to investigate the gravity dependence of the δ-kicked accelerator. We propose methods to quantify the width of the quantum resonant features. In Section 12.3, we present preliminary results for a finite temperature gas, and discuss the feasibility of using the δ-kicked accelerator for the precision measurement of g.

12.2 Quantum resonant effects in the ultracold limit

In Fig. 12.1 we study the evolution of the second-order momentum moment over a range of Ω from 0 to 2, for both $T = T_T/2$ ($\ell = 1$) and $T = T_T$ ($\ell = 2$). The initial condition

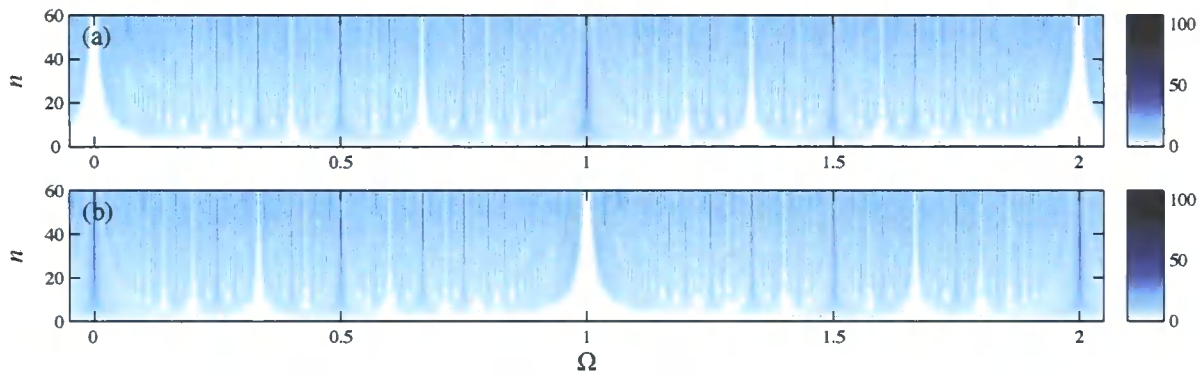

Figure 12.1: $\langle\langle\hat{p}^2\rangle\rangle_n^{1/2}$ in units of $\hbar K$ for a δ-kicked accelerator initially in a zero-momentum eigenstate. Parameters are $\mathcal{N} = 1$ ($w = 0$), $\phi_d = 0.8\pi$, and (a) $T = T_T/2$ ($\ell = 1$); and (b) $T = T_T$ ($\ell = 2$).

in every case is a $\beta = 0$ quasimomentum eigenstate. We observe a rich structure of gravitationally sensitive phenomena, with the dark regions showing the fractional quantum resonance features, and the light regions showing the fractional quantum antiresonance effects. First-order quantum resonance effects, as studied in Chapter 10, are observed for integer Ω values.

In the ultracold limit, transformed Floquet operator (4.12) reduces to

$$\tilde{F}_n(\beta = 0) = \exp\left(-i\pi[\ell + \Omega - 2n\Omega]\hat{k}\right) \exp\left(i\phi_d \cos(K\hat{z})\right). \tag{12.2}$$

From the simplified free evolution operator term, we deduce that integer changes in the value of Ω can be equivalently described by modifying the number of half-Talbot times making up a kick period T. This is verified from the numerical results presented in Fig. 12.1, with the observation that on changing from $\ell = 1$ to $\ell = 2$, the Ω dependence of the various quantum resonant and quantum antiresonant features is transposed by one. We may define an effective kick period $T = \ell' T_T/2$ for an integer formed from $\ell' = \ell + \Omega$, for which the quantum resonant results are observed as predicted.

12.2.1 Quantifying the quantum resonant features

In Fig. 12.2, we examine quantum resonant effects from Fig. 12.1(b), for which $\ell = 2$. The vicinity of the quantum resonant effects is shown in further detail in Fig. 12.3. We have found that in addition to the quantum resonance and quantum antiresonance features themselves, there are other interesting features which we highlight in this section by

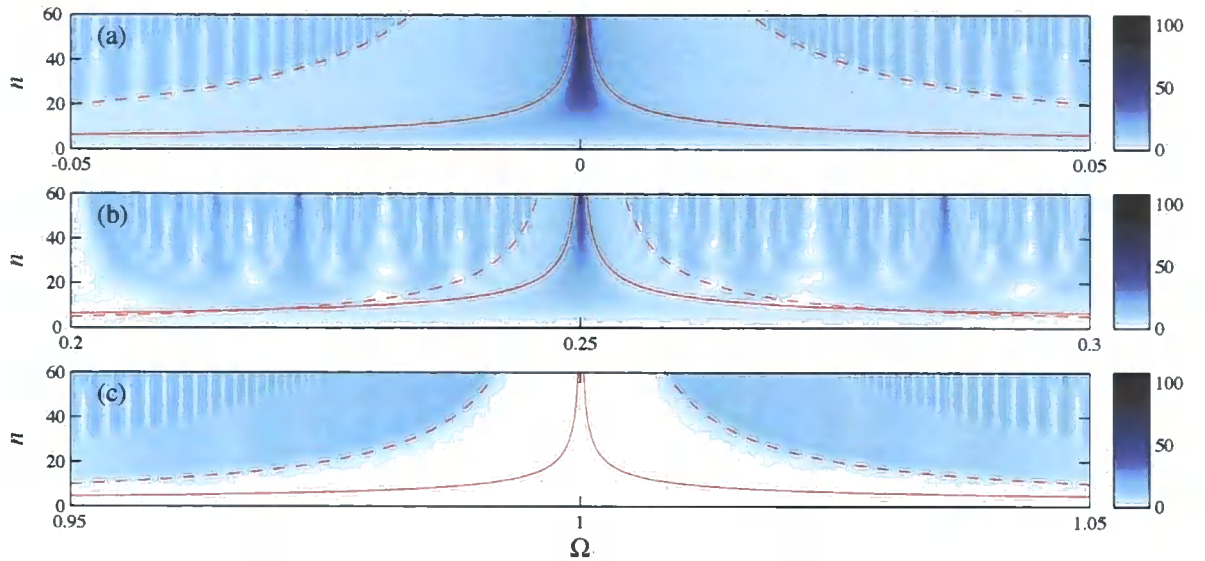

Figure 12.2: $\langle\langle\hat{p}^2\rangle\rangle_n^{1/2}$ in units of $\hbar K$ for a δ-kicked accelerator initially in a zero-momentum eigenstate. Parameters are $\mathcal{N} = 1$ ($w = 0$), $\phi_d = 0.8\pi$, and $T = T_T$ ($\ell = 2$). The gravity dependence is shown in the vicinity of (a) $\Omega = 0$ (Quantum resonance, with $s = 1$); (b) $\Omega = 1/4$ (Fourth-order quantum resonance, with $s = 4$); and (c) $\Omega = 1$ (Quantum antiresonance). The dashed lines correspond to Eq. (12.3) in (a) and (b), and Eq. (12.4) in (c) The solid lines correspond to Eq. (12.5) in (a) and (b), and Eq. (12.6) in (c).

postulating equations to describe loci, as was done in Chapter 9. In Section 12.3, we describe the conditions for which these features are observed for a finite temperature gas.

In Figs. 12.2 and 12.3, we observe the Ω dependence in the vicinity of the fractional quantum resonance feature by evaluating the difference $\bar{\Omega} = \Omega - \Omega_m^{\mathrm{FR}}$. In Chapter 9, we showed with Eq. (9.12) that an Nth order quantum antiresonance occurs at $n = N$ kicks, from which we deduced that reconstruction loci are inversely proportional to the number of kicks.

Quantum resonance loci

In Figs. 12.2(a) and 12.3(a), we show the gravity dependence in the vicinity of the first-order quantum resonance where $\Omega = 0$. A fourth-order quantum resonance is shown in Figs. 12.2(b) and 12.3(b), in the vicinity of $\Omega = 1/4$. We see from the behaviour of $\langle\langle\hat{p}^2\rangle\rangle_n^{1/2}$ that for $\Omega = 1/N$, there is a step up in energy after a number of kicks that is an integer multiple of N. The first occurrence of the onset of the Nth order quantum resonance is denoted by the dashed lines, which may be used to quantify the width of the sth order quantum resonance feature, as was done in Chapter 9. The observation of the

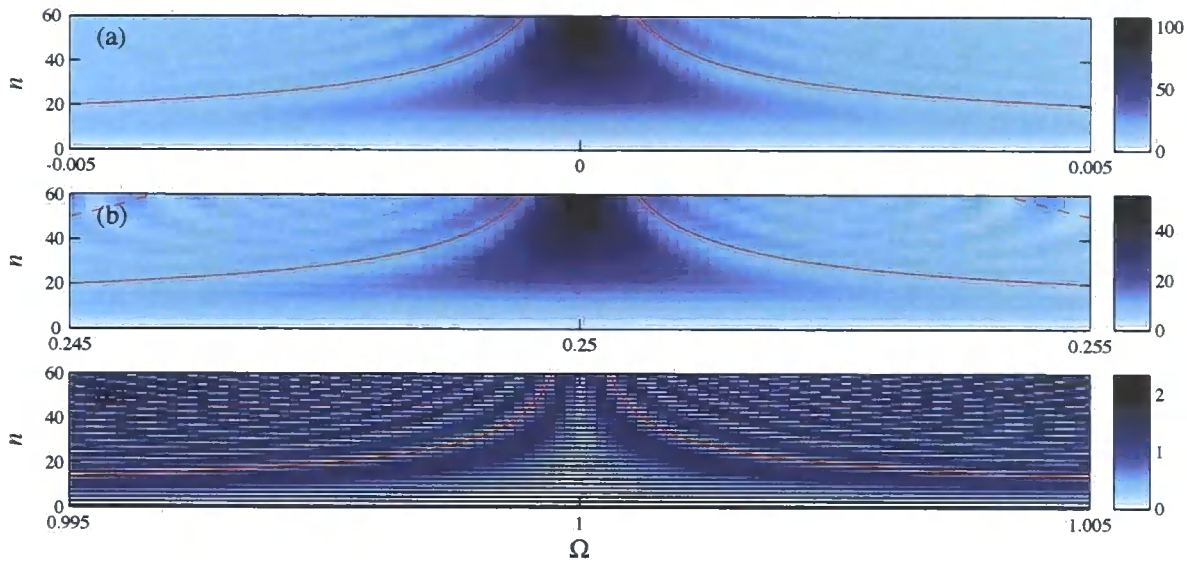

Figure 12.3: Zoom of the quantum resonant features, with the same parameters as shown in Fig. 12.2. Note that the colour scale is different in each of the subplots, to emphasise the high-order quantum antiresonance features. The solid lines correspond to the asymptotes defined by Eq. (12.5) in (a) and (b), and Eq. (12.6) in (c).

dramatic step up in energy is consistent with the Nth order fractional quantum resonant effects observed in Fig. 11.2, for which the grey lines correspond to kick numbers are an integer multiple of the value of N.

Analogous to the loci described by Eq. (9.12), we expect loci that are inversely proportional to n. Fitting the loci by eye, we observe from the dashed lines in Figs. 12.2(a) and 12.2(b) that for $\Omega_m^{\mathrm{FR}} = r/s$,

$$\bar{\Omega}_R(s) = \pm\frac{1}{ns}, \tag{12.3}$$

which is found to be dependent upon the value of Ω_m^{FR} since s appears in this expression. The result given by Eq. (12.3) for the δ-kicked accelerator which incorporates gravity, is consistent with Eq. (12.1) for the δ-kicked rotor evaluated by the Prentiss group.

In the vicinity of a quantum antiresonance feature, we predicted with Eq. (9.14) that the number of loci was double the number in the vicinity of a quantum antiresonance feature. This was confirmed by comparison with the numerical results in Figs. 9.2 and 9.3, and explained by the observation of Nth order quantum antiresonances of both even and odd parity. We found a similar result with Fig. 12.2(c), for which we observed with

$\Omega = 1$, for which $s = 1$, that fitting the loci by eye that

$$\bar{\Omega}_A = \frac{\bar{\Omega}_R(s=1)}{2} = \pm\frac{1}{2n}. \tag{12.4}$$

Quantum antiresonance loci

In Fig. 12.3, we observe interesting behaviour of $\langle\langle \hat{p}^2 \rangle\rangle_n^{1/2}$ in the vicinity of Ω_m^{FR}. We attribute this to the occurrence of high order quantum antiresonance features, which are resolvable at low values of Ω_m^{FR}. This appears consistent to Fig. 11.2, for which fluctuations in energy were observed at intermediate kick numbers.

We postulated that the loci satisfy a $1/n^2$ relationship, denoted by the solid lines in Figs. 12.2 and 12.3, which we fit by eye to the numerical data. In the vicinity of an sth order quantum resonance feature, we found that

$$\bar{\Omega}'_R = \pm\frac{2}{n^2}, \tag{12.5}$$

which is found to be independent of the value of Ω_m^{FR} since s does not appear in this expression. In the vicinity of a quantum antiresonance, we note that the expression for the loci differs by a factor of two, such that

$$\bar{\Omega}'_A = \frac{\bar{\Omega}'_R}{2} = \pm\frac{1}{n^2}. \tag{12.6}$$

12.2.2 Quantifying the width of a fractional quantum resonance feature

Following the procedure from Chapter 9, we refer to the solid lines described by Eq. (12.5) as reconstruction loci. We define the quantum resonance width in terms of the separation of the lines adjacent to a fractional quantum resonance feature, which is given by

$$\delta\Omega' \sim \frac{2}{n^2}. \tag{12.7}$$

This measure of the quantum resonance width is an improvement to the fitted expression for the δ-kicked accelerator given by Eq. (12.3), and the angular acceleration result given by Eq. (12.1).

We conclude that is possible to quantify the width of a fractional quantum resonance feature, with Eq. (12.7) providing an upper bound to the gravitational sensitivity of the

δ-kicked accelerator. In Section 12.3, we discuss the possibility for using these asymptotes to perform a precision measurement of the value of Ω.

12.3 Gravity measurement with a finite temperature gas

Inertial sensitivity is of importance for mapping the variations in the Earth's gravitational field, with a recent high profile example being the launch of the GOCE satellite by the European Space Agency, which is designed to map the gravitational pull to an accuracy of 10^{-5} ms^{-2} [148]. Mappping the variation in gravitational field, the measurement of mass distribution has applications to prospecting for oil as well as the study of geological hazards. The sensitivity of the satellite is expected to enable the mapping of ocean currents, which circulate heat around the planet, and will be used for the development of climate change models.

In Fig. 12.4, we show the gravity dependence in the vicinity of a first-order quantum resonance, as seen in Fig. 12.2(a). However, this time a finite temperature gas is considered, with $w = 1/128$ in Fig. 12.4(a), and $w = 1/1024$ in Fig. 12.4(b).

We find that the asymptote given by Eq. (12.3) is resolvable in both figures. In contrast, we find that the asymptote given by Eq. (12.5) is only resolvable in Fig. 12.4(b). We also see finer detail to the feature used to construct asymptote Eq. (12.3). These effects are due to the lower temperature plot showing greater resolution of the higher-order antiresonance features.

In Fig. 12.5, we examine the gravity dependence in finer detail to investigate the substructure of the quantum resonance feature. Notice that for the higher temperature gas in Fig. 12.5(a), the quantum resonance is broad, meaning that the high-order quantum antiresonances cannot be resolved. In contrast, in Fig. 12.5(b), we plot asymptote (12.5), which may be used to measure the value of Ω.

12.3.1 Prospect for precision measurement

The sensitivity to gravity of the quantum resonance features is determined from the definition given by Eq. (4.13),

$$\Omega \equiv \frac{2\pi\ell^2(g - a_\phi)M^2}{\hbar^2 K^3}. \tag{12.8}$$

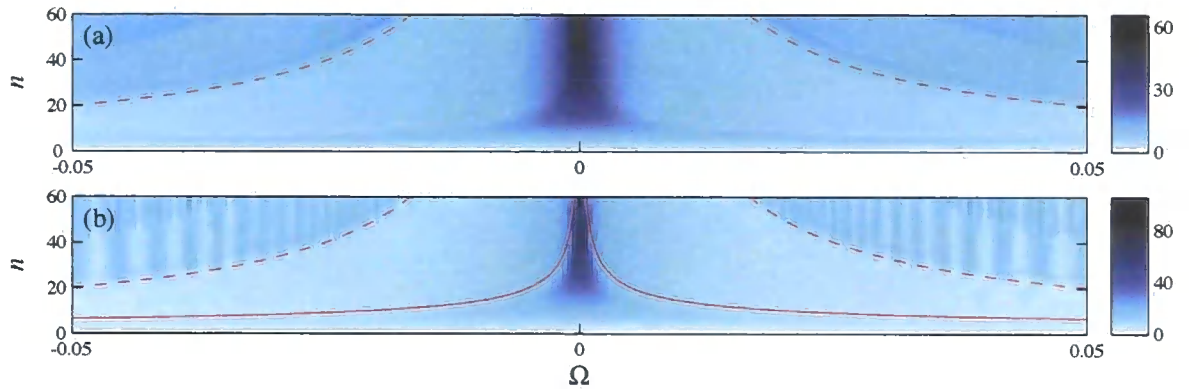

Figure 12.4: $\langle\langle\hat{p}^2\rangle\rangle_n^{1/2}$ in units of $\hbar K$ for a δ-kicked accelerator in a low temperature gas. Parameters are $\mathcal{N} = 1000$, $\phi_d = 0.8\pi$, and $T = T_T$ ($\ell = 2$). The gravity dependence is shown in the vicinity of $\Omega = 0$ (Quantum resonance), with the initial Gaussian distribution of width (a) $w = 1/128$; and (b) $w = 1/1024$. The dashed lines correspond to Eq. (12.3), and the solid line in (b) corresponds to Eq. (12.5).

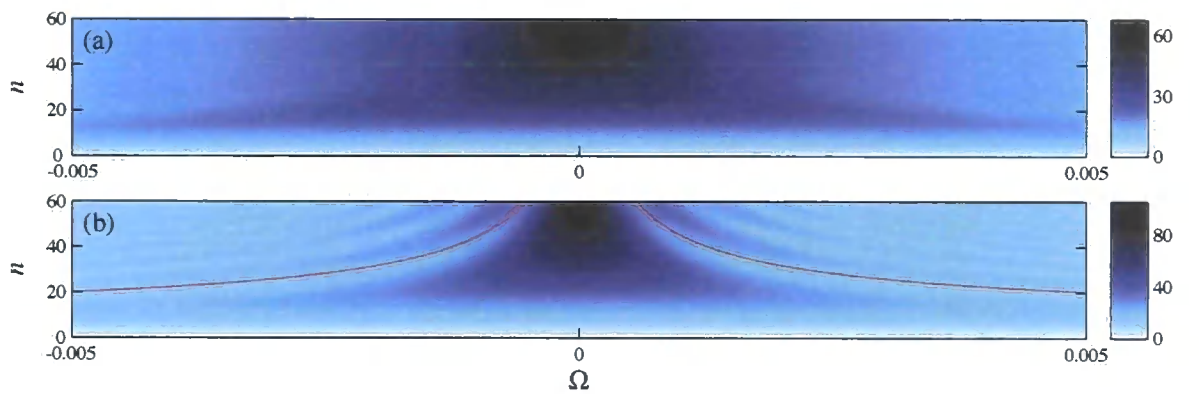

Figure 12.5: Zoom of the quantum resonant feature in the vicinity of $\Omega = 0$, with the same parameters as shown in Fig. 12.4. The solid line in (b) corresponds to Eq. (12.5).

Differentiating the gravity parameter with respect to g, we obtain

$$\frac{d\Omega}{dg} = \frac{2\pi\ell^2 M^2}{\hbar^2 K^3}, \tag{12.9}$$

and rearranging, we obtain a measure of the quantum resonance width in terms of the local gravitational acceleration to be

$$\delta g = \frac{\hbar^2 K^3}{2\pi\ell^2 M^2}\delta\Omega'. \tag{12.10}$$

Substituting Eq. (12.7) and setting $\ell = 2$, we obtain the quantum resonance width

$$\delta g = \frac{\hbar^2 K^3}{4\pi M^2} \frac{1}{n^2}. \tag{12.11}$$

In practice, the quantum resonant effects could be examined with finer resolution, since we anticipate that fitting experimental data to a theoretical scan across Ω, which would enable the quantum resonance width $\delta\Omega$ to be further reduced. This means that this asymptote provides an upper bound to the systematic error.

Experimental parameters are provide in Table 12.1. We have calculated that to obtain a statistical error of $\delta g < 10^{-6}$ ms^{-2}, a large number of kicks are required. The experiment must remain stable for the duration of the pulses. If quantum antiresonances are used to perform a precision measurement, then this measurement could be performed on a length scale comparable with the size of the atom cloud. Note however, that the cloud will still be falling under the influence of gravity since we have transformed to a frame moving with the centre of mass of the atom cloud.

Recent gravimetry experiments have achieved an uncertainty on order of 1 part in 10^4 using ^{87}Rb Bose-Einstein condensates, periodically pulsed with standing waves [149]. Our model confirms the feasibility for measurement of gravity using the δ-kicked accelerator. This is in comparison with interferometric techniques, for which precision has been measured to 1 part in 10^{10} [150, 151].

Experiment	Oxford, UK	Austin, Texas, USA
Atomic species	^{133}Cs	^{23}Na
Mass	133 a.m.u. $= 2.21 \times 10^{-25}$ kg	23 a.m.u. $= 3.82 \times 10^{-26}$ kg
Atomic transition	D1: $6^2S_{1/2}$(F=4) $\rightarrow$ $6^2P_{1/2}$(F=3)	$3S_{1/2}$(F=2) $\rightarrow$ $3P_{3/2}$(F=3)
Detuning	$\sim$30 GHz	$\sim$20 MHz
Wavelength λ	895 nm	589 nm
Wavenumber K	1.40×10^7 m^{-1}	2.13×10^7 m^{-1}
Talbot time T_T	133 μs	10 μs
$n(\delta g = 10^{-6}$ ms$^{-2})$	7,000	80,000
Experiment duration t	1 s	0.8 s
Reference	[107]	[108]

Table 12.1: Comparison of experimental parameters for the atom-optical δ-kicked accelerator. Using Eq. (12.10), we evaluate the time evolution of the quantum resonance width, to determine the number of kicks required to reduce the upper bound on the systematic error to $\delta g < 10^{-6}$ ms^{-2}.

In comparison to an experiment at Innsbruck [118, 119], it has been shown that it is possible to study Bloch oscillations in Bose-Einstein condensates for over twenty thousand periods, allowing integration times in excess of 10 s.

12.4 Conclusions

The quantum resonance width decreases at low temperatures and high kick numbers. Therefore, in order to perform a precision measurement, the gas must be ultracold and the experiment must be stable at long integration times.

We have developed a method to quantify the width of the quantum resonance feature at $\Omega = 0$, with our model building upon a proof of principle experiment performed in Oxford [107]. Our theory does not consider systematic errors or experimental errors. We have provided a theoretical upper bound to the gravitational sensitivity of the δ-kicked accelerator.

Chapter 13

Thesis conclusions

We have investigated the δ-kicked accelerator in the context of atomic physics, assessing the dependence of the time evolution upon pulse period T, gravity parameter Ω, and the initial temperature which is parametrised by w which indicates the width of the initial momentum distribution. We verified that by tuning to specific values of the system parameters, quantum resonant phenomena are observed, which were quantified by extracting momentum moments and momentum cumulants from the momentum distribution data.

We observed quantum resonance and quantum antiresonance of the δ-kicked rotor by setting the pulse period to an integer multiple of the half-Talbot time. We found that for rational values of the gravity parameter, such that $\Omega = r/s$, the δ-kicked accelerator exhibits fractional quantum resonant features of order s.

Signatures of quantum resonance are presented in Table 7.1, with quantum antiresonance categorised by recurrence of the initial momentum state. Above a thermalisation temperature, the system adopts the thermal regime, as summarised in Table 8.1.

In Chapter 9, we observed the time evolution of individual momentum eigenstates, from which we established the quasimomentum dependence for specific values of T and Ω. We studied the temperature dependence of the δ-kicked rotor in Chapter 10, and discovered conditions under which the dynamics undergoes a transition from the ultracold to the thermal regime. In Chapter 11, we studied high-order quantum resonant features observed for fractional values of Ω for the δ-kicked accelerator. We established a thermalisation temperature by analysing the fourth-order momentum cumulant using linear regression analysis. In Chapter 12, we investigated the dependence of the dynamics upon Ω, and quantified the width of the quantum resonance features, which confirmed the feasibility for precision measurement of local gravitational acceleration.

Appendix A

Operator identities

A.1 Overview

In this appendix, we provide operator identities which are used to derive analytic results presented in the main body of the thesis text.

A.2 The displacement operator

For operators $\hat{A}$ and $\hat{B}$ and parameter τ [152],

$$e^{\tau\hat{A}}\hat{B}e^{-\tau\hat{A}} = \hat{B} + \tau[\hat{A},\hat{B}] + \frac{\tau^2}{2!}[\hat{A},[\hat{A},\hat{B}]] + \frac{\tau^3}{3!}[\hat{A},[\hat{A},[\hat{A},\hat{B}]]] + \cdots . \tag{A.1}$$

For a commutation relation $[\hat{A},\hat{B}] = c$, where c is a scalar, the higher order terms are zero, and so

$$e^{\tau\hat{A}}\hat{B}e^{-\tau\hat{A}} = \hat{B} + c\tau. \tag{A.2}$$

Furthermore, for any function $f(\hat{B})$ that can be Taylor expanded,

$$e^{\tau\hat{A}}f(\hat{B})e^{-\tau\hat{A}} = f(\hat{B} + c\tau). \tag{A.3}$$

The displacement of $\hat{B}$ by a scalar is used in this thesis to simplify the operators describing the time evolution of δ-kicked systems.

Substitution for Eq. (3.29)

Setting $\hat{A} = \hat{J}'$ and $\hat{B} = \hat{\theta}$, with the commutation relation $[\hat{J}', \hat{\theta}] = -i\hbar$, we see from (A.3) that

$$e^{-i\hat{J}'/2} \exp\left(i\phi_d \cos\hat{\theta}\right) e^{i\hat{J}'/2} = \exp\left(i\phi_d \cos(\hat{\theta} - \pi\ell)\right). \tag{A.4}$$

This relationship is substituted into Section 3.4.3 to introduce quantum antiresonance for the case of the quantum δ-kicked rotor.

Substitution for Eq. (A.15)

Setting $\hat{A} = \rho_1\tau\hat{p}^2 + \rho_2\tau^2\hat{p} + \rho_3\tau^3$ and $\hat{B} = \gamma\hat{z}$, we note that since $[\hat{p}^2, \hat{z}] = -2i\hbar\hat{p}$ commutes with $\hat{A}$, we may make use of Eq. (A.3) to obtain

$$e^{\rho_1\tau\hat{p}^2+\rho_2\tau^2\hat{p}+\rho_3\tau^3}\gamma\hat{z}e^{-(\rho_1\tau\hat{p}^2+\rho_2\tau^2\hat{p}+\rho_3\tau^3)} = \gamma\hat{z} - i\hbar\gamma\left(2\rho_1\tau\hat{p} + \rho_2\tau^2\right). \tag{A.5}$$

This is used in Section A.5 to factorise the free-evolution operator.

A.3 Unitary transformations of the Hamiltonian

A unitary operator acting on a wavefunction can be expressed by

$$|\tilde{\Psi}\rangle = \hat{U}|\Psi\rangle. \tag{A.6}$$

Differentiating using the product rule,

$$i\hbar\frac{d|\tilde{\Psi}\rangle}{dt} = i\hbar\frac{d\hat{U}}{dt}|\Psi\rangle + i\hbar\hat{U}\frac{d|\Psi\rangle}{dt} = \left(i\hbar\frac{d\hat{U}}{dt}\hat{U}^\dagger + \hat{U}\hat{H}\hat{U}^\dagger\right)|\tilde{\Psi}\rangle. \tag{A.7}$$

Comparing this with the time-dependent Schrödinger equation (3.7), under a unitary operation, the Hamiltonian thus satisfies the transformation relation,

$$\tilde{H} = i\hbar\frac{d\hat{U}}{dt}\hat{U}^\dagger + \hat{U}\hat{H}\hat{U}^\dagger. \tag{A.8}$$

We make use of this identity in Appendix B to relate $\hat{H}_{\text{2level}}$ to the form of $\hat{H}_{\delta\text{ka}}$. Identity (A.8) is also used in Section 4.4.1 together with displacement operator (A.3) to transform the δ-kicked accelerator Hamiltonian to the reference frame accelerating with the centre

of mass of the cloud of falling atoms.

A.4 Basis transformations

In this section, we derive expressions for basis transformations following a procedure by S. A. Gardiner [153]. Consider a basis formed by two orthogonal states, $|\psi\rangle$ and $|\phi\rangle$. The unitary operator $\hat{U}_1 = \exp(\xi|\psi\rangle\langle\psi|)$ with parameter ξ, satisfies the identities [153]

$$\begin{aligned} \hat{U}_1|\phi\rangle &= |\phi\rangle \\ \langle\phi|\hat{U}_1 &= \langle\phi|. \end{aligned} \tag{A.9}$$

In comparison, the case where $|\phi\rangle = |\psi\rangle$ [153]

$$\begin{aligned} \hat{U}_1|\psi\rangle &= e^{\xi}|\psi\rangle \\ \langle\psi|\hat{U}_1 &= \langle\psi|e^{\xi}. \end{aligned} \tag{A.10}$$

Identities (A.9) and (A.10) are combined to give

$$\begin{aligned} \hat{U}_1|\phi\rangle\langle\phi|\hat{U}_1^\dagger &= |\phi\rangle\langle\phi| \\ \hat{U}_1|\psi\rangle\langle\psi|\hat{U}_1^\dagger &= |\psi\rangle\langle\psi| \\ \hat{U}_1|\psi\rangle\langle\phi|\hat{U}_1^\dagger &= e^{\xi}|\psi\rangle\langle\phi| \\ \hat{U}_1|\phi\rangle\langle\psi|\hat{U}_1^\dagger &= e^{-\xi}|\phi\rangle\langle\psi|, \end{aligned} \tag{A.11}$$

where the Hermitian conjugate is defined as the conjugate transpose, denoted $\hat{U}_1^\dagger = (\hat{U}_1^*)^T$.

Generalising further, if

$$\hat{U}_2 = \exp(\xi_1|\psi\rangle\langle\psi| + \xi_2|\phi\rangle\langle\phi|), \tag{A.12}$$

then

$$\begin{aligned} \hat{U}_2|\phi\rangle\langle\phi|\hat{U}_2^\dagger &= |\phi\rangle\langle\phi| \\ \hat{U}_2|\psi\rangle\langle\psi|\hat{U}_2^\dagger &= |\psi\rangle\langle\psi| \\ \hat{U}_2|\psi\rangle\langle\phi|\hat{U}_2^\dagger &= e^{\xi_1-\xi_2}|\psi\rangle\langle\phi| \\ \hat{U}_2|\phi\rangle\langle\psi|\hat{U}_2^\dagger &= e^{\xi_2-\xi_1}|\phi\rangle\langle\psi|. \end{aligned} \tag{A.13}$$

Identities (A.13) are used in Appendix B to transform the Hamiltonian and in Appendix

C to transform the time-evolution operator.

A.5 Factorisation of the free-evolution operator

In this section, we present a derivation from Publication [3], which we use to factorise Floquet operator (C.1). It is convenient to separate the terms that depend on $\hat{z}$ from those that depend on $\hat{p}$. Consider a general operator of the form

$$\hat{O}(\tau) = \exp\left(\rho_1 \tau \hat{p}^2 + \rho_2 \tau^2 \hat{p} + \rho_3 \tau^3\right) \exp(\gamma \tau \hat{z}). \tag{A.14}$$

Taking the partial derivative of $\hat{O}$ with respect to τ gives

$$\frac{\partial \hat{O}(\tau)}{\partial \tau} = \left[e^{\rho_1 \tau \hat{p}^2 + \rho_2 \tau^2 \hat{p} + \rho_3 \tau^3} \gamma \hat{z} e^{-(\rho_1 \tau \hat{p}^2 + \rho_2 \tau^2 \hat{p} + \rho_3 \tau^3)} + \left(\rho_1 \hat{p}^2 + 2\rho_2 \tau \hat{p} + 3\rho_3 \tau^2\right)\right] \hat{O}(\tau). \tag{A.15}$$

Making use of the identity (A.5), this simplifies to

$$\frac{\partial \hat{O}(\tau)}{\partial \tau} = \left[\rho_1 \hat{p}^2 + 2\tau\left(\rho_2 - i\hbar\rho_1\gamma\right)\hat{p} + \gamma\hat{z} + \tau^2\left(3\rho_3 - i\hbar\rho_2\gamma\right)\right] \hat{O}(\tau). \tag{A.16}$$

Choosing ρ_2 and ρ_3 such that terms proportional to τ and τ^2 vanish, i.e., $\rho_2 = i\hbar\rho_1\gamma$, and subsequently $\rho_3 = -\hbar^2\rho_1\gamma^2/3$, Eq. (A.16) reduces to

$$\frac{\partial \hat{O}(\tau)}{\partial \tau} = (\rho_1 \hat{p}^2 + +\gamma\hat{z})\hat{O}(\tau). \tag{A.17}$$

Noting from Eq. (A.14) that $\hat{O}(0) = 1$, Eq. (A.17) can be integrated to give

$$\hat{O}(\tau) = \exp(\rho_1 \tau \hat{p}^2 + \gamma\tau\hat{z}). \tag{A.18}$$

Hence the result

$$\exp\left(\rho_1 \tau \hat{p}^2 + \gamma\tau\hat{z}\right) = \exp\left(\rho_1 \tau \hat{p}^2 + i\hbar\rho_1\gamma\tau^2\hat{p} - \hbar^2\rho_1\gamma^2\tau^3/3\right)\exp\left(\gamma\tau\hat{z}\right). \tag{A.19}$$

Setting $\rho_1 = -i/2M\hbar$, $\gamma = -iMa/\hbar$, and $\tau = T$, reveals

$$\exp\left(-\frac{i}{\hbar}\left[\frac{\hat{p}^2}{2M} + Ma\hat{z}\right]T\right) = \exp\left(-\frac{i}{\hbar}\left[\frac{\hat{p}^2}{2M} + \frac{\hat{p}aT}{2}\right]T\right) \times \exp\left(-\frac{iMa\hat{z}T}{\hbar}\right)\exp\left(-\frac{iMa^2T^3}{6\hbar}\right). \tag{A.20}$$

This is the factorised form of the free-evolution component of the Floquet operator (C.1).

Appendix B

The atom-optical Hamiltonian

B.1 Overview

We start with the Hamiltonian for the atom-optical configuration,

$$\begin{aligned}\hat{H}_{\text{2level}} =& \frac{1}{2}\hbar\omega_0\left(|e\rangle\langle e| - |g\rangle\langle g|\right) + \frac{\hat{p}^2}{2M} + Mg\hat{z} \\ &+ \frac{1}{2}\hbar\Omega_{R1}\left[e^{i(k_L\hat{z}-\omega_L t+\phi_1)}|e\rangle\langle g| + e^{-i(k_L\hat{z}-\omega_L t+\phi_1)}|g\rangle\langle e|\right] \\ &+ \frac{1}{2}\hbar\Omega_{R2}\left[e^{-i(k_L\hat{z}+\omega_L t-\phi_2)}|e\rangle\langle g| + e^{i(k_L\hat{z}+\omega_L t-\phi_2)}|g\rangle\langle e|\right],\end{aligned} \tag{B.1}$$

which was introduced in Section 4.2.3. In this appendix, we demonstrate that by imposing certain conditions, that it is possible to reduce the two-level atom model to the form of the quantum δ-kicked accelerator. We explain in detail a derivation presented in Publication [3] which generalised a derivation from Publication [1] by incorporating gravitational effects.

By deriving $\hat{H}_{\delta\text{ka}}$, we have demonstrate that the quantum resonant effects introduced in Chapter 3 may be experimentally investigated using the atom-optical configuration described by Hamiltonian (B.1). We discuss the concequences of this result in Chapter 4, and go on to derive the kick-to-kick time evolution operator in Appendix C.

B.2 Trig Rearrangement

Setting the Rabi frequencies equal, such that $\Omega_{R1} = \Omega_{R2} = \Omega_R/2$, we focus on the terms involving $|e\rangle\langle g|$:

$$\begin{aligned}&\hbar\frac{\Omega_R}{4}e^{i(k_L\hat{z}-\omega_L t+\phi_1)} + \hbar\frac{\Omega_R}{4}e^{-i(k_L\hat{z}+\omega_L t-\phi_2)}\\ &= \frac{1}{4}\hbar\Omega_R e^{-i(\omega_L t-\phi_1/2-\phi_2/2)}[e^{i(k_L\hat{z}+\phi_1/2-\phi_2/2)} + e^{-i(k_L\hat{z}+\phi_1/2-\phi_2/2)}].\end{aligned} \tag{B.2}$$

Using $2\cos x = e^{ix} - e^{-ix}$, and defining $\phi_r = \phi_1 - \phi_2$ and $\phi_s = (\phi_1 + \phi_2)/2$, the $|e\rangle\langle g|$ factor simplifies to

$$\frac{1}{2}\hbar\Omega_R\cos(k_L\hat{z} + \phi_r/2)e^{-i(\omega_L t-\phi_s)}. \tag{B.3}$$

The complex conjugate of this factor is obtained for the Hermitian conjugate term, $|g\rangle\langle e|$. Therefore, Hamiltonian (B.1) is factorised to

$$\begin{aligned}\hat{H}_{2\text{level}} =&\frac{1}{2}\hbar\omega_0(|e\rangle\langle e| - |g\rangle\langle g|) + \frac{\hat{p}^2}{2M} + Mg\hat{z}\\ &+ \frac{1}{2}\hbar\Omega_R\cos(k_L\hat{z} + \phi_r/2)\left[e^{-i(\omega_L t-\phi_s)}|e\rangle\langle g| + \text{H.c.}\right],\end{aligned} \tag{B.4}$$

where H.c. denotes the Hermitian conjugate of the other term within the same set of brackets, which is defined by taking the conjugate transpose of the relevant term.

B.3 Removal of $|g\rangle\langle g|$ term

To carry out the unitary transformation defined by

$$\hat{U}_3 = \exp(i[\omega_L|e\rangle\langle e| - \omega_0(|e\rangle\langle e| + |g\rangle\langle g|)/2]t), \tag{B.5}$$

we carry out the procedure introduced in Section A.4. Setting $|\phi\rangle = |e\rangle$ and $|\psi\rangle = |g\rangle$, with $\xi_1 = it(\omega_L - \omega_0)$ and $\xi_2 = -it\omega_0/2$. Applying this to (B.4), we obtain

$$\begin{aligned}\hat{U}_3\hat{H}_{2\text{level}}\hat{U}_3^\dagger =&\frac{1}{2}\hbar\omega_0(|e\rangle\langle e| - |g\rangle\langle g|) + \frac{\hat{p}^2}{2M} + Mg\hat{z}\\ &+ \frac{1}{2}\hbar\Omega_R\cos(k_L\hat{z} + \phi_r/2)\left[e^{-i(\omega_L t-\phi_s)}e^{it(\omega_L-\omega_0/2)}|e\rangle\langle g| + \text{H.c.}\right].\end{aligned} \tag{B.6}$$

In addition, we find

$$i\hbar\frac{d\hat{U}_3}{dt}\hat{U}_3^\dagger = -\hbar(\omega_L - \omega_0/2)|e\rangle\langle e| + \hbar(\omega_0/2)|g\rangle\langle g|. \tag{B.7}$$

Substituting these into (A.8), the Hamiltonian transforms to,

$$\begin{aligned}\hat{H}'_{\text{2level}} =&\hbar\Delta|e\rangle\langle e| + \frac{\hat{p}^2}{2M} + Mg\hat{z} \\ &+ \frac{1}{2}\hbar\Omega_R\cos(k_L\hat{z} + \phi_r/2)\left[e^{i\phi_s}|e\rangle\langle g| + \text{H.c.}\right],\end{aligned} \tag{B.8}$$

where we have defined the detuning $\Delta \equiv \omega_0 - \omega_L$. Therefore, the Hamiltonian has been simplified by transforming to the frame in which the $|g\rangle\langle g|$ term is eliminated.

B.4 Transformation to accelerating frame

We now transform to the frame accelerating with the walking wave, with the unitary transformation,

$$\hat{U}_4 = \exp\left(\frac{i}{\hbar}Ma_\phi\hat{z}t\right)\exp\left(-\frac{i}{\hbar}\frac{a_\phi\hat{p}t^2}{2}\right)\exp\left(\frac{i}{\hbar}\chi(t)\right). \tag{B.9}$$

We find that

$$i\hbar\frac{d\hat{U}_4}{dt}\hat{U}_4^\dagger = -\left[Ma_\phi\hat{z} - a_\phi\hat{p}t + \frac{d\chi(t)}{dt}\right]. \tag{B.10}$$

We make use of the displacement operator (A.3) by noting that $[\hat{z},\hat{p}] = i\hbar$ is a scalar. Thus $\hat{U}_4\hat{z}\hat{U}_4^\dagger = \hat{z} - a_\phi t^2/2$ and $\hat{U}_4\hat{p}\hat{U}_4^\dagger = \hat{p} - Ma_\phi t$. Setting $\phi_r = k_L a_\phi t^2$, we simplify the function

$$\hat{U}_4\cos\left(k_L\hat{z} + \frac{\phi_r}{2}\right)\hat{U}_4^\dagger = \cos\left(k_L\hat{z} + \frac{\phi_r}{2} - \frac{k_L a_\phi t^2}{2}\right) = \cos(k_L\hat{z}). \tag{B.11}$$

We determine

$$\begin{aligned}\hat{U}_4\hat{H}'_{\text{2level}}\hat{U}_4 =&\hbar\Delta|e\rangle\langle e| + \frac{(\hat{p} - Ma_\phi t)^2}{2M} + Mg(\hat{z} - a_\phi t^2/2) \\ &+ \frac{1}{2}\hbar\Omega_R\cos(k_L\hat{z})\left[e^{i\phi_s}|e\rangle\langle g| + \text{H.c.}\right],\end{aligned} \tag{B.12}$$

Combining (B.10) and (B.12), we obtain

$$\begin{aligned}\hat{H}''_{\text{2level}} =& \hbar\Delta|e\rangle\langle e| + \frac{\hat{p}^2}{2M} + M(g-a_\phi)\hat{z} - Ma_\phi(g-a_\phi)t^2/2 - \frac{d\chi(t)}{dt} \\ &+ \frac{1}{2}\hbar\Omega_R\cos(k_L\hat{z})\left[e^{i\phi_s}|e\rangle\langle g| + \text{H.c.}\right].\end{aligned} \tag{B.13}$$

The explicit t dependence can be removed by setting $\chi(t) = Ma_\phi(g-a_\phi)t^3/6$, which yields,

$$\hat{H}''_{\text{2level}} = \hbar\Delta|e\rangle\langle e| + \frac{\hat{p}^2}{2M} + Ma\hat{z} + \frac{1}{2}\hbar\Omega_R\cos(k_L\hat{z})\left[e^{i\phi_s}|e\rangle\langle g| + e^{-i\phi_s}|g\rangle\langle e|\right], \tag{B.14}$$

with the acceleration of atoms in this reference frame given by $a \equiv g - a_\phi$.

B.5 Adiabatic elimination in the far detuned limit

In the far detuned limit, for which

$$|\Omega_R| \ll |\Delta|, \tag{B.15}$$

the transition between $|g\rangle$ and $|e\rangle$ may be suppressed [154]. At sufficiently low temperatures, the atoms begin in the ground state $|g\rangle$, and therefore the excited state $|e\rangle$ is not populated. This enables the elimination of the excited state from Hamiltonian (B.14), which reduces to a one-level atom subject to a laser potential.

Making use of a result by S. A. Gardiner [13], it is possible to show that

$$\hat{H}'''_{\text{1level}} = \frac{\hat{p}^2}{2M} + Ma\hat{z} + \hbar\frac{\Omega_R^2}{8\Delta}[\cos(2k_L\hat{z}) + 1]. \tag{B.16}$$

The trig term may be simplified by setting $K = 2k_L$ and performing the unitary transformation

$$\hat{U}_5 = \exp\left(-i\frac{\Omega_R^2}{8\Delta}|g\rangle\langle g|t\right), \tag{B.17}$$

to reveal

$$\hat{H}_{\text{1level}} = \frac{\hat{p}^2}{2M} + Ma\hat{z} + \frac{\hbar\Omega_R^2}{8\Delta}\cos(K\hat{z}). \tag{B.18}$$

B.6 Time dependence of the laser intensity

Assuming that each pulse is spectrally narrow, for which the pulse duration $t_p \gg 1/\Delta$, the time-dependent system can be described by Hamiltonian (B.18) with an additional time-dependent amplitude included in the standing-wave term. We approximate the system by the Hamiltonian

$$\hat{H}_\delta = \frac{\hat{p}^2}{2M} + Ma\hat{z} + \frac{\hbar\Omega_R^2}{8\Delta}\cos(K\hat{z})t_p\sum_{n=0}^{\infty}\delta(t-nT). \tag{B.19}$$

We consider the situation where the laser standing-wave amplitude is switched on and off instantaneously at $t = 0$, with subsequent pulses applied with periodicity T. In practice, a short pulse duration on the order of $t_p = 25$ femtoseconds is experimentally achievable, for example [155]. For the applications discussed in this thesis, we explain in Section 4.2.4 that a δ-function is sufficient due to relatively long times between the pulses [1, 46, 48]. The pulses are separated by an order of microseconds, for example, $T = 133$ μs for caesium [107]; and $T = 1.58$ μs for sodium [109]. Defining an effective potential depth $\phi_d \equiv \Omega_R^2 t_p/8\Delta$, we obtain

$$\hat{H}_{\delta\text{ka}} = \frac{\hat{p}^2}{2M} + Ma\hat{z} - \hbar\phi_d\cos(K\hat{z})\sum_{n=0}^{\infty}\delta(t-nT), \tag{B.20}$$

which has the form of the δ-kicked accelerator Hamiltonian (4.3) [57].

Appendix C

The atom-optical evolution operator

C.1 Overview

In this appendix, we express the time-evolution operator of the δ-kicked accelerator in the reference frame of the the falling atoms. We explain in detail a derivation presented in Publication [3] which generalised a derivation from Publication [1] by incorporating gravitational effects.

C.2 The Floquet operator

For a time-periodic system, the unitary time-evolution operator for a single temporal period is known as the Floquet operator. Hamiltonian (4.3) has temporal period T and we choose to define the Floquet operator from just before one kick to just before the next, such that

$$\hat{F}_{\delta\mathrm{ka}} = \exp\left(-\frac{i}{\hbar}\left[\frac{\hat{p}^2}{2M} + Ma\hat{z}\right]T\right)\exp\left(i\phi_d\cos(K\hat{z})\right). \tag{C.1}$$

Using Eq. (A.20), this Floquet operator can be rewritten to

$$\begin{aligned}\hat{F}_{\delta\mathrm{ka}} = &\exp\left(-\frac{iMa^2T^3}{6\hbar}\right)\exp\left(-\frac{i}{\hbar}\left[\frac{\hat{p}^2}{2M}T + \frac{\hat{p}a}{2}T^2\right]\right)\\ &\times\exp\left(-\frac{iMa\hat{z}T}{\hbar}\right)\exp\left(i\phi_d\cos(K\hat{z})\right).\end{aligned} \tag{C.2}$$

C.3 The transformed Floquet operator in the accelerating frame

In the accelerating frame defined by unitary operator (4.5), the Hamiltonian (4.8) is not periodic in time, so strictly speaking there is no Floquet operator. However, it is useful to consider the transformed Floquet operator which is the time-evolution operator describing kick-to-kick dynamics of the system in the accelerating frame. The Floquet operator (C.1), transformed according to the unitary operator (4.5), becomes

$$\tilde{F}(nT,[n-1]T) = \hat{U}_4(nT)\hat{F}\hat{U}_4^\dagger([n-1]T). \tag{C.3}$$

The time variables on the left-hand side are required to indicate explicitly that the transformed Floquet operator corresponds to the system evolution from just before the $(n-1)$th kick to just before the nth kick [19].

Substituting Eq. (C.2) into Eq. (C.3), then using $\hat{U}_4(nT)\hat{p}\hat{U}_4^\dagger(nT) = \hat{p} - ManT$ and simplifying, we find that

$$\begin{aligned}\tilde{F}(nT,[n-1]T) = &\exp\left(-\frac{iMa^2}{6\hbar}\left[3n^2-3n+1\right]T^3\right)\\ &\times\exp\left(-\frac{i}{\hbar}\left[\frac{\hat{p}^2}{2M}T-\frac{\hat{p}a}{2}(2n-1)T^2\right]\right)\\ &\times\exp\left(i\phi_d\cos(K\hat{z})\right).\end{aligned} \tag{C.4}$$

The first exponential term in Eq. (C.4), i.e., the global phase,[1] is not generally of interest. Therefore, we absorb it into the transformed Floquet operator by defining

$$\tilde{F}_n \equiv \exp\left(i\frac{Ma^2}{6\hbar}[3n^2-3n+1]T^3\right)\tilde{F}(nT,[n-1]T), \tag{C.5}$$

such that

$$\tilde{F}_n = \exp\left(-\frac{i}{\hbar}\left[\frac{\hat{p}^2}{2M}T-\frac{\hat{p}a}{2}(2n-1)T^2\right]\right)\exp\left(i\phi_d\cos(K\hat{z})\right). \tag{C.6}$$

Finally, we substitute the discrete and continuous components of $\hat{p}$ from Eq. (6.2.3) into Eq. (C.6). A further simplification is then possible due to quasimomentum conservation discussed in Section 4.4.2 [1, 19, 125, 126]. When the transformed Floquet operator acts on a general quasimomentum eigenstate $|\psi(\beta)\rangle = \sum_k c_k|k+\beta\rangle$, where the dimensionless

[1]The global phase is corrected slightly from that given previously [57].

momentum eigenkets $|k+\beta\rangle$ satisfy $\hat{p}|k+\beta\rangle = \hbar K(k+\beta)|k+\beta\rangle$ and $\langle k'+\beta'|k+\beta\rangle = \delta_{kk'}\delta(\beta-\beta')$ [1], the operator $\hat{\beta}$ can be replaced by its eigenvalue β. Hence, the transformed Floquet operator, restricted to acting on a particular quasimomentum subspace [19], is

$$\tilde{F}_n(\beta) = \exp\left(-\frac{i}{\hbar}\left[\frac{\hbar^2K^2}{2M}(\hat{k}+\beta)^2T - \pi\hbar\Omega(\hat{k}+\beta)(2n-1)\right]\right)\exp\left(i\phi_d\cos(K\hat{z})\right). \quad \text{(C.7)}$$

In Eq. (C.7), we have defined $\Omega \equiv KaT^2/2\pi$. This parameter is a dimensionless rescaling of the effective gravitation acceleration $a = g - a_\phi$, in the frame comoving with the laser walking wave. The experimental configuration is discussed in detail in Section 4.2, and described mathematically in Section 4.3. In the context of quantum accelerator modes, Ω has been referred to as the unperturbed winding number [21]. This is in analogy with the sine-circle map [156], which can be considered a particular dissipative limiting case of the dynamics of the quantum δ-kicked accelerator.

C.4 Quantum resonant parameters

The time evolution described by the transformed Floquet operator (C.7) varies significantly depending on the system parameters. In this thesis, we investigate the effect of the effective gravity parameter Ω on quantum resonant dynamics in the classically chaotic regime, for which $K^2T\hbar\phi_d/M \geq 1.5$. For the δ-kicked rotor, for which $\Omega = 0$, quantum resonant effects occur for pulse periodicities T equal to integer multiples ℓ of the half-Talbot time $T_T/2$ [104], as explained in Section 3.6. For the atom optical configuration, the Talbot time is defined by Eq. (4.11).

The transformed Floquet operator (C.7), for the case where the pulse periodicity T is given by Eq. (4.10), simplifies to

$$\tilde{F}_n(\beta) = e^{-i\pi\left[\beta^2\ell - \beta\Omega(2n-1)\right]}e^{-i\pi\left[\hat{k}\ell + 2\hat{k}\beta\ell - \hat{k}\Omega(2n-1)\right]}e^{i\phi_d\cos(K\hat{z})}, \quad \text{(C.8)}$$

where, because the eigenvalues of $\hat{k}$ are integer, we have used that $\exp(-i\ell\pi\hat{k}^2) = \exp(-i\ell\pi\hat{k})$ [19, 125, 126]. In the case where $T = \ell T_T/2$, the effective gravity parameter is $\Omega = 2\pi\ell^2aM^2/\hbar^2K^3$.

The first exponential term in transformed Floquet operator (C.8) provides a quasimomentum dependent phase, which we may remove, since it does not change the observed dynamics for the momentum distribution. The third term describes the momentum kick

due to a laser field pulse. The second term can be written more concisely by defining

$$K\gamma_n \equiv \pi\left[(1+2\beta)\ell - \Omega\,(2n-1)\right], \tag{C.9}$$

which means that the transformed Floquet operator simplifies to

$$\tilde{F}_n(\beta) = \exp\left(-iK\gamma_n\hat{k}\right)\exp\left(i\phi_d\cos(K\hat{z})\right). \tag{C.10}$$

It is evident that, for an integer value of Ω, $\exp(-iK\gamma_n\hat{k}) \to \exp(-iK\gamma_0\hat{k})$ and the explicit n-dependence of transformed Floquet operator (C.10) drops out.

C.5 Summary

The derived result of kick-to-kick operator (C.10) is used in Chapter 4 to concisely convey the time evolution in the accelerating frame, with analytic results presented in Chapter 5. In Chapter 6, we investigate the time evolution numerically, and obtain solutions without restricting the treatment to quantum resonant values of the pulse period. The general expression used for the transformed Floquet operator, is given by Eq. (C.6) .

Appendix D

Matrix elements

D.1 Overview

In this appendix we derive expressions for the matrix elements for various values of the system parameters. We summarise results from Publication [2] which we make use of in Publication [3]. In Section D.2, we introduce Gauss sums, which we use to derive a quantity ω, to be used in this thesis to determine the momentum moments.

The ultracold limit is considered for rational Ω values in Section D.3, with the momentum moment results summarised in Section 5.4. We then evaluate ω for a finite temperature, for integer Ω in Section D.4, and for half-integer Ω in Section D.5. The finite temperature matrix elements are used to extract momentum moments in Appendix E, with case of the thermal limit summarised in Section 5.5.

D.2 Matrix element definitions

The distribution evolution given by Eq. (5.4), is dependent upon the probability amplitudes $c_{kj}(\beta, nT)$. The matrix elements are derived to be [2]

$$c_{kj}(\beta, nT) = J_{j-k}(\omega) e^{i(j-k)\chi} e^{-2in\Upsilon k} e^{in^2\pi(k+\beta)\Omega} e^{-in\pi\beta^2\ell}, \tag{D.1}$$

where the parameters ω, χ, and Υ are explained in Section D.2.2.

D.2.1 Distribution evolution

In this thesis, we are interested in the momentum moments and cumulant, which are defined in terms of the momentum distribution, which evolves according to

$$D_j(\beta, t = nT) = \sum_{k=-\infty}^{\infty} |c_{kj}(\beta, nT)|^2 D_k(\beta, t = 0), \tag{D.2}$$

as stated Section 5.2.1. This is dependent upon the modulus of the probability amplitude, which from Eq. (D.1) is given by

$$|c_{kj}(\beta, nT)|^2 = J^2_{j-k}(\omega), \tag{D.3}$$

from which we obtain an expression for the distribution evolution

$$D_j(\beta, t = nT) = \sum_{k=-\infty}^{\infty} J^2_{j-k}(\omega) D_k(\beta, t = 0). \tag{D.4}$$

Therefore, the imaginary part of Eq. (D.1) is not required. In this appendix, we explain how the Bessel function argument in Eq. (D.4) depends upon the parameters of the system.

D.2.2 Matrix element parameters

The matrix elements are dependent upon the parameter ω, which is defined

$$\omega e^{i\chi} = \phi_d \nu \tag{D.5}$$

which is defined by

$$\nu = i e^{-i(2n\Upsilon - n^2\pi\Omega)} \eta, \tag{D.6}$$

incorporating the Gauss sum [157–160]

$$\eta = \sum_{j=0}^{n-1} e^{i(2j\Upsilon - j^2\pi\Omega)}. \tag{D.7}$$

The evolution of the momentum moments is proportional to $|\eta|$, the absolute value of the Gauss sum [2].

The dependence of the Bessel function argument ω incorporates the gravity parameter

Ω in the Gauss sum. The quasimomentum and pulse period T are incorporated into the parameter

$$\Upsilon = \frac{1}{2}\pi(1 + 2\beta)\ell. \tag{D.8}$$

Often the parameter dependence of ν will be specified explicitly by writing $\nu = \nu_{n,\ell}(\Omega, \beta)$, from which the value of ω is inferred by taking its magnitude.

D.3 Evaluating ω for fractional Ω values in the $\beta = 0$ subspace

In the $\beta = 0$ subspace, where $\Upsilon \to \pi\ell/2$, ν can be evaluated analytically for $\Omega = 1/s$, at kick values n which are specific multiples of s [2].

D.3.1 Fractional quantum resonance condition

We investigate quantum resonance features to order s by setting $s(1-\ell)$ to be even. We find that for n a multiple of s,

$$\nu_{n,\ell}(1/s, 0) = ie^{-i\pi[n\ell - n^2\Omega - (1-s\ell^2)/4]}\frac{n}{\sqrt{s}}. \tag{D.9}$$

As a result, for even values of $s(1-\ell)$, the magnitude of ν increases linearly with n at a rate proportional to $1/\sqrt{s}$. This leads to fractional quantum resonant behaviour, where energy is transferred from the laser field to the atom cloud in quasi-periodic bursts. Substituting into Eq. (D.5), the argument of the Bessel function for the sth-order quantum resonant condition is given by

$$\omega = \frac{\phi_d n}{\sqrt{s}}, \tag{D.10}$$

with fractional quantum resonances in the ultracold limit discussed in Section 5.4.3.

D.3.2 Fractional quantum antiresonance condition

For $s(1-\ell)$ even or odd, and n a multiple of $2s$,

$$\nu_{n,\ell}(1/s, 0) = ie^{-i\pi[n\ell - n^2\Omega - (1-s\ell^2)/4]}\frac{n[1 + (-1)^{s(1-\ell)}]}{2\sqrt{s}}. \tag{D.11}$$

Taking the modulus of Eq. (D.11), the Bessel function argument is given by

$$\omega = \frac{\phi_d n}{\sqrt{s}} \frac{[1 + (-1)^{s(1-\ell)}]}{2}. \tag{D.12}$$

Two main classes of behaviour can be identified, as we saw in Section 3.4.3 when considering the simpler case of the quantum δ-kicked rotor, for which acceleration parameter Ω was not incorporated into the model. For even values of $s(1-\ell)$, Eq. (D.12) reduces to the fractional quantum resonant result shown in Eq. (D.10).

In contrast however, for odd values of $s(1-\ell)$, Eq. (D.12) every $2s$ kicks the value of ω collapses to zero, and the initial state is reconstructed. We refer to this temporal reconstruction with period $2s$ as fractional quantum antiresonant behaviour, as are discussed further in Chapter 12.

In Section 5.4.4, we explain that the even-ordered momentum moments oscillate with period $2T$. First-order quantum antiresonance, is characterised by the recurrence of the initial state every two kicks, as depicted in Fig. 4.2, and characterised by the Floquet operator identity (3.31).

D.4 Evaluating ω for integer Ω values

In this section, we evaluate ν for an arbitrary β eigenstate, from which the momentum moments are derived in Section E.3. We consider the case for which Ω is an integer, using the notation $\Omega = r_1$, for which the quantity ν becomes

$$\nu_{n,\ell}(r_1, \beta) = ie^{-2in\Upsilon} e^{in^2\pi r_1} \sum_{j=0}^{n-1} e^{2ij\Upsilon} e^{-ij^2\pi r_1}. \tag{D.13}$$

For n integer we have that $\exp(i\pi r_1 n^2) = \exp(i\pi r_1 n)$ and Eq. (D.13) simplifies to

$$\nu_{n,\ell}(r_1, \beta) = ie^{-2in\Upsilon} e^{in\pi r_1} \sum_{j=0}^{n-1} e^{i(2\Upsilon - \pi r_1)j}. \tag{D.14}$$

Evaluating the geometric series in Eq. (D.14), and simplifying, yields

$$\nu_{n,\ell}(r_1, \beta) = ie^{-i(n+1)(\Upsilon - \pi r_1/2)} \frac{\sin(n[\Upsilon - \pi r_1/2])}{\sin(\Upsilon - \pi r_1/2)}. \tag{D.15}$$

Taking the modulus of ν, we find that ω is given by

$$\omega = \phi_d \frac{\sin(n[\Upsilon - \pi r_1/2])}{\sin(\Upsilon - \pi r_1/2)}. \tag{D.16}$$

In Appendix E, this is substituted into Eqs. (E.3) and (E.5). We find that for integer values of Ω, in the thermal limit, $\langle \hat{p}^2 \rangle_n$ is given by Eq. (E.33) and $\langle \hat{p}^4 \rangle_n$ is given by Eq. (E.35).

Note that for the case of the δ-kicked rotor, we set $\Omega = 0$, and therefore, $r_1 = 0$, which means that

$$\omega = \phi_d \frac{\sin(n\Upsilon)}{\sin(\Upsilon)}, \tag{D.17}$$

as has been verified experimentally [47].

D.5 Evaluating ω for half-integer Ω values

In this section, we evaluate ν for an arbitrary β eigenstate, from which the momentum moments are derived in Section E.4. We consider the case for which Ω is an integer, using the notation $\Omega = r_2/2$, for which the quantity ν becomes

$$\nu_{n,\ell}(r_2/2, \beta) = ie^{-2in\Upsilon} e^{i\pi n^2 r_2/2} \sum_{j=0}^{n-1} e^{2ij\Upsilon} e^{-i\pi j^2 r_2/2}. \tag{D.18}$$

For even values of j, $\exp(-i\pi j^2 r_2/2) = 1$, and for odd values of j, $\exp(-i\pi j^2 r_2/2) = \exp(-i\pi r_2/2)$. For an even number of kicks $n = 2n'$, Eq. (D.18) can be rewritten as two sums, each with the same number of elements, i.e.,

$$\nu_{n=2n',\ell}(r_2/2, \beta) = e^{-4in'\Upsilon} e^{2i\pi n'^2 r_2} \left[\sum_{j_1=0}^{n'-1} e^{4ij_1\Upsilon} + e^{-i\pi r_2/2} \sum_{j_2=0}^{n'-1} e^{2i(2j_2+1)\Upsilon} \right]. \tag{D.19}$$

Simplifying, we find that

$$\nu_{n=2n',\ell}(r_2/2, \beta) = ie^{-4in'\Upsilon} \left[1 + e^{i(2\Upsilon - \pi r_2/2)}\right] \sum_{j=0}^{n'-1} e^{4ij\Upsilon}. \tag{D.20}$$

Evaluating the geometric sum, and simplifying further, yields

$$\nu_{n=2n',\ell}(r_2/2,\beta) = 2ie^{-i[\Upsilon(2n'+1)+\pi r_2/4]}\cos(\Upsilon-\pi r_2/4)\frac{\sin(2n'\Upsilon)}{\sin(2\Upsilon)}. \tag{D.21}$$

Resubstituting for $n = 2n'$ gives

$$\nu_{n,\ell}(r_2/2,\beta) = 2ie^{-i[\Upsilon(n+1)+\pi r_2/4]}\cos(\Upsilon-\pi r_2/4)\frac{\sin(n\Upsilon)}{\sin(2\Upsilon)}, \tag{D.22}$$

which applies for even n only.

Therefore, ω is given by

$$\omega = 2\phi_d\cos(\Upsilon-\pi r_2/4)\frac{\sin(n\Upsilon)}{\sin(2\Upsilon)}. \tag{D.23}$$

In Appendix E, this is substituted into Eqs. (E.3) and (E.5). We find that for half-integer values of Ω, in the thermal limit, $\langle\hat{p}^2\rangle_n$ is given by Eq. (E.37) and $\langle\hat{p}^4\rangle_n$ is given by Eq. (E.39). For the case of the δ-kicked rotor, we set $\Omega = 0$, and therefore, $r_2 = 0$, which means that

$$\omega = 2\phi_d\cos(\Upsilon)\frac{\sin(n\Upsilon)}{\sin(2\Upsilon)}, \tag{D.24}$$

which, as expected, reduces to the integer case given in Eq. (D.17).

D.6 Summary

We have determined ω for a range of parameters, and make use of this quantity to determine the momentum moments. In Appendix E, we derive expressions for the momentum moments for a finite temperature distribution. In Chapter 5, we summarise the analytic observables predicted using this theory. We verify that the analytic results are consistent with the numerical results for the ultracold limit in Chapter 7 and for the thermal limit in Chapter 8.

Appendix E

Momentum moments

E.1 Overview

At finite temperature, the qth-order momentum moment is given by Eq. (5.7), which are evaluated in this appendix. We explain a method for evaluating momentum moments that is presented in Publication [2] for integer values of Ω. We make use of this method to derive momentum moments for half-integer values of Ω, as presented in Publication [3]. For various parameters, we substitute matrix element (D.1) using the values of ω derived in Appendix D. Returning to the atomic momentum notation $p = \hbar K(k + \beta)$, we find that

$$\langle \hat{p}^q \rangle_n = \int dp \sum_{j=-\infty}^{\infty} J_j^2(\omega)\, D(p)\, (\hbar K j + p)^q . \tag{E.1}$$

Using the Bessel function identity $J_{-j}(\eta) = (-1)^j J_j(\eta)$, we find that all odd-ordered momentum moments are zero for symmetric momentum distributions $D(p)$. The even-ordered momentum moments are finite in general. Here we consider only the second- and fourth-order momentum moments in detail.

The second-order momentum moment is given by

$$\langle \hat{p}^2 \rangle_n = \int dp \sum_{j=-\infty}^{\infty} J_j^2(\omega)\, D(p) \left[(\hbar K)^2 j^2 + 2\hbar K j p + p^2 \right] . \tag{E.2}$$

Using the Bessel function identities $\sum_{j=-\infty}^{\infty} j^2 J_j^2(\eta) = \eta^2/2$, $\sum_{j=-\infty}^{\infty} j J_j^2(\eta) = 0$, and

$\sum_{j=-\infty}^{\infty} J_j^2(\eta) = 1$ [1, 133], Eq. (E.2) becomes

$$\langle \hat{p}^2 \rangle_n = \int dp D(p) p^2 + (\hbar K)^2 \frac{1}{2} \int dp D(p) \omega^2. \tag{E.3}$$

The fourth-order momentum moment is given by

$$\langle \hat{p}^4 \rangle_n = \int dp \sum_{j=-\infty}^{\infty} J_j^2(\omega) D(p) \left[(\hbar K)^4 j^4 + 4(\hbar K)^3 j^3 p + 6(\hbar K)^2 j^2 p^2 + 4\hbar K j p^3 + p^4 \right]. \tag{E.4}$$

Using the Bessel function identities above, as well as $\sum_{j=-\infty}^{\infty} j^3 J_j^2(\eta) = 0$ and $\sum_{j=-\infty}^{\infty} j^4 J_j^2(\eta) = 3\eta^4/8 + \eta^2/2$ [2], Eq. (E.4) becomes

$$\begin{aligned} \langle \hat{p}^4 \rangle_n = & \int p^4 D(p) dp + (\hbar K)^4 \frac{1}{2} \int dp D(p) \omega^2 \\ & + (\hbar K)^2 3 \int dp D(p) p^2 \omega^2 + (\hbar K)^4 \frac{3}{8} \int dp D(p) \omega^4. \end{aligned} \tag{E.5}$$

In Section E.2, we derive analytic expressions for these integrals, with the moments evaluated for integer values of Ω in Section E.3, and for half-integer values of Ω in Section E.4.

E.2 Momentum distribution integrals

In this section, we obtain analytic expressions for momentum integrals, which we substitute into Eqs. (E.3) and (E.5).

E.2.1 Initial momentum moments

At finite temperature, the initial qth-order momentum moment is given by Eq. (E.1) with $\omega = 0$, given by

$$\langle \hat{p}^q \rangle_{n=0} = \int dp D(p) p^q. \tag{E.6}$$

In the case where the atomic momenta are distributed according to the Gaussian (5.14), the initial second-order momentum moment is

$$\langle \hat{p}^2 \rangle_{n=0} = \int dp D(p) p^2 = (\hbar K)^2 w^2, \tag{E.7}$$

and the initial fourth-order momentum moment is

$$\langle \hat{p}^4 \rangle_{n=0} = \int dp D(p) p^4 = 3(\hbar K)^4 w^4. \tag{E.8}$$

E.2.2 Evaluating $\int dp D(p)\omega^2$

When Ω takes integer values, i.e., $\Omega = r_1$, ω is given by Eq. (D.16) and

$$\int dp D(p)\omega^2 = \phi_d^2 \int dp D(p) \frac{\sin^2(n[\Upsilon - \pi r_1/2])}{\sin^2(\Upsilon - \pi r_1/2)}. \tag{E.9}$$

Using the expansion [2]

$$\frac{\sin^2(nx)}{\sin^2(x)} = n + 2\sum_{m=1}^{n-1}(n-m)\cos(2mx), \tag{E.10}$$

we rearrange Eq. (E.9) to

$$\int dp D(p)\omega^2 = n\phi_d^2 \int dp D(p) + 2\phi_d^2 \sum_{m=1}^{n-1}(n-m)(-1)^{mr_1} \int dp D(p)\cos(2m\Upsilon). \tag{E.11}$$

In the case where $D(p)$ is Gaussian [see Eq. (5.14)], $\int dp D(p) = 1$ by our choice of normalization, and the second integral in Eq. (E.11) can be evaluated using $\cos(2m\Upsilon) = (-1)^{m\ell}\cos(2m\pi\ell p/\hbar K)$ with

$$\int dp \cos(\lambda p) e^{-p^2/\alpha^2} = \sqrt{\pi}\alpha e^{-\lambda^2\alpha^2/4}. \tag{E.12}$$

We find that

$$\int dp D(p)\omega^2 = n\phi_d^2 + 2\phi_d^2 \sum_{m=1}^{n-1}(n-m)(-1)^{m(r_1+\ell)} e^{-2m^2\ell^2\pi^2 w^2}. \tag{E.13}$$

When Ω takes half-integer values, i.e., $\Omega = r_2/2$ with r_2 odd, ω is given by Eq. (D.23) for even kick numbers $n = 2n'$. Hence,

$$\int dp D(p)\omega^2 = 4\phi_d^2 \int dp D(p) \frac{\sin^2(2n'\Upsilon)}{\sin^2(2\Upsilon)} \cos^2(\Upsilon - \pi r_2/4). \tag{E.14}$$

Using Eq. (E.10), $\cos(4m\Upsilon) = \cos(4m\pi\ell p/\hbar K)$, and

$$\cos^2\left(\Upsilon - \frac{\pi r_2}{4}\right) = \frac{1}{2} + \frac{1}{2}(-1)^{\ell+(r_2-1)/2}\sin\left(\frac{2\pi\ell p}{\hbar K}\right), \tag{E.15}$$

we rearrange Eq. (E.14) to

$$\begin{aligned}\int dpD(p)\omega^2 =& 2n'\phi_d^2 + 4\phi_d^2\sum_{m=1}^{n'-1}(n'-m)\int dpD(p)\cos\left(\frac{4m\pi\ell p}{\hbar K}\right) \\ &+ 2\phi_d^2(-1)^{\ell+(r_2-1)/2}\int dpD(p)\sin\left(\frac{2\pi\ell p}{\hbar K}\right) \\ &\times\left[n' + 2\sum_{m=1}^{n'-1}(n'-m)\cos\left(\frac{4m\pi\ell p}{\hbar K}\right)\right],\end{aligned} \tag{E.16}$$

where again we have used the normalization of $D(p)$ to evaluate the first term. In the case where the atomic momenta are distributed according to the Gaussian (5.14), the first integral on the right-hand side of Eq. (E.16) can be evaluated using Eq. (E.12). The remaining integrals vanish due to the even parity of $D(p)$. Therefore, we find that

$$\int dpD(p)\omega^2 = 2n'\phi_d^2 + 4\phi_d^2\sum_{m=1}^{n'-1}(n'-m)e^{-8m^2\pi^2\ell^2w^2}. \tag{E.17}$$

Substituting $n = 2n'$ yields

$$\int dpD(p)\omega^2 = n\phi_d^2 + 2\phi_d^2\sum_{m=1}^{n/2-1}(n-2m)e^{-8m^2\pi^2\ell^2w^2}, \tag{E.18}$$

where n is even.

E.2.3 Evaluating $\int dpD(p)p^2\omega^2$

For integer Ω, i.e., $\Omega = r_1$,

$$\int dpD(p)p^2\omega^2 = \phi_d^2\int dpD(p)p^2\frac{\sin^2(n[\Upsilon - \pi r_1/2])}{\sin^2(\Upsilon - \pi r_1/2)}. \tag{E.19}$$

Following the evaluation of $\int \omega^2 D(p)dp$ in Section E.2.2, for integer Ω, and making use of Eq. (E.7) and the integral

$$\int p^2 \cos(\lambda p) e^{-p^2/\alpha^2} dp = \frac{1}{2}\sqrt{\pi}\alpha^3 \left(1 - \frac{\alpha^2\lambda^2}{2}\right) e^{-\lambda^2\alpha^2/4}, \tag{E.20}$$

we find that for a Gaussian $D(p)$ described by Eq. (5.14),

$$\int dpD(p)p^2\omega^2 = (\hbar K)^2 w^2 \phi_d^2 \left[n + 2\sum_{m=1}^{n-1} (n-m)(-1)^{m(r_1+\ell)}(1 - 4m^2\pi^2\ell^2 w^2) e^{-2m^2\pi^2\ell^2 w^2} \right]. \tag{E.21}$$

For half-integer Ω, i.e., $\Omega = r_2/2$, and even kick numbers $n = 2n'$,

$$\int dpD(p)p^2\omega^2 = 4\phi_d^2 \int dpD(p)p^2 \frac{\sin^2(2n'\Upsilon)}{\sin^2(2\Upsilon)} \cos^2(\Upsilon - \pi r_2/4). \tag{E.22}$$

Following the treatment in Section E.2.2, for half-integer Ω, and using Eqs. (E.7) and (E.20), we find that for a Gaussian $D(p)$ described by Eq. (5.14),

$$\int dpD(p)p^2\omega^2 = (\hbar K)^2 w^2 \phi_d^2 \left[2n' + 4\sum_{m=1}^{n'-1} (n'-m)(1 - 4m^2\pi^2\ell^2 w^2) e^{-8m^2\pi^2\ell^2 w^2} \right]. \tag{E.23}$$

Substituting $n = 2n'$ yields

$$\int dpD(p)p^2\omega^2 = (\hbar K)^2 w^2 \phi_d^2 \left[n + 2\sum_{m=1}^{n/2-1} (n-2m)(1 - 4m^2\pi^2\ell^2 w^2) e^{-8m^2\pi^2\ell^2 w^2} \right]. \tag{E.24}$$

E.2.4 Evaluating $\int dpD(p)\omega^4$

For integer Ω,

$$\int dpD(p)\omega^4 = \phi_d^4 \int dpD(p) \frac{\sin^4(n[\Upsilon - \pi r_1/2])}{\sin^4(\Upsilon - \pi r_1/2)}. \tag{E.25}$$

Using the expansion [2]

$$\begin{aligned} \frac{\sin^4(nx)}{\sin^4(x)} =& \frac{n}{3}(2n^2+1) + \sum_{m=1}^{n-1} \cos(2mx) \left[m^3 - 2nm^2 - m + \frac{2n}{3}(2n^2+1) \right] \\ & - \sum_{m=n}^{2n-2} \cos(2mx) \left[\frac{m^3}{3} - 2nm^2 + \left(4n^2 - \frac{1}{3}\right) m + \frac{2n}{3}(1-4n^2) \right], \end{aligned} \tag{E.26}$$

and following the treatment in Appendix E.2.2, we find that

$$\begin{aligned}\int dpD(p)\omega^4 =& \frac{n}{3}\phi_d^4(2n^2+1) \\ &+ \phi_d^4 \sum_{m=1}^{n-1}(-1)^{m(r_1+\ell)} e^{-2m^2\pi^2\ell^2w^2}\left[m^3 - 2nm^2 - m + \frac{2n}{3}(2n^2+1)\right] \\ &- \phi_d^4 \sum_{m=n}^{2n-2}(-1)^{m(r_1+\ell)} e^{-2m^2\pi^2\ell^2w^2} \\ &\times \left[\frac{m^3}{3} - 2nm^2 + \left(4n^2 - \frac{1}{3}\right) m\frac{2n}{3}(1-4n^2)\right].\end{aligned} \tag{E.27}$$

For half-integer Ω, and even kick numbers $n = 2n'$,

$$\int dpD(p)\omega^4 = 16\phi_d^4 \int dpD(p) \frac{\sin^4(2n'\Upsilon)}{\sin^4(2\Upsilon)} \cos^4(\Upsilon - \pi r_2/4). \tag{E.28}$$

Using Eq. (E.26),

$$\cos^4\left(\Upsilon - \frac{\pi r_2}{4}\right) = \frac{3}{8} - \frac{1}{8}\cos\left(\frac{4\pi\ell p}{\hbar K}\right) + \frac{1}{2}(-1)^{\ell+(r_2-1)/2}\sin\left(\frac{2\pi\ell p}{\hbar K}\right), \tag{E.29}$$

and following the treatment in Appendix E.2.2, we find that

$$\begin{aligned}\int dpD(p)\omega^4 =& \frac{2\phi_d^4}{3}n'(2n'^2+1)\left[3 - e^{-8\pi^2\ell^2w^2}\right] \\ &+ \phi_d^4 \sum_{m=1}^{n'-1}\left[m^3 - 2n'm^2 - m + \frac{2n'}{3}(2n'^2+1)\right] \\ &\times \left[6e^{-8\pi^2m^2\ell^2w^2} - e^{-8\pi^2(m+1)^2\ell^2w^2} - e^{-8\pi^2(m-1)^2\ell^2w^2}\right] \\ &- \phi_d^4 \sum_{m=n'}^{2n'-2}\left[\frac{m^3}{3} - 2n'm^2 + \frac{1}{3}(12n'^2-1)m + \frac{2n'}{3}(1-4n'^2)\right] \\ &\times \left[6e^{-8\pi^2m^2\ell^2w^2} - e^{-8\pi^2(m+1)^2\ell^2w^2} - e^{-8\pi^2(m-1)^2\ell^2w^2}\right].\end{aligned} \tag{E.30}$$

Substituting $n = 2n'$ then yields

$$\begin{aligned}\int dpD(p)\omega^4 =& \frac{1}{6}n(n^2+2)\phi_d^4\left[3-e^{-8\pi^2\ell^2w^2}\right] \\ &+ \phi_d^4\sum_{m=1}^{n/2-1}\left[m^3-nm^2-m+\frac{1}{6}n(n^2+2)\right] \\ &\times\left[6e^{-8\pi^2m^2\ell^2w^2}-e^{-8\pi^2(m+1)^2\ell^2w^2}-e^{-8\pi^2(m-1)^2\ell^2w^2}\right] \\ &- \phi_d^4\sum_{m=n/2}^{n-2}\left[\frac{m^3}{3}-nm^2+\frac{1}{3}(3n^2-1)m+\frac{n}{3}(1-n^2)\right] \\ &\times\left[6e^{-8\pi^2m^2\ell^2w^2}-e^{-8\pi^2(m+1)^2\ell^2w^2}-e^{-8\pi^2(m-1)^2\ell^2w^2}\right].\end{aligned} \tag{E.31}$$

E.3 Momentum moments for integer Ω values

In this section, we explain an analytic method to describe the time evolution for integer Ω values, developed by P. L. Halkyard, and published in [2]. The theory presented here treats the momentum distribution by Gaussian function (5.14), improving upon an analytic treatment presented in [1], for which the initial momentum was modelled by a square distribution function.

For integer values of Ω, the second-order momentum moment evolution for a Gaussian distribution is given by Eq. (E.3) with ω of Eq. (D.15). Using the integral results (E.7) and (E.13), we find that

$$\frac{\langle\hat{p}^2\rangle_n}{(\hbar K)^2} = w^2+\frac{\phi_d^2}{2}n+\phi_d^2\sum_{m=1}^{n-1}(n-m)(-1)^{m(r_1+\ell)}e^{-2m^2\ell^2\pi^2w^2}. \tag{E.32}$$

In the limit $w \gg 1/\sqrt{2}\pi\ell$, the decaying terms become negligible and we can write

$$\langle\hat{p}^2\rangle_n = (\hbar K)^2\left(w^2+\frac{\phi_d^2}{2}n\right). \tag{E.33}$$

The fourth-order momentum moment for a Gaussian distribution is given by Eq. (E.5).

Using Eqs. (E.8), (E.13), (E.21), and (E.27), we find that

$$\begin{aligned}\frac{\langle\hat{p}^4\rangle_n}{(\hbar K)^4} =& 3w^4 + \frac{\phi_d^2}{2}n + 3\phi_d^2 w^2 n + \frac{\phi_d^4}{8}n(2n^2+1) \\ &+ \phi_d^2 \sum_{m=1}^{n-1}(-1)^{m(r_1+\ell)}(n-m)e^{-2m^2\ell^2\pi^2w^2} \\ &\times \left[1 + 6w^2(1 - 4m^2\ell^2\pi^2w^2)\right] \\ &+ \frac{3\phi_d^4}{8}\sum_{m=1}^{n-1}(-1)^{m(r_1+\ell)}e^{-2m^2\ell^2\pi^2w^2}\left[m^3 - 2nm^2 - m + \frac{2n}{3}(2n^2+1)\right] \\ &- \frac{3\phi_d^4}{8}\sum_{m=n}^{2n-2}(-1)^{m(r_1+\ell)}e^{-2m^2\ell^2\pi^2w^2}\left[\frac{m^3}{3} - 2nm^2\frac{(12n^2-1)}{3}m + \frac{2n}{3}(1-4n^2)\right].\end{aligned} \tag{E.34}$$

Similarly, in the limit $w \gg 1/\sqrt{2}\pi\ell$, the decaying terms become negligible and we can write

$$\langle\hat{p}^4\rangle_n = (\hbar K)^4\left(\frac{\phi_d^4}{4}n^3 + \frac{\phi_d^4}{8}n + \frac{\phi_d^2}{2}n + 3w^2\phi_d^2 n + 3w^4\right). \tag{E.35}$$

E.4 Momentum moments for half-integer Ω values

In this section, we make use of the analytic method introduced by P. L. Halkyard to evaluate the time evolution for half-integer Ω values, as published in [?].

For half-integer values of Ω, the second-order momentum moment evolution for a Gaussian distribution is given by Eq. (E.3) with ω of Eq. (D.22). Using Eqs. (E.7) and (E.18), we find that

$$\frac{\langle\hat{p}^2\rangle_n}{(\hbar K)^2} = w^2 + \frac{\phi_d^2}{2}n + \phi_d^2\sum_{m=1}^{n/2-1}(n-2m)e^{-8m^2\pi^2\ell^2w^2}. \tag{E.36}$$

In the limit $w \gg 1/2\sqrt{2}\pi\ell$, the decaying terms become negligible and we can write

$$\langle\hat{p}^2\rangle_n = (\hbar K)^2\left(w^2 + \frac{\phi_d^2}{2}n\right). \tag{E.37}$$

Note that Eqs. (E.36) and (E.37) only apply for even n.

The fourth-order momentum moment for a Gaussian distribution is given by Eq. (E.5).

Using Eqs. (E.8), (E.18), (E.24), and (E.31), we find that

$$\begin{aligned}\frac{\langle\hat{p}^4\rangle_n}{(\hbar K)^4} =& 3w^4 + \frac{\phi_d^2}{2}n + 3w^2\phi_d^2 n + \frac{\phi_d^4}{16}n(n^2+2)\left(3 - e^{-8\pi^2 w^2\ell^2}\right) \\ &+ 6\phi_d^2 w^2 \sum_{m=1}^{n/2-1}(n-2m)(1-4\pi^2 m^2\ell^2 w^2)e^{-8\pi^2 m^2\ell^2 w^2} \\ &+ \frac{3\phi_d^4}{8}\sum_{m=1}^{n/2-1}\left[m^3 - nm^2 - m + \frac{1}{6}n(n^2+2)\right] \\ &\times\left[6e^{-8\pi^2 m^2\ell^2 w^2} - e^{-8\pi^2(m+1)^2\ell^2 w^2} - e^{-8\pi^2(m-1)^2\ell^2 w^2}\right] \\ &- \frac{3\phi_d^4}{8}\sum_{m=n/2}^{n-2}\left[\frac{m^3}{3} - nm^2 + \frac{1}{3}(3n^2-1)m + \frac{n}{3}(1-n^2)\right] \\ &\times\left[6e^{-8\pi^2 m^2\ell^2 w^2} - e^{-8\pi^2(m+1)^2\ell^2 w^2} - e^{-8\pi^2(m-1)^2\ell^2 w^2}\right].\end{aligned} \tag{E.38}$$

In the limit $w \gg 1/2\sqrt{2}\pi\ell$, we can write

$$\langle\hat{p}^4\rangle_n = (\hbar K)^4\left(\frac{\phi_d^4}{8}n^3 + \frac{5\phi_d^4}{8}n + \frac{\phi_d^2}{2}n + 3w^2\phi_d^2 n + 3w^4\right). \tag{E.39}$$

Again, we emphasize that Eqs. (E.37) and (E.39) only apply for even n.

E.5 Summary

We discuss the analytic momentum moment results in Section 5.5, from which the momentum cumulants are derived. In Chapter 8 we verify that these equations for the thermal limit are consistent with the numerical simulations, and extend the model by exploring the temperature dependence in Chapter 11

In the thermal limit, the second-order momentum moment is independent of Ω, as shown analytically by Eqs. (E.33) and (E.37). In comparison the fourth-order momentum moment does depend upon Ω, as seen from Eqs. (E.35) and (E.39).

Bibliography

[1] M. Saunders, P. L. Halkyard, K. J. Challis, and S. A. Gardiner. Manifestation of quantum resonances and antiresonances in a finite-temperature dilute atomic gas. *Phys. Rev. A*, 76:043415, 2007. Results presented in Chapter 10.

[2] P. L. Halkyard, M. Saunders, K. J. Challis, and S. A. Gardiner. Power-law behavior in the quantum-resonant evolution of the δ-kicked accelerator. *Phys. Rev. A*, 78:063401, 2008.

[3] M. Saunders, P. L. Halkyard, S. A. Gardiner, and K. J. Challis. Fractional resonances in the atom-optical δ-kicked accelerator. *Phys. Rev. A*, 79:023423, 2009. Results presented in Chapter 11.

[4] M. C. Gutzwiller. *Chaos in Classical and Quantum Mechanics.* Springer, New York, 1991.

[5] F. Haake. *Quantum Signatures of Chaos.* Springer, Berlin, 2nd edition, 2001.

[6] L. E. Reichl. *The Transition to Chaos: Conservative Classical Systems and Quantum Manisfestations.* Springer, New York, 2nd edition, 2004.

[7] B. V. Chirikov. A universal instability of many-dimensional oscillator systems. *Phys. Rep.*, 52:263, 1979.

[8] B. V. Chirikov and D. L. Shepelyansky. Chirikov standard map. *Scholarpedia*, 3(3):3550, 2008.

[9] G. Casati, B. V. Chirikov, F. M. Izraelev, and J. Ford. Stochastic behavior of a quantum pendulum under a periodic perturbation. In G. Casati and J. Ford, editors, *Stochastic Behavior in Classical and Quantum Hamiltonian Systems*, New York, 1979. Springer.

[10] F. M. Izrailev and D. Shepelyansky. Quantum resonance for a rotor in a nonlinear periodic field. *Soviet Physics Doklady*, 24:996, 1979.

[11] F. M. Izrailev and D. Shepelyansky. Quantum resonance for a rotator in a nonlinear periodic field. *Theor. Math. Phys.*, 43:553, 1980.

[12] F. M. Izrailev. Nearly linear mappings and their applicaitons. *Physica D*, 1:243, 1980.

[13] S. A. Gardiner. *Quantum measurement, quantum chaos, and Bose-Einstein condensates.* PhD thesis, Leopold-Franzens-Universität Innsbruck, Innsbruck, Österreich, January 2000.

[14] S. A. Gardiner, J. I. Cirac, and P. Zoller. Quantum chaos in an ion trap: The delta-kicked harmonic oscillator. *Phys. Rev. Lett.*, 79:4790, 1997.

[15] S. A. Gardiner, D. Jaksch, R. Dum, J. I. Cirac, and P. Zoller. Nonlinear matter wave dynamics with a chaotic potential. *Phys. Rev. A*, 62:023612, 2000.

[16] S. Schlunk, M. B. d'Arcy, S. A. Gardiner, D. Cassettari, R. M. Godun, and G. S. Summy. Signatures of quantum stability in a classically chaotic system. *Phys. Rev. Lett.*, 90:054101, 2003.

[17] S. Schlunk, M. B. d'Arcy, S. A. Gardiner, and G. S. Summy. Experimental observation of high-order quantum accelerator modes. *Phys. Rev. Lett.*, 90:124102, 2003.

[18] Z.-Y. Ma, M. B. d'Arcy, and S. A. Gardiner. Gravity-sensitive quantum dynamics in cold atoms. *Phys. Rev. Lett.*, 93:164101, 2004.

[19] R. Bach, K. Burnett, M. B. d'Arcy, and S. A. Gardiner. Quantum-mechanical cumulant dynamics near stable periodic orbits in phase space: Applications to the classical-like dynamics of quantum accelerator modes. *Phys. Rev. A*, 71:033417, 2005.

[20] Z.-Y. Ma, K. Burnett, M. B. d'Arcy, and S. A. Gardiner. Quantum random walks using quantum accelerator modes. *Phys. Rev. A*, 73:013401, 2006.

[21] A. Buchleitner, M. B. d'Arcy, S. Fishman, S. A. Gardiner, I. Guarneri, Z.-Y. Ma, L. Rebuzzini, and G. S. Summy. Quantum accelerator modes from the farey tree. *Phys. Rev. Lett.*, 96:164101, 2006.

[22] T. P. Billam and S. A. Gardiner. Quantum resonances in the δ-kicked harmonic oscillator. *arXiv*, 0809:4373, 2008.

[23] I. Dana, E. Eisenberg, and N. Shnerb. Dynamical localization near quantum antiresonance: Exact results and a solvable case. *Phys. Rev. Lett.*, 74:686, 1995.

[24] I. Dana, E. Eisenberg, and N. Shnerb. Antiresonance and localization in quantum dynamics. *Phys. Rev. E*, 54:5948, 1996.

[25] I. Dana and D. L. Dorofeev. General approach to the quantum kicked particle in a magnetic field: Quantum-antiresonance transition. *Phys. Rev. E*, 72:046205, 2005.

[26] I. Dana and D. L. Dorofeev. General quantum resonances of the kicked particle. *Phys. Rev. E*, 73:026206, 2006.

[27] I. Dana and D. L. Dorofeev. Fluctuations and transients in quantum-resonant evolution. *Phys. Rev. E*, 74:045201(R), 2006.

[28] I. Dana and V. Roitberg. Quantum resonances and ratchets in freely-falling frames. *Phys. Rev. E*, 76:015201(R), 2007.

[29] I. Dana, V. Ramareddy, I Talukdar, and G. S. Summy. Experimental realization of quantum-resonance ratchets at arbitrary quasimomenta. *Phys. Rev. Lett.*, 100:024103, 2008.

[30] S. Wimberger, I. Guarneri, and S. Fishman. Quantum resonances and decoherence for δ-kicked atoms. *Nonlinearity*, 16:1381, 2003.

[31] S. Wimberger, I. Guarneri, and S. Fishman. Classical scaling theory of quantum resonances. *Phys. Rev. Lett.*, 92:084102, 2004.

[32] S. Wimberger and M. Sadgrove. The role of quasi-momentum in the resonant dynamics of the atom-optics kicked rotor. *J. Phys. A*, 38:10549, 2005.

[33] S. Wimberger, R. Mannella, O. Morsch, and E. Arimondo. Resonant nonlinear quantum transport for a periodically kicked Bose condensate. *Phys. Rev. Lett.*, 94:130404, 2005.

[34] S. Wimberger, P. Schlagheck, C. Eltschka, and A. Buchleitner. Resonance-assisted decay of nondispersive wave-packets. *Phys. Rev. Lett.*, 97:043001, 2006.

[35] T. Boness, S. Bose, and T. S. Monteiro. Entanglement and dynamics of spin chains in periodically pulsed magnetic fields: Accelerator modes. *Phys. Rev. Lett.*, 96:187201, 2006.

[36] T. Boness, M. M. A. Stocklin, and T. S. Monteiro. Quantum chaos with spin-chains in pulsed magnetic fields. *Prog. Theo. Phys.*, 166:85, 2007.

[37] J. Reslen, C. E. Creffield, and T. S. Monteiro. Dynamical instability in kicked Bose-Einstein condensates. *arXiv*, 0707:1653, 2008.

[38] C. E. Creffield, G. Hur, and T. S. Monteiro. Localization-delocalization transition in a system of quantum kicked rotors. *Phys. Rev. Lett.*, 96:024103, 2006.

[39] C. E. Creffield, S. Fishman, and T. S. Monteiro. Theory of 2δ-kicked quantum rotors. *Phys. Rev. E*, 73:066202, 2006.

[40] M. M. A. Stocklin and T. S. Monteiro. Classical momentum diffusion in double-δ-kicked particles. *Phys. Rev. E*, 74:026210, 2006.

[41] J. Wang, T. S. Monteiro, S. Fishman, J. P. Keating, and R. Schubert. Fractional $\hbar$ scaling for quantum kicked rotors without cantori. *Phys. Rev. Lett*, 99:234101, 2007.

[42] T. S. Monteiro, P. A. Dando, N. A. C. Hutchings, and M. R. Isherwood. Proposal for a chaotic ratchet using cold atoms in optical lattices. *Phys. Rev. Lett.*, 89:194102, 2002.

[43] G. Hur, C. E. Creffield, P. H. Jones, and T. S. Monteiro. Chaotic quantum ratchets and filters with cold atoms in optical lattices: Analysis using floquet states. *Phys. Rev. A*, 72:013403, 2005.

[44] T. S. Monteiro, A. Rançon, and J. Ruostekoski. Nonlinear resonances in δ-kicked Bose-Einstein condensates. *Phys. Rev. Lett.*, 102:014102, 2009.

[45] F. L. Moore, J. C. Robinson, C. Bharucha, P. E. Williams, and M. G. Raizen. Observation of dynamical localization in atomic momentum transfer: A new testing ground for quantum chaos. *Phys. Rev. Lett.*, 73:2974, 1994.

[46] F. L. Moore, J. C. Robinson, C. F. Bharucha, B. Sundaram, and M. G. Raizen. Atom optics realization of the quantum δ-kicked rotor. *Phys. Rev. Lett.*, 75:4598, 1995.

[47] C. F. Bharucha, J. C. Robinson, F. L. Moore, B. Sundaram, Q. Niu, and M. G. Raizen. Dynamical localisation of ultracold sodium atoms. *Phys. Rev. E*, 60:3881, 1999.

[48] B. G. Klappauf, W. H. Oskay, D. A. Steck, and M. G. Raizen. Quantum chaos with cesium atoms: pushing the boundaries. *Physica D*, 131:78, 1999.

[49] V. Milner, D. A. Steck, W. H. Oskay, and M. G. Raizen. Recovery of classically chaotic behavior in a noise-driven quantum system. *Phys. Rev. E*, 61:7223, 2000.

[50] W. H. Oskay, D. A. Steck, V. Milner, B. G. Klappauf, and M. G. Raizen. Ballistic peaks at quantum resonance. *Opt. Comm.*, 179:137, 2000.

[51] D. A. Steck, V. Milner, W. H. Oskay, and M. G. Raizen. Quantitative study of amplitude noise effects on dynamical localization. *Phys. Rev. E*, 62:3461, 2000.

[52] W. H. Oskay, D. A. Steck, and M. G. Raizen. Timing noise effects on dynamical localization. *Chaos, Solitons & Fractals*, 16:409, 2003.

[53] C. Zhang, J. Liu, M. G. Raizen, and Q. Niu. Transition to instability in a kicked Bose-Einstein condensate. *Phys. Rev. Lett.*, 92:054101, 2004.

[54] B. G. Klappauf, W. H. Oskay, D. A. Steck, and M. G. Raizen. Observation of noise and dissipation effects on dynamical localization. *Phys. Rev. Lett.*, 81:4044, 1998.

[55] M. K. Oberthaler, R. M. Godun, M. B. d'Arcy, G. S. Summy, and K. Burnett. Observation of quantum accelerator modes. *Phys. Rev. Lett.*, 83:4447, 1999.

[56] R. M. Godun, M. B. d'Arcy, M. K. Oberthaler, G. S. Summy, and K. Burnett. Quantum accelerator modes: A tool for atom optics. *Phys. Rev. A*, 62:013411, 2000.

[57] M. B. d'Arcy, R. M. Godun, M. K. Oberthaler, G. S. Summy, K. Burnett, and S. A. Gardiner. Approaching classicality in quantum accelerator modes through decoherence. *Phys. Rev. E*, 64:056233, 2001.

[58] M. B. d'Arcy, R. M. Godun, M. K. Oberthaler, D. Cassettari, and G. S. Summy. Quantum enhancement of momentum diffusion in the delta-kicked rotor. *Phys. Rev. Lett.*, 87:074102, 2001.

[59] R. M. Godun, M. B. d'Arcy, G. S. Summy, and K. Burnett. Prospects for atom interferometry. *Contemporary Physics*, 42:77, 2001.

[60] M. B. d'Arcy, R. M. Godun, D. Cassettari, and G. S. Summy. Accelerator-mode-based technique for studying quantum chaos. *Phys. Rev. A*, 67:023605, 2003.

[61] Z.-Y. Ma. *Cold atom dynamics in laser fields.* PhD thesis, Oxford, 2005.

[62] M. B. d'Arcy, R. M. Godun, G. S. Summy, I. Guarneri, S. Wimberger, S. Fishman, and A. Buchleitner. Decoherence as a probe of coherent quantum dynamics. *Phys. Rev. A*, 69:027201, 2004.

[63] G. J. Duffy, A. S. Mellish, K. J. Challis, and A. C. Wilson. Nonlinear atom-optical δ-kicked harmonic oscillator using a Bose-Einstein condensate. *Phys. Rev. A*, 70:041602(R), 2004.

[64] G. Behinaein, V. Ramareddy, P. Ahmadi, and G. S. Summy. Exploring the phase space of the quantum δ-kicked accelerator. *Phys. Rev. Lett.*, 97:244101, 2006.

[65] C. Ryu, M. F. Andersen, A. Vaziri, M. B. d'Arcy, J. M. Grossman, K. Helmerson, and W. D. Phillips. High-order quantum resonances observed in a periodically kicked Bose-Einstein condensate. *Phys. Rev. Lett.*, 96:160403, 2006.

[66] J. F. Kanem, S. Maneshi, M. Partlow, M. Spanner, and A. M. Steinberg. Observation of high-order quantum resonances in the kicked rotor. *Phys. Rev. Lett.*, 98:083004, 2007.

[67] L. Rebuzzini, I. Guarneri, and R. Artuso. Spinor dynamics of quantum accelerator modes near higher-order resonances. *Phys. Rev. A*, 79:033614, 2009.

[68] I. G. Hughes. Atom-light interactions and laser cooling. Graduate Lecture Course, 2005.

[69] C. J. Foot. *Atomic physics.* Oxford University Press, Oxford, 2005.

[70] M. Fox. *Quantum optics.* Oxford University Press, Oxford, 2006.

[71] P. A. Tipler. *Physics for Scientists and Engineers.* W. H. Freeman, 4th edition, 1999.

[72] S. A. Gardiner. Dynamics and many-body physics. Graduate Lecture Course, 2005.

[73] A. J. Lichtenberg and M. A. Lieberman. *Regular and Chaotic Dynamics.* Springer, New York, 2nd edition, 1992.

[74] F. Benvenuto, G. Casati, and D. L. Shepelyansky. Chaotic autoionization of molecular rydberg states. *Phys. Rev. Lett.*, 72:1818, 1994.

[75] D. L. Shepelyansky and A. D. Stone. Chaotic landau level mixing in classical and quantum wells. *Phys. Rev. Lett.*, 74:2098, 1995.

[76] T. Y. Petrowsky. Chaos and cometary clouds in the solar system. *Phys. Rev. A*, 117:328, 1986.

[77] J. M. Greene. Method for determining a stochastic transition. *J. Math. Phys.*, 20:1183, 1979.

[78] R. S. MacKay. A renormalization approach to invariant circles in area-preserving maps. *Physica D*, 7:283, 1983.

[79] R. S. MacKay and I. C. Percival. Converse KAM - theory and practice. *Comm. Math. Phys.*, 94:469, 1985.

[80] T. M. Fromhold, P. B. Wilkinson, F. W. Sheard, L. Eaves, J. Miao, and G. Edwards. Manifestations of classical chaos in the energy level spectrum of a quantum well. *Phys. Rev. Lett.*, 75:1142, 1995.

[81] T. M. Fromhold, C. R. Trench, S. Bujkiewicz, P. B. Wilkinson, and F. W. Sheard. Quantum chaos for cold atoms in an optical lattice with a tilted harmonic trap. *J. Opt. B*, 2:628, 2000.

[82] R. G. Scott, S. Bujkiewicz, T. M. Fromhold, P. B. Wilkinson, and F. W. Sheard. Effects of chaotic energy-band transport on the quantized states of ultracold sodium atoms in an optical lattice with a tilted harmonic trap. *Phys. Rev. A*, 66:023407, 2002.

[83] T. M. Fromhold, A. Patanè, S. Bujkiewicz, P. B. Wilkinson, D. Fowler, D. Sherwood, S. P. Stapleton, A. A. Krokhin, L. Eaves, M. Henini, N. S. Sankeshwar, and F. W. Sheard. Chaotic electron diffusion through stochastic webs enhances current flow in superlattices. *Nature*, 428:726, 2004.

[84] M. Berry. Quantum chaology, not quantum chaos. *Phys. Scr.*, 40:335, 1989.

[85] P. W. Anderson. Absence of diffusion in certain random lattices. *Phys. Rev.*, 109:1492, 1957.

[86] S. Fishman, D. R. Grempel, and R. E. Prange. Chaos, quantum recurrences, and Anderson localization. *Phys. Rev. Lett.*, 49:509, 1982.

[87] D. R. Grempel, S. Fishman, and R. E. Prange. Localisation in an incommensurate potential: An exactly solvable model. *Phys. Rev. Lett.*, 49:833, 1982.

[88] D. R. Grempel, R. E. Prange, and S. Fishman. Quantum dynamics of a nonintegrable system. *Phys. Rev. A*, 29:1639, 1984.

[89] J. Chabé, G. Lemarié, B. Grémaud, D. Delande, P. Szriftgiser, and J. C. Garreau. Experimental observation of the Anderson metal-insulator transition with atomic matter waves. *Phys. Rev. Lett.*, 101:255702, 2008.

[90] M. Sadgrove. Finding some sense in disorder. *Physics*, 1:41, 2008.

[91] H. Ammann, R. Gray, I. Shvarchuck, and N. Christensen. Quantum delta-kicked rotor: Experimental observation of decoherence. *Phys. Rev. Lett.*, 80:4111, 1998.

[92] H. Ammann and N. Christensen. Quantum delta-kicked rotor: Experimental observation of decoherence. *Phys. Rev. E*, 57:354, 1998.

[93] A. C. Doherty, K. M. D. Vant, G. H. Ball, N. Christensen, and R. Leonhardt. Momentum distributions for the quantum δ-kicked rotor with decoherence. *J. Opt. B*, 2:605, 2000.

[94] K. Vant, G. Ball, H. Ammann, and N. Christensen. Experimental evidence for the role of cantori as barriers in a quantum system. *Phys. Rev. E*, 59:2846, 1999.

[95] K. Vant, G. Ball, and N. Christensen. Momentum distributions for the quantum δ-kicked rotor with decoherence. *Phys. Rev. E*, 61:5994, 2000.

[96] A. Messiah. *Quantum Mechanics.* John Wiley, New York, 1966.

[97] N. Bohr. On the constitution of atoms and molecules. *Phil. Mag.*, 26:1, 1913.

[98] E. Schrödinger. Quantisierung als Eigenwertproblem. *Annalen der Physik*, 386:109, 1926.

[99] H.-P. Breuer and F. Petruccione. *The theory of open quantum systems.* Oxford, New York, 2002.

[100] W. H. F. Talbot. Facts relating to optical science, No. IV. *Phil. Mag.*, 9:401, 1836.

[101] A. W. Lohmann, D. Mendlovic, and G. Shabtay. Talbot (1836), Montgomery (1967), Lau (1948), and Wolf (1955) on periodicity in optics. *Pure Appl. Opt.*, 7:1121, 1998.

[102] K. Patorski. *The Self-Imaging Phenomenon and its Applications.* E. Wolf, Progress in Optics XXVII: Elsevier Science, 1989.

[103] M. Mansuripur. *Classical Optics and its Applications.* Cambridge University Press, Cambridge, 2002.

[104] L. Deng, E. W. Hagley, J. Denschlag, J. E. Simsarian, M. Edwards, C. W. Clark, K. Helmerson, S. L. Rolston, and W. D. Phillips. Temporal matter-wave dispersion Talbot effect. *Phys. Rev. Lett.*, 83:5407, 1999.

[105] B.H. Bransden and C. J. Joachain. *Physics of Atoms and Molecules.* Prentice Hall, London, 2nd edition, 2003.

[106] V. S. Letokhov. *Laser Control of Atoms and Molecules.* Oxford, New York, 2007.

[107] M. B. d'Arcy. *Quantum chaos in atom optics.* PhD thesis, University of Oxford, Balliol College, 2002.

[108] J. C. Robinson. *Atom optics: A new testing ground for quantum chaos.* PhD thesis, The University of Texas, Austin, 1995.

[109] D. A. Steck. *Quantum chaos, transport and decoherence in atom optics.* PhD thesis, The University of Texas, Austin, 2001.

[110] E. L. Raab, M. Prentiss, A. Cable, S. Chu, and D. E. Pritchard. Trapping of neutral sodium atoms with radiation pressure. *Phys. Rev. Lett.*, 59:2631, 1987.

[111] A. Aspect, R. Kaiser, N. Vansteenkiste, and C. I. Westbrook. Laser manipulation of neutral atoms. *Physica Scripta*, T58:69, 1995.

[112] C. S. Adams and E. Riis. Laser cooling and trapping of neutral atoms. *Prog. Quantum Electron.*, 21:1, 1997.

[113] W. D. Phillips. Laser cooling and trapping of neutral atoms. *Rev. Mod. Phys.*, 70:721, 1998.

[114] J. Hecker Denschlag, J. E. Simsarian, H. Häffner, C. McKenzie, A. Browaeys, D. Cho, K. Helmerson, S. L. Rolston, and W. D. Phillips. A Bose-Einstein condensate in an optical lattice. *J. Phys. B*, 35:3095, 2002.

[115] W. C. Wiley and I. H. McLaren. Time-of-flight mass spectrometer with improved resolution. *Rev. Sci. Inst.*, 26:1150, 1955.

[116] R. M. Bowley and M. Sánchez. *Introductory statistical mechanics.* Clarendon, Oxford, 2nd edition, 1999.

[117] L. Pitaevskii and S. Stringari. *Bose-Einstein Condensation.* Clarendon, Oxford, 2003.

[118] M. Gustavsson, E. Haller, M. J. Mark, J. G. Danzl, G. Rojas-Kopeinig, and H.-C. Nägerl. Control of interaction-induced dephasing of bloch oscillations. *arXiv*, 0710:5083, 2007.

[119] T. Kraemer, J. Herbig, M. Mark, T. Weber, C. Chin, H.-C. Nägerl, and R. Grimm. Optimized production of a cesium Bose-Einstein condensate. *Appl. Phys. B*, 79:1013, 2004.

[120] S. Inouye, M. R. Andrews, J. Stenger, H.-J. Miesner, D. M. Stamper-Kurn, and W. Ketterle. Observation of Feshbach resonances in a Bose-Einstein condensate. *Nature*, 392:151, 1998.

[121] J. L. Roberts, N. R. Claussen, J. P. Burke, C. H. Greene, E. A. Cornell, and C. E. Wieman. Resonant magnetic field control of elastic scattering in cold ^{85}Rb. *Phys. Rev. Lett.*, 81:5109, 1998.

[122] T. Köhler, K. Góral, and P. S. Julienne. Production of cold molecules via magnetically tunable Feshbach resonances. *Rev. Mod. Phys.*, 78:1311, 2006.

[123] J. R. Hook and H. E. Hall. *Solid state physics.* John Wiley & Sons, New York, 2nd edition, 1991.

[124] C. Kittel. *Introduction to solid state physics.* John Wiley & Sons, New York, 1996.

[125] S. Fishman, I. Guarneri, and L. Rebuzzini. Stable quantum resonances in atom optics. *Phys. Rev. Lett.*, 89:084101, 2002.

[126] S. Fishman, I. Guarneri, and L. Rebuzzini. A theory for quantum accelerator modes in atom optics. *J. Stat. Phys.*, 110:911, 2003.

[127] C. S. Adams, M. Sigel, and J. Mlynek. Atom optics. *Phys. Rep.*, 240:143, 2002.

[128] J.-A. Currivan, A. Ullah, and M. D. Hoogerland. The initial velocity dependence of the quantum resonance in the delta-kicked rotor. *Europhys. Lett.*, 85:30005, 2009.

[129] J.-A. Currivan. Investigations into quantum resonance and anti-resonance of cold Rb87 atoms interacting with an optical moving standing wave. Technical report, University of Auckland, June 2008.

[130] C. W. Gardiner. *Handbook of Stochastic Methods.* Springer, Berlin, 3rd edition, 2004.

[131] J. Fricke. Transport equations including many-particle correlations for an arbitrary quantum system: A general formalism. *Ann. Phys. (N.Y.)*, 252:479, 1996.

[132] T. Köhler and K. Burnett. Microscopic quantum dynamics approach to the dilute condensed Bose gas. *Phys. Rev. A*, 65:033601, 2002.

[133] M. Abramowitz and I. A. Stegun. *Handbook of Mathematical Functions with Formulas, Graphs, and Mathematical Tables.* U. S. Government Printing Office, Washington, 1964.

[134] M. Kasevich, D. S. Weiss, E. Riis, K. Moler, S. Kasapi, and S. Chu. Atomic velocity selection using stimulated Raman transitions. *Phys. Rev. Lett.*, 66:2297, 1991.

[135] M. Kasevich and S. Chu. Laser cooling below a photon recoil with three-level atoms. *Phys. Rev. Lett.*, 69:1741, 1992.

[136] A. J. Kerman, V. Vuletić, C. Chin, and S. Chu. Beyond optical molasses: 3D Raman sideband cooling of atomic cesium to high phase-space density. *Phys. Rev. Lett.*, 84:439, 2000.

[137] A. Aspect, E. Arimondo, R. Kaiser, N. Vansteenkiste, and C. I. Westbrook. Laser cooling below the one-photon recoil energy by velocity-selective coherent population trapping. *Phys. Rev. Lett.*, 61:826, 1988.

[138] F. Bardou, J. P. Bouchaud, O. Emile, A. Aspect, and C. Cohen-Tannoudji. Subrecoil laser cooling and Lévy flights. *Phys. Rev. Lett.*, 72:203, 1994.

[139] M. Sadgrove, A. Hilliard, T. Mullins, S. Parkins, and R. Leonhardt. Observation of robust quantum resonance peaks in an atom optics kicked rotor with amplitude noise. *Phys. Rev. E*, 70:036217, 2004.

[140] A. E. Leanhardt, T. A. Pasquini, M. Saba, A. Schirotzek, Y. Shin, D. Kielpinski, D. E. Pritchard, and W. Ketterle. Cooling Bose-Einstein condensates below 500 picokelvin. *Science*, 301:1513, 2003.

[141] B. Saubaméa, T. W. Hijmans, S. Kulin, E. Rasel, E. Peik, M. Leduc, and C. Cohen-Tannoudji. Direct measurement of the spatial correlation function of ultracold atoms. *Phys. Rev. Lett.*, 79:3146, 1997.

[142] J. Reichel, F. Bardou, M. Ben Dahan, E. Peik, S. Rand, C. Salomon, and C. Cohen-Tannoudji. Raman cooling of cesium below 3 nK: New approach inspired by Lévy flight statistics. *Phys. Rev. Lett.*, 75:4575, 1995.

[143] R. Johnson and P. Kuby. *Elementary statistics.* Duxbury, Thomson Learning, Pacific Grove, California, 8th edition, 2000.

[144] S. Wu, P. S. Striehl, and M. Prentiss. A Weyl function approach to matter-wave coherence and Talbot-Lau effects. *arXiv*, 0710:5479, 2007.

[145] A. Tonyushkin, S. Wu, and M. Prentiss. Demonstration of perfect coherence preservation for matter waves perturbed by a δ-kicked rotor. *arXiv*, 0803:4153, 2008.

[146] A. Tonyushkin, S. Wu, and M. Prentiss. Perfect coherence preservation in an atom interferometer perturbed by optical standing wave pulses acting as a kicked rotor. In *Quantum Electronics and Laser Science Conference.* Opt. Soc. Am., 2008.

[147] S. Wu, A. Tonyushkin, and M. Prentiss. Observation of coherence revival and fidelity saturation in a δ-kicked rotor potential. *arXiv*, 0801:0475, 2008.

[148] M. R. Drinkwater, R. Haagmans, D. Muzi, A. Popescu, R. Floberghagen, M. Kern, and M. Fehringer. The GOCE gravity mission: ESAs first core earth explorer. In *Proceedings of 3rd International GOCE User Workshop*, Frascati, Italy, 2007. ESA Special Publication SP-627.

[149] K. J. Hughes, J. H. T. Burke, and C. A. Sackett. Suspension of atoms and gravimetry using a pulsed standing wave. *Phys. Rev. Lett.*, 102:150403, 2009.

[150] A. Peters, K. Y. Chung, and S. Chu. High-precision gravity measurements using atom interferometry. *Metrologia*, 38:25, 2001.

[151] A. Peters, K. Y. Chung, and S. Chu. Measurement of gravitational acceleration by dropping atoms. *Nature*, 400:849, 1999.

[152] W. H. Louisell. *Quantum statistical properties of radiation.* John Wiley & Sons, New York, 1973.

[153] S. A. Gardiner. Theory and application of dark states in cavity QED. Master's thesis, University of Waikato, Hamilton, New Zealand, October 1995.

[154] P. Meystre and M. Sargent III. *Elements of quantum optics.* Springer-Verlag, Berlin, 3rd edition, 1991.

[155] A. Montmayrant, A. Arbouet, B. Girard, B. Chatel, A. Barman, B. J. Whitaker, and D. Kaplan. AOPDF-shaped optical parametric amplifier output in the visible. *Appl. Phys. B*, 81:177, 2005.

[156] H. G. Schuster. *Deterministic Chaos: An Introduction.* VCH, Weinheim, 1995.

[157] D. Bigourd, B. Chatel, W. P. Schleich, and B. Girard. Factorisation of numbers with the temporal Talbot effect: Optical implementation by a sequence of shaped ultrashort pulses. *Phys. Rev. Lett.*, 100:030202, 2008.

[158] M. Gilowski, T. Wendrich, T. Müller, C. Jentsch, W. Ertmer, E. M. Rasel, and W. P. Schleich. Gauss sum factorization with cold atoms. *Phys. Rev. Lett.*, 100:030201, 2008.

[159] T. M. Apostol. *Introduction to analytic number theory.* Springer-Verlag, New York, 1976.

[160] V. Armitage and A. Rogers. Gauss sums and quantum mechanics. *J. Phys. A*, 33:5993, 2000.

Manifestation of quantum resonant effects in the atom-optical delta-kicked accelerator

by

Mark Saunders

In this thesis we investigate quantum resonant effects in the atom-optical δ-kicked accelerator.

Using Floquet analysis, we theoretically study the time evolution of quantum systems which have a classical counterpart that exhibits chaotic dynamics. We introduce quantum resonance and quantum antiresonance features of the quantum δ-kicked rotor by setting the pulse period to an integer multiple of the half-Talbot time. The model is generalised to the atom-optical δ-kicked accelerator by considering thermal alkali atoms subject to a periodically pulsed standing wave potential formed from counter-propagating laser beams.

The dynamics of the momentum distribution is analysed by evaluating the momentum moments and momentum cumulants. We derive analytic solutions for these observables for the ultracold and thermal limiting cases, and observe fractional quantum resonant phenomena. Simulations have been developed to examine the time evolution for individual momentum eigenstates, which we use to construct a non-interacting finite temperature gas, based upon a Monte Carlo method. We investigate the temperature dependence of the δ-kicked rotor, neglecting gravitational effects, and show that the atomic dynamics is highly sensitive to the initial momentum width of the gas. A generalisation of the model to quantify the transition between the ultracold and thermal temperature regimes of the atom-optical δ-kicked accelerator is examined using linear regression analysis. High order quantum resonance features are found to be sensitive to the relative acceleration between the atomic gas and the pulsed optical standing wave.

We assess the dependence of the δ-kicked accelerator upon gravitational acceleration, quantifying the width of the high order quantum resonance features, which we use to assess the prospect for precision measurement using a finite temperature gas.